

The Pennsylvania State University
The Graduate School
Department of Material Science and Engineering

**RESIDUAL FERROELECTRICITY, PIEZOELECTRICITY, AND
FLEXOELECTRICITY IN BARIUM STRONTIUM TITANATE TUNABLE
DIELECTRICS**

A Dissertation in
Material Science and Engineering

by

Lauren M. Garten

© 2014 Lauren M. Garten

Submitted in Partial Fulfillment
of the Requirements
for the Degree of

Doctor of Philosophy

December 2014

The dissertation of Lauren M. Garten was reviewed and approved* by the following:

Susan Trolier-McKinstry
Professor of Ceramic Science and Engineering
Dissertation Advisor
Chair of Committee

Clive A. Randall
Professor of Materials Science and Engineering

Michael T. Lanagan
Professor of Engineering Science and Mechanics

Thomas N. Jackson
Robert E. Kirby Chair Professor of Electrical Engineering

Gary L. Messing
Distinguished Professor of Ceramic Science and Engineering
Head of the Department of Materials Science and Engineering

*Signatures are on file in the Graduate School

ABSTRACT

Loss reduction is critical to the development of $\text{Ba}_{1-x}\text{Sr}_x\text{TiO}_3$ (BST) thin film tunable microwave dielectrics. This work addresses mechanisms of loss and performance of $\text{Ba}_{1-x}\text{Sr}_x\text{TiO}_3$, such as residual ferroelectricity, enhanced flexocoupling, and dc electric field induced piezoelectricity.

The presence of residual ferroelectricity –a persistent ferroelectric response above the global phase transition temperature, adds a contribution to dielectric loss from either motion of domain walls or the boundaries of micropolar regions, degrading the tunable performance over a wide frequency range. Rayleigh behavior as a function of temperature was used to track the ferroelectric behavior of BST materials through the ferroelectric to paraelectric transition temperature. The irreversible Rayleigh parameter serve as a metric for the presence of ferroelectricity because this response is dependent on the presence of domain walls, cluster boundaries or phase boundaries. Chemical solution deposited $\text{Ba}_{0.7}\text{Sr}_{0.3}\text{TiO}_3$ films, with relative tunabilities of 86% over 250kV/cm at 100kHz, demonstrated residual ferroelectricity at least 65°C above the ostensible paraelectric transition temperature. The Rayleigh behavior was further corroborated with second harmonic generation, polarization-electric field hysteresis loops and the frequency dependence of the Rayleigh response. The temperature extent of residual ferroelectricity in sputtered and chemical solution deposited films and bulk ceramics was investigated as a function of chemical inhomogeneity on the A-site using electron energy loss spectroscopy. All samples showed some residual ferroelectricity, where the temperature extent was a function of the sample processing. The application of AC electric field for residual ferroelectric measurements of these samples lead to a 100% increase in loss for ac fields exceeding 10kV/cm at room temperature.

The presence of residual ferroelectricity in BST also correlates to the increased flexoelectric response in these materials. Residual ferroelectricity is observed in barium strontium titanate ceramics 30°C above the global phase transition temperature, in the same temperature range in which anomalously large flexoelectric coefficients are reported. The application of a strain gradient in this temperature range was shown to lead to strain gradient-induced poling, or flexoelectric poling, enhancing the flexoelectric response. Flexoelectric poling was observed by the development of a remanent polarization in flexoelectric measurements upon the removal of the applied strain gradient. Additionally, an induced d_{33} piezoelectric response was observed in samples after the removal of the applied strain gradient, indicating that the polarization was realigned during flexoelectric measurements. Flexoelectric poling lead to the production of an internal bias of 9 kV/m. It is concluded that residual ferroelectric response considerably enhances the observed flexoelectric response.

In order to investigate the effects of dc electric field induced piezoelectricity, metrology was designed, developed and calibrated for the measurement of the $e_{31,f}$ piezoelectric coefficient as a function of applied electric field and strain. This allowed for direct measurements of the field-induced piezoelectric response for $\text{Ba}_{0.7}\text{Sr}_{0.3}\text{TiO}_3$ (70:30) and $\text{Ba}_{0.6}\text{Sr}_{0.4}\text{TiO}_3$ (60:40) thin films on MgO and silicon. The relative dielectric tunabilities for the 70:30 and 60:40 composition on MgO were 83% and 70% respectively, with a dielectric loss of 0.011 and 0.004 at 100 kHz respectively. A linear increase in induced piezoelectricity with field to -3.0 C/m^2 and -1.5 C/m^2 at 110 kV/cm was observed in 60:40 BST on MgO and 70:30 BST on Si. Large and hysteretic piezoelectric and tuning responses were observed in the 70:30 BST thin films on MgO. This was consistent with the irreversible Rayleigh behavior, indicating a ferroelectric contribution to the piezoelectric and dielectric response 40°C above the global paraelectric transition temperature. This information

should enable advancements in tunable dielectric components through the removal of piezoelectric resonance-based loss mechanisms.

LIST OF FIGURES	x
LIST OF TABLES.....	xviii
ACKNOWLEDGEMENTS	xix
Chapter 1. Thesis Overview	1
1.1. Introduction... ..	1
1.2. Thesis Objectives.....	2
1.3. Thesis Organization	3
1.4. References	4
Chapter 2. Background Literature	5
2.1. Barium Strontium Titanate	5
2.2. Frequency Agile Systems	12
2.3. Tunable Dielectrics	13
2.4. Dielectric Response	15
2.4.1. Relative Permittivity	15
2.4.2. Dielectric Loss	17
2.5. Piezoelectricity	18
2.5.1. DC Electric Field Induced Piezoelectricity	19
2.6. Ferroelectricity.....	20
2.6.1. Relaxor Ferroelectricity	21
2.6.2. Rayleigh Analysis	24
2.7. Flexoelectricity	25
2.8. References	29
Chapter 3. Experimental Procedures	35
3.1. Preparation of Materials	35
3.1.1. Chemical Solution Deposition of BST Thin Films	35
3.1.2. Pulsed Laser Deposition of BST Thin Films	40

3.1.3. Sputtered Deposition of BST Thin Films	43
3.1.4. Materials from Commercial Sources	44
3.2. Physical Characterization and Methods	44
3.2.1. Scanning Electron Microscopy.....	45
3.2.2. X-Ray Diffraction	45
3.2.3. Transmission Electron Microscopy and Electron Energy Loss Spectroscopy	47
3.3. Electrical Characterization... ..	48
3.3.1. Dielectric Measurements	49
3.3.2. Rayleigh Analysis	49
3.3.3. Current-Voltage Measurements.....	50
3.3.4. Polarization-Electric Field Loops	50
3.4. Other Measurements	51
3.4.1. Second Harmonic Generation	51
3.4.2. Piezoresponse Force Microscopy	51
3.5. References	53
 Chapter 4. $e_{31,f}$ (Electric Field and Strain)	55
4.1. Introduction... ..	55
4.2. Development of an $e_{31,f}$ (Electric Field and Strain) Measurement System	56
4.3. Calibration of an $e_{31,f}$ (Electric Field and Strain) Measurement System	60
4.4. $e_{31,f}$ (Electric Field) in BST... ..	62
4.5. $e_{31,f}$ (Electric Field and Strain) in BST... ..	68
4.6. Conclusions	70
4.7. References	71
 Chapter 5. Residual Ferroelectricity	74
5.1. Introduction... ..	74
5.2. Background.....	74

5.3. Sample Preparation...	78
5.4. Tunability	78
5.5. Dielectric Temperature Dependence	80
5.6. Temperature Dependence of Rayleigh Behavior	83
5.7. Substantiation of Rayleigh Analysis	90
5.8. Conclusions	96
5.9. References	96
Chapter 6. Further Evidence for Residual Ferroelectricity in BST	101
6.1. Introduction	101
6.2. Methods	103
6.3. Results	103
6.3.1. Dielectric Temperature Dependence	103
6.3.2. Rayleigh Analysis	104
6.3.3 Second Harmonic Generation... ..	106
6.3.4. Transmission Electron Microscopy	111
6.4. Conclusions	115
6.5. References	115
Chapter 7. The Flexoelectric Response in BST... ..	117
7.1. Introduction... ..	117
7.2. Methods	119
7.3. Results and Discussion... ..	122
7.4. Conclusions	130
7.5. References	130

Chapter 8. Reliability, Degradation, and Failure Mechanisms in Lead Zirconate Titanate Films.	136
8.1. Introduction...	136
8.2. Methods	139
8.3. Results	141
8.4. Supplemental Methods: Voltage Contrast Microscopy and Optical Microscopy.....	153
8.5. References	155
Chapter 9. Conclusions and Future Work...	159
9.1. Conclusions	159
9.1.1. Residual Ferroelectricity in BST Tunable Dielectrics.....	159
9.1.2. Residual Ferroelectricity and Flexoelectricity	160
9.1.3. Electric Field Induced Piezoelectricity in BST Thin Films.....	161
9.2. Future Work.....	162
9.2.1. Characterization of Residual Ferroelectricity in Materials for Flexoelectric Applications.....	162
9.2.2. Characterization of A-site Chemical Inhomogeneity in BST.....	164
9.3. References	166

LIST OF FIGURES

Figure 2.1. Paraelectric BST unit cell, and point group symmetry.....	5
Figure 2.2. Lattice parameters, spontaneous polarization and permittivity as a function of temperature in barium titanate	6
Figure 2.3. Schematic of the local titanium displacements at temperatures above the displacive phase transition temperature	8
Figure 2.4. Temperature dependence of the birefringence and the full width-half maximum of the longitudinal acoustic mode of a BaTiO ₃ single crystal, inset shows center peak, CP, intensity, above the ferroelectric phase transition.	8
Figure 2.5. The dielectric temperature dependence of strained SrTiO ₃ films on dysprosium scandate, showing frequency dispersion in chemical inhomogeneous materials	10
Figure 2.6. The impact of various dopants to the temperature of the ferroelectric phase transitions in BaTiO ₃ , with the impact of strontium addition highlighted.....	11
Figure 2.7. A comparison of quality factor and tunability for different tunable technologies.....	13
Figure 2.8. The schematic of the dielectric voltage dependence from which the tunability can be calculated.....	14
Figure 2.9. Schematic of the contributions to polarization showing the time domain of each mechanisms	16
Figure 2.10. Dielectric loss tangent as a function of temperature for different compositions of Ba _x Sr _{1-x} TiO ₃	18

Figure 2.11. Induced piezoelectric resonances in the real and imaginary components of impedance, Z , in BST thin films.....	20
Figure 2.12. Polarization-electric field loop for a ferroelectric material and the nucleation and growth of domains in response to the electric field.....	21
Figure 2.13. Comparison of the response of normal and relaxor ferroelectrics.....	23
Figure 2.14. Schematic of the movement of domain walls, indicated by the red dots, across a complex energy landscape under subswitching AC electric fields.....	25
Figure 2.15. Flexoelectric response in barium strontium titanate as a function of temperature above the ferroelectric-paraelectric phase transition temperature, indicated by the line at 21°C.....	27
Figure 2.16. A comparison of the measured and predicted flexocoupling, relating flexoelectric coefficient and the dielectric susceptability, for barium strontium titanate ceramics.....	28
Figure 3.1. Scanning electron micrograph of CSD films on silicon crystallized at 900°C.....	36
Figure 3.2. Differences in lattice parameters for different substrates as a function of coefficient of thermal expansion compared to BST	37
Figure 3.3. Scanning electron micrograph of $\text{Ba}_{0.6}\text{Sr}_{0.4}\text{TiO}_3$ films deposited crystallized for one minute at 900°C on MgO.....	38
Figure 3.4. Scanning electron micrograph of the $\text{Ba}_{0.7}\text{Sr}_{0.3}\text{TiO}_3$ thin films deposited onto platinized MgO substrates, showing a dense film	39

Figure 3.5. First set of pulsed laser deposited $\text{Ba}_{0.7}\text{Sr}_{0.3}\text{TiO}_3$ thin films on platinized alumina substrates deposited at 700°C with an energy density of 1.5 J/cm^2	41
Figure 3.6. Pulsed laser deposition of $\text{Ba}_{0.7}\text{Sr}_{0.3}\text{TiO}_3$ thin films on alumina substrates at 1.25 J/cm^2	42
Figure 3.7. X-ray diffraction pattern for sputtered and CSD $\text{Ba}_{0.7}\text{Sr}_{0.3}\text{TiO}_3$ thin films deposited on $\text{Al}_2\text{O}_3/\text{MgO}$ substrates respectively. Substrate and electrode peaks indicated by * and °	46
Figure 3.8. Schematic of the polishing set up for BST PFM samples.....	52
Figure 4.1. Schematic of the $e_{31,f}$ (electric field, strain) metrology and sample	57
Figure 4.2. Image of $e_{31,f}$ (Electric field and Strain) measurement system in operation.....	58
Figure 4.3. Quarter Wheatstone bridge circuit used for dynamic strain measurements.....	58
Figure 4.4. Schematic of the charge to voltage converter used in the charge portion of the piezoelectric measurements	59
Figure 4.5. A comparison of the transverse piezoelectric response, $e_{31,f}$, as a function of applied DC electric fields for BST films with varied compositions and substrates	64
Figure 4.6. Tunability and DC electric field dependence of the dielectric loss tangent in BST films with varied composition and substrate	65
Figure 4.7. Normalized irreversible Rayleigh behavior for 70:30 BST on MgO and Si, and 60:40 BST on MgO thin films	67
Figure 4.8. Schematic of the DC strain gauge measurement circuit.....	69
Figure 4.9. The impacts of strain on the electric field induced $e_{31,f}$ of BST 70:30 on Si.....	70

- Figure 5.1.** Schematic of the dielectric response as a function of temperature through the paraelectric to ferroelectric phase transition in barium strontium titanate..... 75
- Figure 5.2.** DC electric field dependence of the capacitance (symbols) and dielectric loss tangent (thin lines), for CSD $Ba_xSr_{1-x}TiO_3$ thin films at room temperature and 100kHz 79
- Figure 5.3.** Tunability, DC field dependence of the capacitance (filled symbols) and dielectric loss tangent (open symbols), for a sputtered $Ba_{0.7}Sr_{0.3}TiO_3$ thin film on alumina 80
- Figure 5.4.** Capacitance (filled symbols) and dielectric loss tangent (open symbols) as a function of temperature from 1kHz to 1MHz for a sputtered $Ba_{0.7}Sr_{0.3}TiO_3$ thin film..... 82
- Figure 5.5.** Permittivity (filled symbols) and dielectric loss tangent (open symbols) as a function of temperature from 100Hz to 1MHz for a CSD $Ba_{0.7}Sr_{0.3}TiO_3$ thin film 83
- Figure 5.6.** Characteristic capacitance (above) and dielectric loss tangent (below) small signal AC electric field response for a sputtered $Ba_{0.7}Sr_{0.3}TiO_3$ thin film measured through the temperature range of the global phase transition determined by the dielectric temperature response at a frequency of 1MHz (lines are added to guide the eye) 85
- Figure 5.7.** Rayleigh response for a sputtered BST thin film on alumina substrates as a function of temperature, $Ba_{0.7}Sr_{0.3}TiO_3$ thin film as a function of temperature..... 86
- Figure 5.8.** Characteristic permittivity (above) and dielectric loss (below) as a function of AC electric field response for a CSD $Ba_{0.7}Sr_{0.3}TiO_3$ thin film with a global phase transition temperature of $-22^\circ C$ at 100 kHz 87
- Figure 5.9.** A comparison of the irreversible Rayleigh response as a function of normalized temperature for sputtered and CSD $Ba_xSr_{1-x}TiO_3$ thin films 89

Figure 5.10. Polarization-electric field for the sputtered $\text{Ba}_{0.7}\text{Sr}_{0.3}\text{TiO}_3$ thin film taken on increasing voltage at room temperature and 100Hz	90
Figure 5.11. Polarization electric field loops for the CSD $\text{Ba}_{0.7}\text{Sr}_{0.3}\text{TiO}_3$ thin film taken at room temperature. b.(inset) Magnification showing the remanent polarization and the coercive electric field. P-E loops were extremely slim, indicating the materials were likely macroscopically paraelectric at room temperature	91
Figure 5.12. Minor polarization-electric field loop for a sputtered $\text{Ba}_{0.7}\text{Sr}_{0.3}\text{TiO}_3$ thin film taken at room temperature and 100 Hz	93
Figure 5.13. Frequency dependence of the capacitance as a function of applied small signal AC electric field for a sputtered $\text{Ba}_{0.7}\text{Sr}_{0.3}\text{TiO}_3$ thin film	94
Figure 5.14. Leakage current for the CSD and sputtered BST thin films	95
Figure 6.1. $\text{Ba}_{0.4}\text{Sr}_{0.6}\text{TiO}_3$ ceramics with different pre-calcination mixing times a. 0 hours, b. 3 hours, c. 6 hours, and d. 9 hours ³ . The amount of dielectric dispersion characteristic of relaxor ferroelectric characteristics is larger for shorter mixing times	102
Figure 6.2. The dielectric temperature dependence of $\text{Ba}_{0.8}\text{Sr}_{0.2}\text{TiO}_3$ chemical solution deposited thin films on MgO showing a broad maximum and frequency dispersion	104
Figure 6.3. The irreversible Rayleigh response of various BST materials normalized to temperatures above the ferroelectric phase transition.....	105
Figure 6.4. Normalized SHG response from the 70:30 BST ceramic samples taken at a ramp rate of 3 °C/min and 6 °C/min	107

Figure 6.5. Normalized SHG response above the transition temperature in the 70:30 BST ceramic samples taken at a ramp rate of 3 °C/min measured first on heating then on cooling. The red lines are added as a guide to highlight the change in slope	108
Figure 6.6. Normalized SHG response for the CSD 70:30 BST thin films, with the temperature of the maximum in the dielectric response indicated by the arrow for comparison... ..	110
Figure 6.7. Normalized SHG response for the sputtered 70:30 BST thin films, with the temperature of the maximum in the dielectric response indicated by the arrow for comparison... ..	111
Figure 6.8. Transmission electron microscopy and electron energy loss spectroscopy of 70:30 BST ceramics.....	113
Figure 6.9. Transmission electron microscopy and electron energy loss spectroscopy of sputtered 70:30 BST thin films.....	114
Figure 7.1. Schematic of the flexoelectric testing system and flexoelectric response.....	121
Figure 7.2. Temperature dependence of the Rayleigh response and flexoelectric coefficient (Ma and Cross), normalized to the ferroelectric-paraelectric phase transition temperature.....	123
Figure 7.3. Impact of applied strain gradient on the coercive field of a flexoelectric sample showing flexo-poling and residual imprint upon removal of the electric field.....	126
Figure 7.4. The polarization as a function of applied strain gradient in lead zirconate titanate	127

- Figure 7.5.** Hysteresis in polarization with increasing and decreasing applied strain gradient and the development of a piezoelectric response. The d_{33} measurements were taken after the strain gradient was removed, and hence are remanent piezoelectric coefficients 128
- Figure 8.1.** Image of the PZT films after wire bonding to the top and bottom electrodes 140
- Figure 8.2.** Leakage current as a function of time for a randomly oriented, 1 μm thick, chemical solution deposited $\text{Pb}(\text{Zr}_{0.52}\text{Ti}_{0.48})\text{O}_3$ thin film taken at 150 kV/cm and 180 $^{\circ}\text{C}$ 142
- Figure 8.3.** The time to failure for data sets at three temperatures from a CSD PZT thin film 143
- Figure 8.4.** Median time to failure PZT thin films deposited by different methods, as a function of temperature at a constant voltage. While the chemical solution deposited films were tested at 150 kV/cm, the short lifetimes of the sputtered films required a reduction in the field to 100 kV/cm 145
- Figure 8.5.** Median time to failure as a function of voltage at constant temperature of 150 $^{\circ}\text{C}$ for PZT thin films 146
- Figure 8.6.** Fitting of the leakage current-voltage measurements over a range of temperature for CSD PZT thin films 149
- Figure 8.7.** Refitting the highly accelerated lifetime testing for $\text{Pb}(\text{Zr},\text{Ti})\text{O}_3$ thin films deposited by different methods with different crystallographic orientations. The predicted voltage acceleration factor for the refit data is -2, which is in good agreement with the refit slopes 151
- Figure 8.8.** Voltage contrast microscopy of PZT thin film devices under 30 V for 4.5 hours showing regions of resistance degradation 154

Figure 8.9. Scanning electron micrograph of an area of ejected material after electrical testing in a PZT thin film	155
Figure 9.1. Characteristic EDS response from barium titanate	165

LIST OF TABLES

Table 3.1. Pulsed Laser Deposition of BST Films.....	41
Table 3.2. Sputter Processing Conditions	43
Table 3.3. Lattice parameters and lattice volumes calculated from X-ray diffraction in figure 3.7... ..	47
Table 4.1 Calibration of the $e_{31,f}$ (Electric Field and Strain) Measurement System.....	61
Table 4.2. Transition temperature, tunability, dielectric loss and Rayleigh behavior for BST films at 100kHz.....	62
Table 5.1. Relative tunability and minimum quality factor at maximum tunability calculated for the CSD $Ba_{1-x}Sr_xTiO_3$ thin films at 100kHz	79
Table 8.1. Compilation of previous literature on reliability in PZT thin films	138
Table 8.2. Median time to failure and Weibull fitting parameter for each temperature data set.....	144
Table 8.3. Previous studies on mechanisms associated with a given activation energy in PZT	145
Table 8.4. Activation energy and voltage acceleration factor determined from the Eyring model and the voltage acceleration calculated from the new model	152
Table 8.5. List of conduction mechanisms in dielectrics	148
Table 9.1. Flexoelectric and flexocoupling response in a series of perovskite materials.....	163

ACKNOWLEDGEMENTS

I am truly grateful to have so many good people in my life who have taught me so much. I would first like to thank my advisor Dr. Trolier-McKinstry for taking me on as a student. She has taught me, what I expect to be, some of the most important lessons on life and science. Her intensity and compassion inspire me. I would also like to thank the members of my committee, Drs. Randall, Lanagan, and Jackson for their guidance. Additionally, I would like to thank Dr. Meyer for always being supportive. I would like to acknowledge the MCL staff, particularly Jeff and Tim, who have given so much of their time.

I would also like to thank the many members of the STM, Messing, Randall, Maria, Gopalan, and Meyer groups who have helped me over the years. A special thanks to Raegan, Derek, Nevin, and Susie who have helped me immensely both scientifically and personally. And to those from Missouri for never letting me forget where I come from.

And most importantly, I am grateful for the love and support of my family and Casey Newell. Without your love and support I would not have thought my dreams possible.

Chapter 1.

Thesis Overview

This section provides a brief introduction to the research discussed within this thesis in order to provide a framework for the project objectives. After presenting the project objectives, a short section is provided on the thesis organization.

1.1 Introduction

As telecommunication frequency standards become increasingly complex and devices more compact, it becomes necessary to develop efficient tunable systems.¹ Thin film tunable dielectrics enable cost-effective and scalable frequency agile technologies.^{2, 3} Barium strontium titanate, BST, thin film tunable dielectrics offer high tunability, but suffer from comparatively high dielectric loss in the microwave region.^{2,4,5} Because of this, BST based devices have to-date been limited.⁴ The communication quality factor, a figure of merit for frequency agile systems, highlights the importance of balancing tunability and dielectric loss and is given by:

$$K = \frac{(\eta - 1)^2}{\eta \cdot \tan\delta(0) \cdot \tan\delta(E)}$$

where η is the tunability and $\tan\delta(0)$ and $\tan\delta(E)$ are the unbiased and biased dielectric loss.⁴ Thus, developing efficient BST based tunable systems is dependent on an understanding of and, where possible, mitigation of, the factors impacting dielectric loss.

Losses are incurred in BST thin films through several intrinsic and extrinsic mechanisms. In addition to intrinsic phonon-based loss mechanisms, residual ferroelectricity, electric field induced piezoelectricity and electrical degradation have been observed to contribute to the dielectric loss in BST thin films.^{6,7,8,9} Intrinsic loss and residual ferroelectric contributions to dielectric loss occur in unbiased materials. Mechanisms such as electric field-induced piezoelectricity and electrical degradation are dependent upon the application of an electric field and cannot be completely circumvented. However, with an understanding of the material response, the contributions to loss from induced piezoelectricity can be minimized through design optimization. Similarly, by understanding the mechanisms of breakdown under electrical degradation, predictions of the material reliability can be made. Thus providing an understanding of loss in tunable dielectrics is the first step towards the development of lower loss, higher tunability frequency agile systems. In addition to the benefits to tunable dielectrics, understanding and mitigating loss in barium strontium titanate-based materials impacts a broad range of applications, including dielectric electrostatic energy storage.¹⁰

1.2 Thesis Objectives

The overall goal of this work is to characterize loss mechanisms in barium strontium titanate thin films for tunable dielectric applications. This work focuses on the ferroelectric, piezoelectric and dielectric contributions to dielectric loss experienced during tuning. Rayleigh analysis is employed to investigate the ferroelectric response as a function of temperature near and above the paraelectric phase transition. This methodology provides information on ferroelectric contributions to dielectric loss (and the flexoelectric response) in the paraelectric phase. Electric

field-induced piezoelectricity is also characterized, and a discussion of the development and calibration of the piezoelectric metrology tool is included to provide context. Additional background information is provide on the specific methodologies and metrologies employed within this study, including; $e_{31,f}$ piezoelectric response as a function of electric field and strain, second harmonic generation, transmission electron microscopy and flexoelectric poling.

1.3 Thesis Organization

The second chapter is dedicated to a discussion of the relevant background literature on the essential phenomenology and material properties of barium strontium titanate thin films. Chapter three includes the thin film processing and the physical and electrical thin film characterization. The fourth chapter discusses the design, calibration and development of the $e_{31,f}$ (electric field and strain) piezoelectricity metrology and the DC electric field-induced piezoelectric response in a series of BST thin films. The next section, chapter five, covers measurements of the residual ferroelectricity contributions to dielectric loss through Rayleigh analysis and the corroborating electrical characterization. Chapter five also includes a discussion of the possible underlying mechanisms leading to the development of residual ferroelectricity in BST thin films. Chapter 6 begins a discussion on the impact of residual ferroelectricity on flexoelectric response in BST ceramics. Chapter 7 consists of the work on conduction mechanisms, reliability and breakdown in piezoelectric thin films. And chapter 8 includes possible future work which stems from the observations made during this study.

1.4 References

1. Yang, L., Hou, W., Cao, L., Zhao, B. Y. & Zheng, H. Supporting Demanding Wireless Applications with Frequency-agile Radios. in *Proc. 7th USENIX Conf. Networked Syst. Des. Implement.* 5–5 (USENIX Association, 2010).
2. Tiggelman, M. P. J., Reimann, K., Van Rijs, F., Schmitz, J. & Huetting, R. J. E. On the Trade-Off Between Quality Factor and Tuning Ratio in Tunable High-Frequency Capacitors. *IEEE Trans. Electron Devices* **56**, 2128–2136 (2009).
3. Bao, P., Jackson, T. J., Wang, X. & Lancaster, M. J. Barium strontium titanate thin film varactors for room-temperature microwave device applications. *J. Phys. Appl. Phys.* **41**, 063001 (2008).
4. Tagantsev, A. K., Sherman, V. O., Astafiev, K. F., Venkatesh, J. & Setter, N. Ferroelectric Materials for Microwave Tunable Applications. *J. Electroceramics* **11**, 5–66 (2003).
5. York, R. A. Tunable Dielectrics for RF Circuits, in *Multifunctional Adaptive Microwave Circuits and Systems*, Scitech Pub., 2009, ch. 4.
6. Gurevich, V. L. & Tagantsev, A. K. Intrinsic dielectric loss in crystals. *Adv. Phys.* **40**, 719–767 (1991).
7. Garten, L. M., Lam, P., Harris, D., Maria, J.-P. & Trolier-McKinstry, S. Residual ferroelectricity in barium strontium titanate thin film tunable dielectrics. *J. Appl. Phys.* **116**, 044104 (2014).
8. Noeth, A., Yamada, T., Tagantsev, A. K. & Setter, N. Electrical tuning of dc bias induced acoustic resonances in paraelectric thin films. *J. Appl. Phys.* **104**, 094102 (2008).
9. Zafar, S., Jones, R., Jiang, B., White, B., Kaushik, V., Gillespie, S. The electronic conduction mechanism in barium strontium titanate thin films. *Appl. Phys. Lett.* **73**, 3533–3535 (1998).
10. Roy, D. & Krupanidhi, S. B. Excimer laser ablated barium strontium titanate thin films for dynamic random access memory applications. *Appl. Phys. Lett.* **62**, 1056–1058 (1993).

Chapter 2

Background Literature

2.1 Barium Strontium Titanate

Barium strontium titanate, $\text{Ba}_x\text{Sr}_{1-x}\text{TiO}_3$ or BST, forms as a continuous solid solution between barium titanate and strontium titanate.¹ With respect to the unit cell of the perovskite crystal structure, barium and strontium share the A-site, and the titanium is on the center B-site surrounded by an oxygen octohedra.² Figure 2.1 shows the cubic (paraelectric) BST unit cell, with barium and strontium at the corners shown in green, titanium in the center in red, and oxygen at the face centers of the cube in blue.

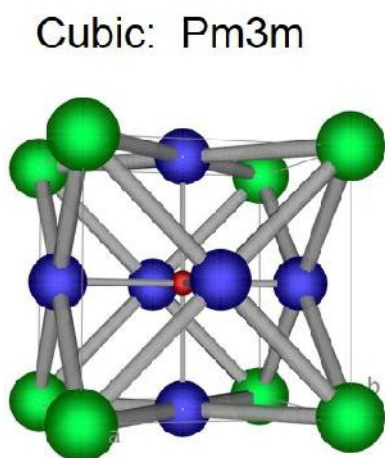


Figure 2.1. Paraelectric BST unit cell, and space group symmetry³

Barium titanate, an end member of the BST solid solution, is a material of interest for many dielectric, piezoelectric, ferroelectric and flexoelectric applications.^{2,4,5} Due to the engineering

importance of barium titanate, the phase formation in this material is well studied. Figure 2.2 shows the lattice parameters, spontaneous polarization and dielectric response through the rhombohedral, orthorhombic, tetragonal, and cubic phases of barium titanate.⁶ The rhombohedral, orthorhombic, and tetragonal phases exhibit piezoelectricity and ferroelectricity. The paraelectric phase, stable above $\sim 130^\circ\text{C}$, is macroscopically cubic, nominally precluding piezoelectricity or ferroelectricity.²

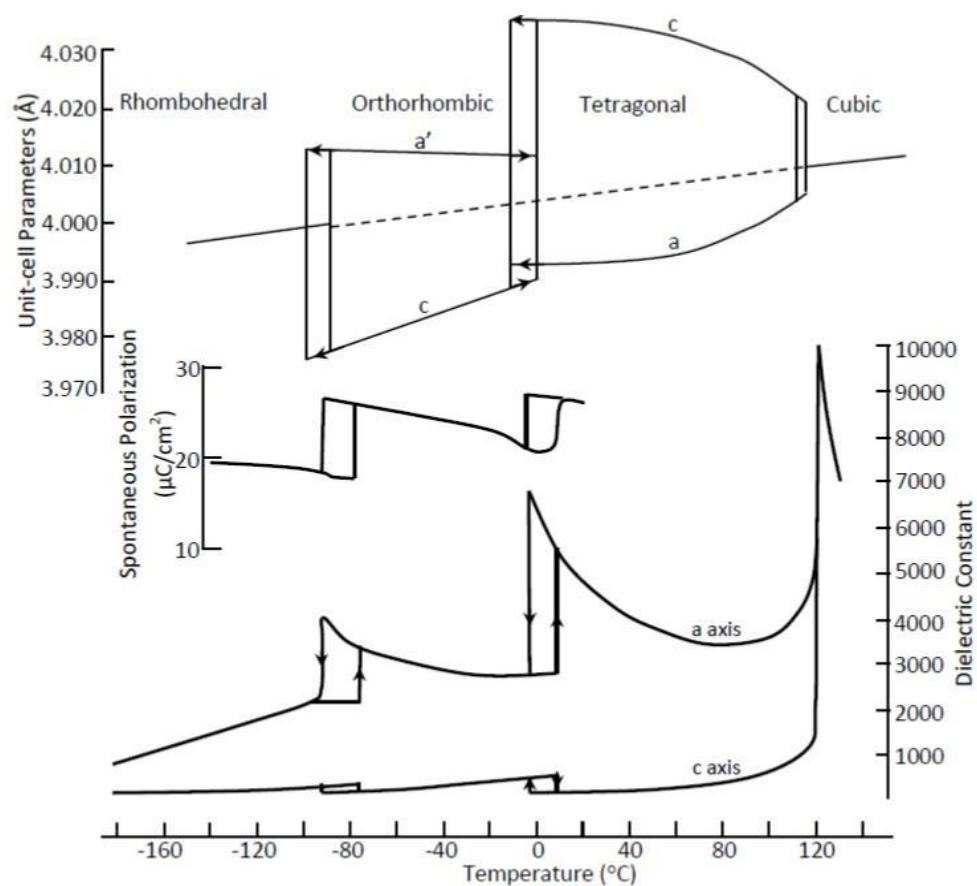


Figure 2.2. Lattice parameters, spontaneous polarization and permittivity as a function of temperature in barium titanate. Figure reproduced from ⁶

In BaTiO₃ and barium strontium titanate, the paraelectric to ferroelectric transition has characteristics of both a displacive and order-disorder type phase transition as first observed by Comes.^{7,8,9} Displacive phase transitions are characterized by the displacement of an atom (or atoms) with respect to neighboring atoms in a unit cell, where the displacements are generally small with respect to the size of the unit cell.¹⁰ In BaTiO₃-based materials, the displacive phase transition is attributed to the condensation of the transverse optic phonon mode, or soft mode, at the Brillouin zone center.¹⁰ This model accounts for the observed phonon spectrum and the Curie constant of the first order, displacive ferroelectric phase transition.² In BaTiO₃, the displacement refers to the offsetting of the titanium from the center of unit cell towards an oxygen on one of the face-centers, with correlated motion of the oxygen sublattice.^{2,11} The resulting unit cell is tetragonal, with one unique lattice parameter and three orthogonal axes. Within the tetragonal unit cell, the centers of positive and negative charge are no longer coincident, breaking the center of symmetry and creating a dipole.

Barium titanate based materials have some characteristics which are consistent with order-disorder type phase transitions.^{7,12,13} The ordering in this instance refers to the coalescence of local titanium displacements along the $\langle 111 \rangle$, as shown in Figure 2.3. These local structural displacements have been observed ~ 100 °C above the displacive phase transition temperature, as shown in the birefringence and Raman data for barium titanate single crystals in Figure 2.4.¹³ X-ray absorption fine structure analysis shows the titanium displacements occurring along [111] direction, but nuclear magnetic resonances, NMR, indicates a more tetragonal-like symmetry, which would be consistent with a time averaged symmetry.⁹ An eight site (rhombohedrally displaced) local structure in paraelectric BST is further supported by neutron diffraction, XAFS, and diffuse scattering distributions.¹⁴ It has also been suggested that the dynamic rhombohedral

distortions persist through all phase transitions in BaTiO_3 and the observed macroscopic symmetry is an effective time averaged non-ergodic symmetry.⁹ The presence of these local distortions is germane to the study of loss in tunable dielectrics, as persistent movable polar displacements would create another mechanisms of loss.

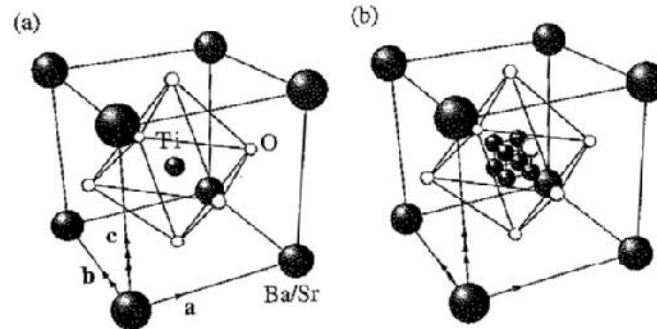


Figure 2.3. Schematic of the local titanium displacements in BaTiO_3 at temperatures above the displacive phase transition temperature. From ¹⁵

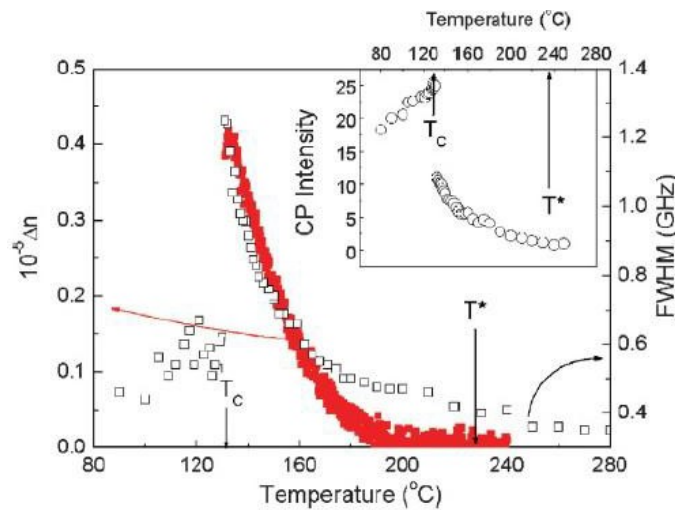


Figure 2.4. Temperature dependence of the birefringence and the full width-half maximum of the longitudinal acoustic mode of a BaTiO_3 single crystal, inset shows center peak, CP, intensity, above the ferroelectric phase transition¹³

Strontium titanate is also of interest for dielectric applications. SrTiO_3 is an incipient ferroelectric, meaning that it does not enter the ferroelectric phase at any temperature. Unlike BaTiO_3 , the soft optic mode in SrTiO_3 does not condense at the Brillouin zone center.^{10,16} Areas of local polar response have been observed in SrTiO_3 ; these have been attributed to local symmetry breaking by defects and grain boundaries.¹⁷ It has been shown, however, that under 1 % tensile strain, strontium titanate can become a relaxor ferroelectric at room temperature.¹⁸ It was further shown that the relaxor nature of the SrTiO_3 films is related to chemical inhomogeneity of strontium, as shown in Figure 2.5 with x indicating the excess or deficiency of strontium. The development of relaxor ferroelectric characteristics in SrTiO_3 is germane to barium strontium titanate, where the order-disorder nature of the phase transition could lead to similar relaxor tendencies in the presence of chemical inhomogeneity.

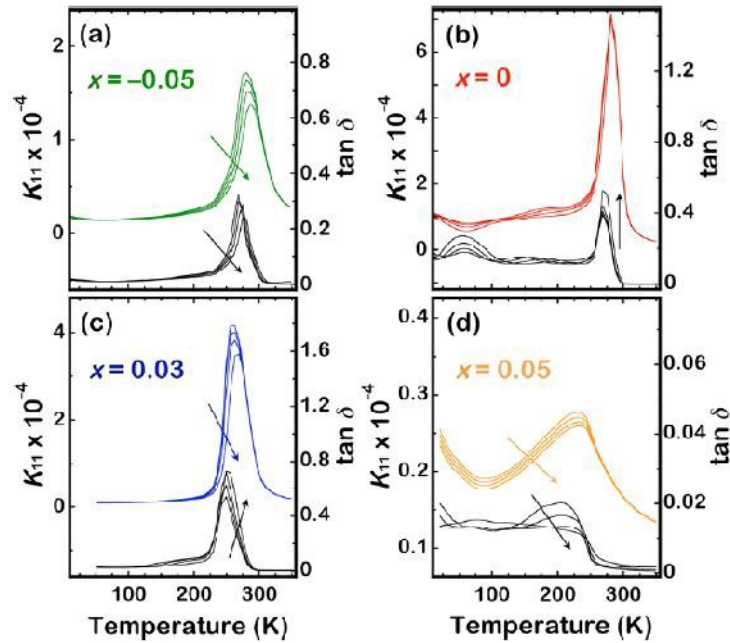


Figure 2.5. The dielectric temperature dependence of strained SrTiO₃ films on dysprosium scandate, showing frequency dispersion in chemically inhomogeneous materials. K_{11} is the relative dielectric constant, x denotes the deviation of the strontium stoichiometry from a 1:1 A:B ratio. From reference ¹⁶

A continuous solid solution forms between BaTiO₃ and SrTiO₃ with the addition of strontium leading to a linear decrease in the ferroelectric phase transition temperature. Figure 2.6 shows the impact of various dopants on the temperature of the cubic-tetragonal transition (the paraelectric to ferroelectric transition temperature, T_c), the tetragonal-orthorhombic transition, and then orthorhombic-rhombohedral transition in BaTiO₃.¹¹ The impact of the strontium on the cubic transition is highlighted. For applications such as tunable dielectrics, the ratio of barium to

strontium is set near or below 70:30, in order to suppress the ferroelectric phase below operating temperatures.

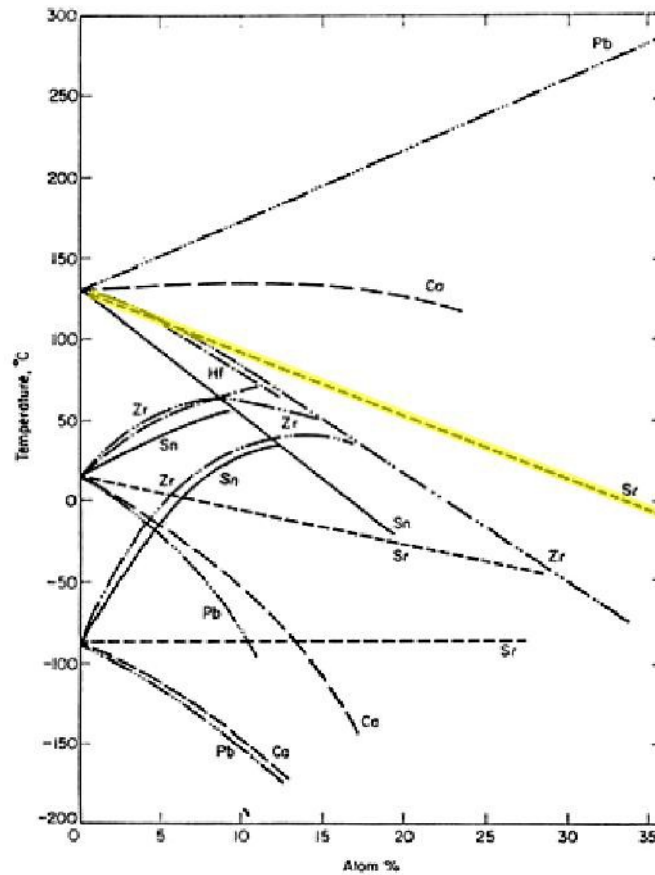


Figure 2.6. The impact of various dopants to the temperature of the ferroelectric phase transitions in BaTiO₃, with the impact of strontium addition highlighted. From reference ¹¹

2.2. Frequency Agile Systems

Barium strontium titanate thin films are of interest for tunable dielectrics in frequency agile applications. This section covers the motivation behind the development of frequency agile electronics with a particular focus on tunable dielectrics.

Frequency agile electronics allow for the optimization of the telecommunication frequency space, while minimizing the electronics footprint. Due to the limitations of wideband circuitry and analogue-to-digital converters, the development of tunable radio frequency front ends is critical for multi-frequency telecommunications.¹⁹ Frequency agile technologies are currently being developed for military and commercial telecommunications applications.^{19,20} Frequency switching is often used in tactical military communications to prevent tracking or jamming of battlefield communications.²¹

Practical implementation of any frequency agile technology requires a combination of high tunability and low loss. The communication quality factor, K , is a figure of merit for frequency agile systems which highlights the importance of balancing tunability and loss.²² The communication quality factor is calculated as follows:

$$K = \frac{(\eta - 1)^2}{\eta \times \tan\delta(0) \times \tan\delta(E)}$$

where η is the tunability, and $\tan\delta(0)$ and $\tan\delta(E)$ are the dielectric loss at zero field and at the electric field, E , used for tuning.

Figure 2.7 shows the balance between tunability and loss for a series of different frequency agile technologies. Q stands for the quality factor, determined from: $Q = \frac{1}{\tan\delta}$. Further increases

in quality factor, and thus decreases in loss, would facilitate the competitiveness of tunable dielectrics as a viable frequency agile technology.

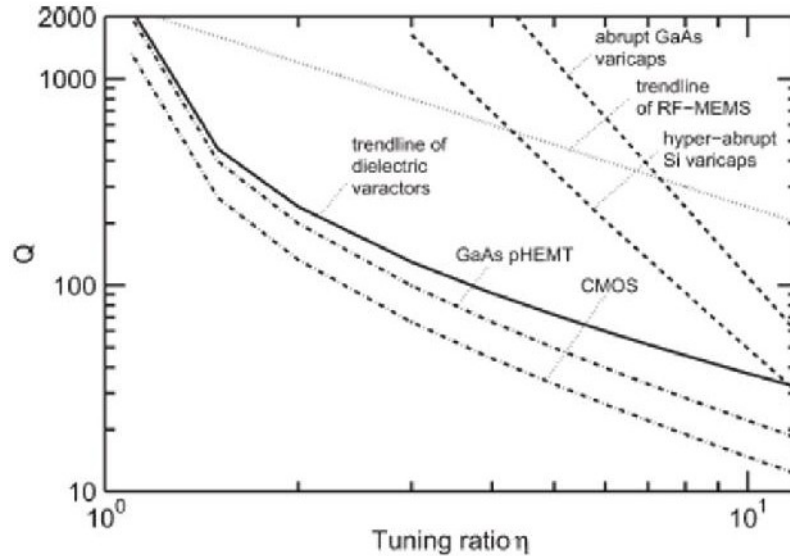


Figure 2.7. A comparison of quality factor and tunability for different tunable technologies ²³

2.2.1. Tunable Dielectrics

In tunable dielectrics, the DC electric field dependence of the permittivity is used to provide frequency agility. The tunability of a system is calculated from the difference in the permittivity maximum (typically the unbiased permittivity in paraelectrics) and the permittivity at a set DC electric field, shown in Figure 2.8.²⁰ The equation for relative tunability is as follows:

$$\eta = \frac{\epsilon_r(0) - \epsilon_r(V)}{\epsilon_r(0)}$$

where $\epsilon_r(0)$ and $\epsilon_r(E)$ are the maximum permittivity and the permittivity at a particular voltage, respectively.²⁰

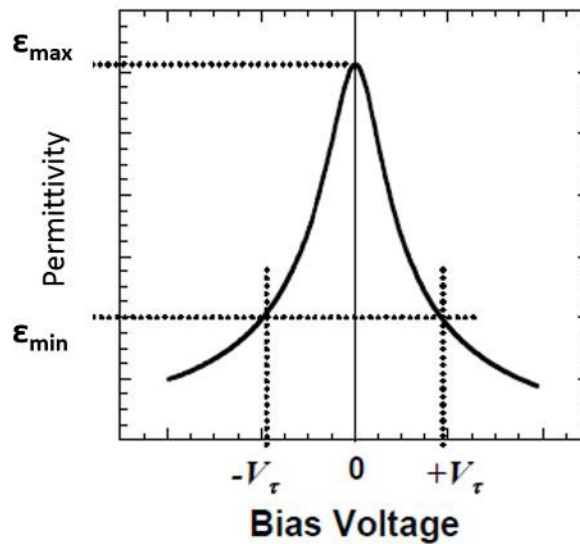


Figure 2.8. The schematic of the dielectric voltage dependence from which the tunability can be calculated²⁰

Tunable dielectrics are based on solid state devices and as such, offer reliable, fast acting tunability.^{19,20} Compared to tunable dielectrics, mechanically tunable filters tend to be slower and larger, while varactor diodes are faster but have poor power handling and high losses in the RF.²³ Tunable dielectrics are employed in voltage-controlled oscillators, tunable filters and phase shifters.^{12,19,20,21} Barium strontium titanate is a primary candidate for tunable dielectrics. It offers high tunability, fast tuning and high electric fields to breakdown,²⁰ but still suffers from comparatively high loss in the microwave region.²² In order to develop BST thin films as a competitive tunable technology, the factors impacting loss need to be assessed and mitigated where possible.

2.3. Dielectric Response

As the focus of this work is towards the development of barium strontium titanate in dielectric applications, the next section will provide a brief discussion of the relevant terms relating to the dielectric response.

2.3.1. Relative Permittivity

The relative permittivity is a measure of the polarizability of a material compared to the polarizability of free space. The equations for relative permittivity and the complex form of relative permittivity in a capacitor are as follows:

$$D = \epsilon_0 E + P = \epsilon_r \epsilon_0 E$$

$$\epsilon_r^* = \epsilon_r' - i\epsilon_r''$$

vector, applied electric

where D is the electric displacement, E is the applied electric field, P is the polarization, ϵ_0 is the permittivity of free space, and ϵ_r' is the real and ϵ_r'' is the imaginary components of relative permittivity.^{24,25} Contributions to relative permittivity arise from electronic (distortions of the electron cloud), atomic (distortions in bond length between ions of different charge), dipole orientation (the alignment of a permanent dipoles), hopping (movement of charges between crystallographic sites) and space charge (macroscopic movement of charges until blocked by an insulating interface) mechanisms.²⁶ There is a frequency limit to the contribution from each source, where loss of any contribution is associated with a relaxation or resonance. Figure 2.9 shows the polarization which develops due to each mechanism as a function of the average response time.²⁶

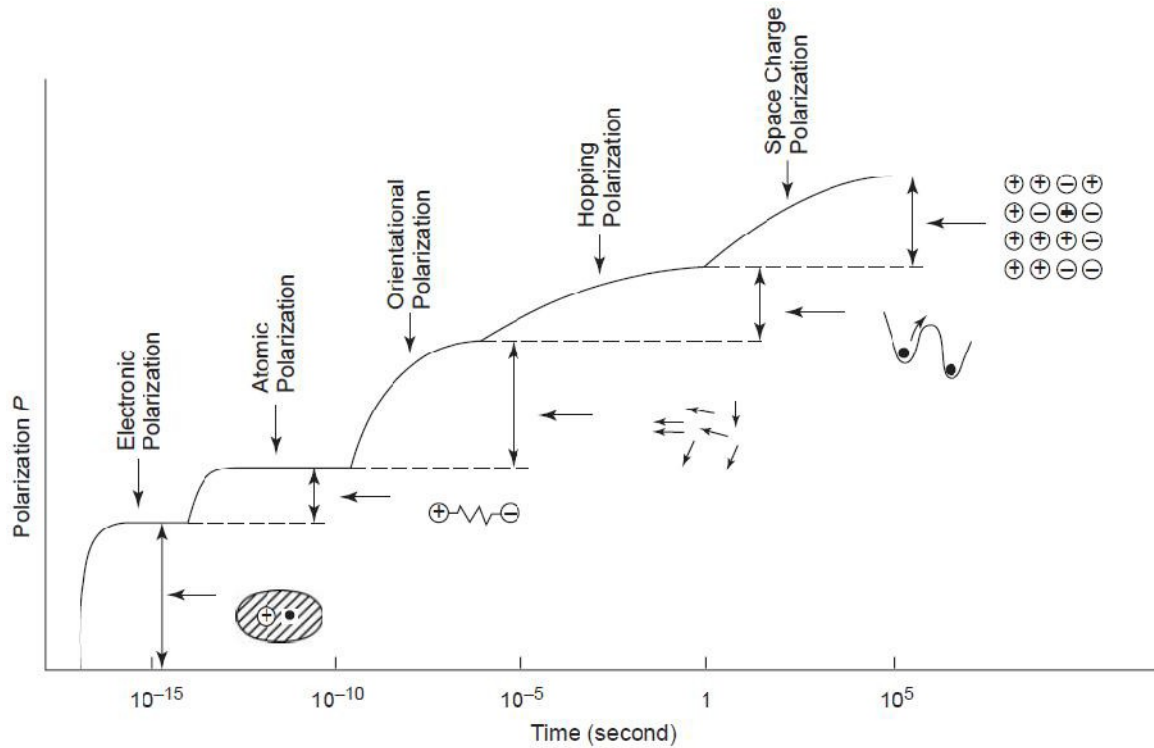


Figure 2.9. Schematic of the contributions to polarization showing the time domain of each mechanism. From reference ²⁶

In this work, the temperature dependence of the permittivity was also considered, as the temperature of the maximum in permittivity (T_{\max}) is associated with the ferroelectric to paraelectric phase change. Examples of the large increase in permittivity at the phase transition are shown in Figures 2.2 and 2.5. Generally, above the ferroelectric to paraelectric phase transition temperature the permittivity follows the Curie-Weiss law, described by:

$$\varepsilon = \varepsilon_0 + \frac{C}{T - T_0}$$

where C is the Curie constant, and T_0 is the Curie-Weiss temperature. In materials with first order phase transitions, such as barium strontium titanate, the Curie-Weiss temperature and the transition temperature T_c need not coincide.

2.3.2 Dielectric Loss

The figure of merit often used to gauge dielectric loss, which is measured as the ratio of the imaginary to real permittivity, or the loss current to charging current, is the loss tangent, $\tan\delta$.²⁴ High losses in the microwave regime make ferroelectric materials with domain wall contributions to the loss, less interesting for microwave devices.²⁷ Jin et al. have reported an extrinsic (ferroelectric) contribution to the dielectric response and loss in perovskite ferroelectric ceramics extending into the low gigahertz frequency range, producing both a strong dispersion and an increase in dielectric loss in the frequency range of interest for tunable devices.²⁸

The measured dielectric loss of a capacitor is a combination of intrinsic and extrinsic loss mechanisms. Intrinsic loss in centrosymmetric materials comes from the three quantum and four quantum loss mechanisms and in non-centrosymmetric materials, or materials under asymmetric external stimuli, quasi-Debye loss mechanisms are also possible.²⁹ Further external losses can come from charged defects, hysteretic domain wall, cluster or phase boundary movements, piezoelectric resonances, resistance degradation, and grain boundaries.³⁰ It is these external loss mechanisms that are the focus of this work.

In ferroelectric barium strontium titanate, domain wall, cluster, or phase boundary motion adds contributions to the dielectric loss. Figure 2.10 shows the two order of magnitude increase in loss which occurs upon entering the ferroelectric phase from the paraelectric prototype. The

temperature of this onset is a function of the composition x in $\text{Ba}_x\text{Sr}_{1-x}\text{TiO}_3$. In the ferroelectric phase, the material is also piezoelectric, leading to additional loss mechanisms discussed in the next section. In this work, the impact of residual ferroelectricity –a persistent ferroelectric response above the global ferroelectric temperature, and DC electric field induced piezoelectric loss mechanisms are characterized.

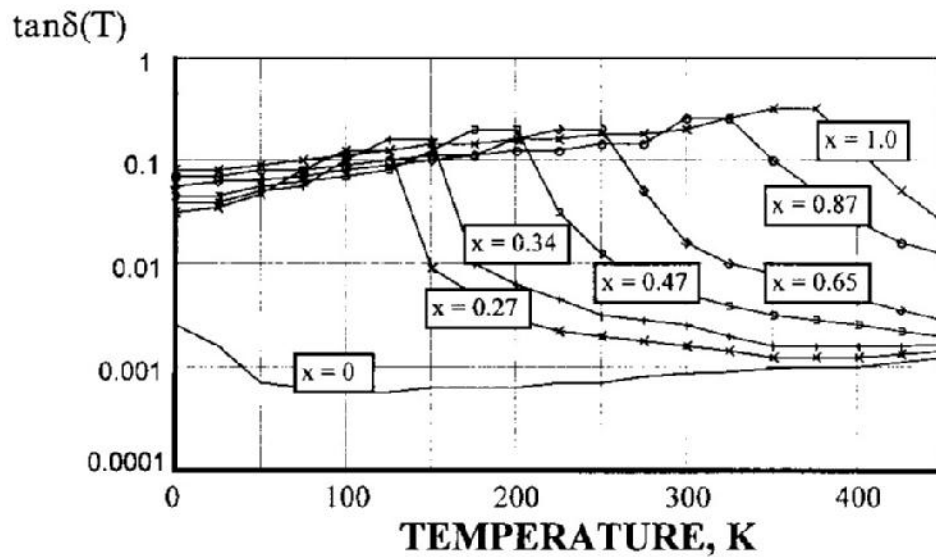


Figure 2.10. Dielectric loss tangent as a function of temperature for different compositions of $\text{Ba}_x\text{Sr}_{1-x}\text{TiO}_3$. From reference ³¹

2.4. Piezoelectricity

The direct piezoelectric effect is the linear coupling between mechanical stress and electric polarization.¹¹ The coefficients of the direct response are equivalent to those of the converse

piezoelectric response, which relates the applied electric field to mechanical strain.³² The equations for the direct and converse piezoelectric effect are as follows:

$$D_i = e_{ij}x_j$$

$$\sigma_i = -e_{ki}E_k$$

where D is the dielectric displacement, E is the applied electric field, x is the strain and e is the piezoelectric coefficient.²⁵ Piezoelectricity is a third order tensor properties and thus exclusive to materials lacking a center of symmetry or other combinations of symmetry elements that forbid the effect (e.g. as for point group 432 and the Curie group symmetry in unpoled ferroelectrics). Often for thin film applications, the piezoelectric response of interest is the $e_{31,f}$ coefficient, which relates the in-plane strain to the out of plane dielectric displacement.³³

2.4.1. DC Electric Field Induced Piezoelectricity

In tunable dielectrics, induced piezoelectricity is one mechanism leading to increased loss. Intrinsic piezoelectricity is exclusive to materials for which the third rank tensor property is not symmetry-forbidden. However, the application of an electric field to a centrosymmetric material can induce piezoelectricity through a distortion of structure along the direction of the electric field.³⁴ In tunable dielectrics, induced piezoelectricity is a consequence of the DC electric fields used for tuning. Induced piezoelectricity leads to resonances in impedance, shown in Figure 2.9, which interfere with impedance matching.^{35,36}

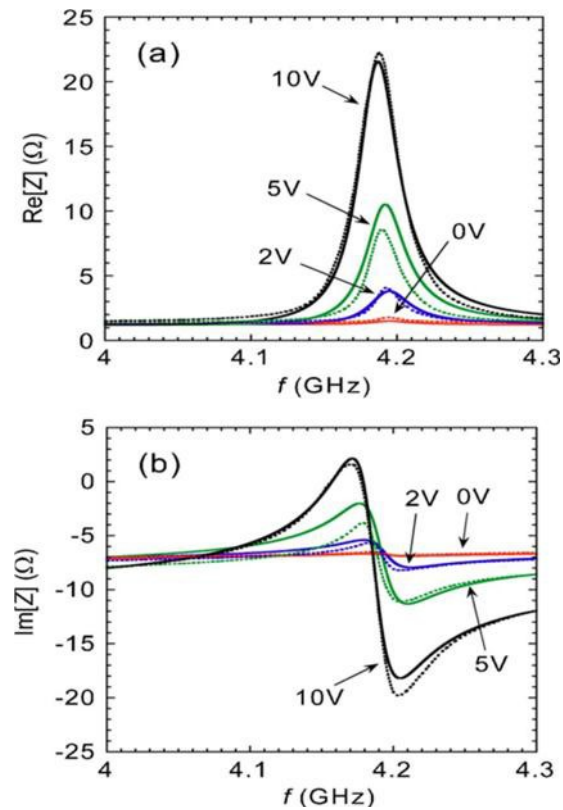


Figure 2.11. Induced piezoelectric resonances in the real and imaginary components of impedance, Z , in BST thin films.³⁶

2.5. Ferroelectricity

Ferroelectrics, which are a subset of piezoelectric materials, are materials which develop a spontaneous electrical polarization that can be reoriented between crystallographically defined states with an applied electric field.² Ferroelectrics display hysteresis with applied electric fields, associated with nucleation and growth of domains in response to the field, as shown in Figure 2.12.³⁷

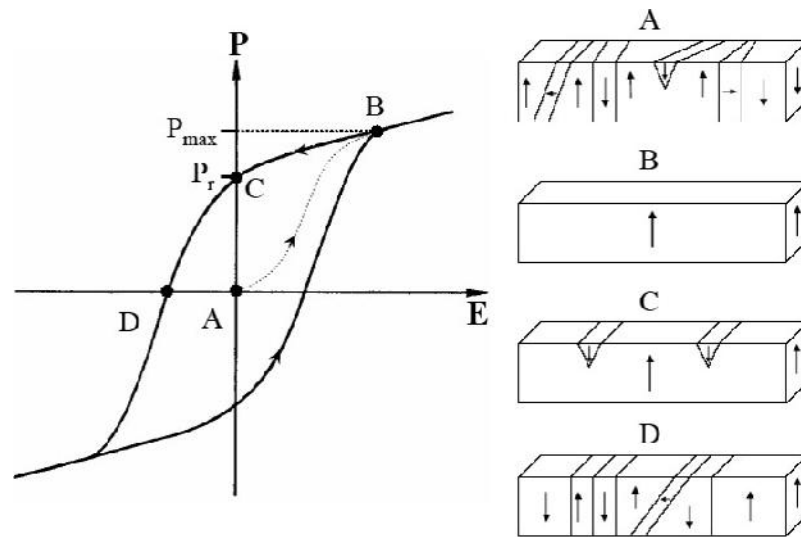


Figure 2.12. Polarization-electric field loop for a ferroelectric material and the nucleation and growth of domains in response to the electric field. From reference ³⁷

Domains are areas of like oriented spontaneous polarization. Domains form in response to the local electrostatic and elastic boundary conditions, within the bounds of the crystallographic symmetry of the ferroelectric phase. In tetragonal barium strontium titanate, domains meet at angles of $\sim 90^\circ$ or 180° in accordance with the allowable directions of titanium displacement. The presence, formation, movement and alignment of these domains is critical to the understanding of this work and will be discussed further in chapter 5.

2.5.1. Relaxor Ferroelectricity

There is another class of polar materials relevant to this study called relaxor ferroelectrics. Relaxor ferroelectrics are characterized by nanometer scale regions of polarization, and chemical

inhomogeneity at similar length scales.^{38,39} Chemical ordering has been shown in some materials, such as $\text{Pb}(\text{Sc}_{0.5}\text{Ta}_{0.5})\text{O}_3$, to lead to a transition from relaxor to normal ferroelectric behavior.^{40,41}

Relaxor ferroelectrics do not go exhibit the sharp phase transition observed in normal ferroelectrics. Rather nano-scale polar regions persist up to the Burns temperature, which can be over 100°C above T_{max} . Macroscopic manifestations of relaxor behavior include a characteristic frequency dispersion and diffuse maximum observed in the dielectric temperature response. Additionally, the polarization-electric field hysteresis loops in relaxor ferroelectrics are characteristically very thin. Figure 2.13 shows a comparison of dielectric and ferroelectric properties of normal and relaxor ferroelectrics.⁴² Figure 2.13 shows a gradual decay in the polarization which is very different than the response expected for a first-order or second-order phase transition. This gradual decay in the polarization is attributed to the persistence of the nano-scale polar regions to higher temperatures. Figure 2.5 also provides an example of relaxor ferroelectric behavior in a non-stoichiometric strontium titanate thin film, an end member of barium strontium titanate.

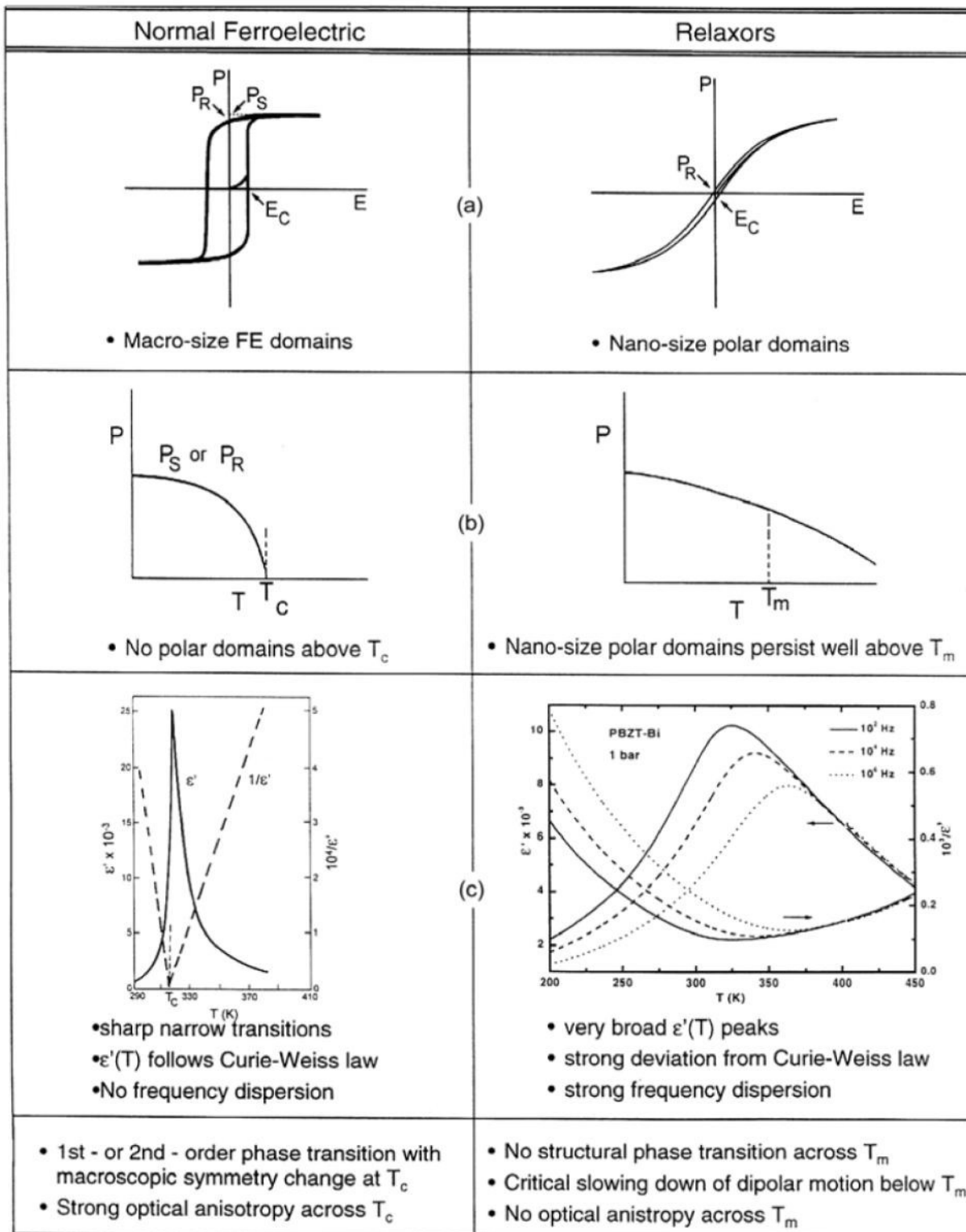


Figure 2.13. Comparison of the response of normal and relaxor ferroelectrics ⁴²

2.5.2. Rayleigh analysis

Rayleigh analysis, first developed to describe the non-linear response of the magnetization to the applied magnetic field,⁴³ has been adapted to describe the field dependence of the dielectric and piezoelectric response in ferroelectric materials.^{44,45} The amplitude dependence of the dielectric response is coupled to a hysteresis attributed to the interaction of domain walls, phase boundaries or domain wall clusters with pinning centers in the material.⁴⁶ The Rayleigh relationship for dielectric non-linearity is given by:

$$\varepsilon_{33} = \varepsilon_{init} + \alpha E_{AC}$$

where ε_{init} is the reversible and α is the irreversible Rayleigh coefficient, and E_{AC} is the oscillating electric field.⁴⁴ Rayleigh analysis is conducted within the subswitching regime, typically $E_{AC} <$ half the coercive electric field, in order to avoid changes in the domain structure.⁴⁷ Reversible contributions to the dielectric response arise from the intrinsic lattice response and non-lossy domain wall motion; irreversible contributions come from the pinning and depinning of domains as they move between potential energy wells.⁴⁶ Figure 2.14 presents a schematic of the reversible and irreversible domain wall or boundary movements across an area with pinning centers of different strengths.

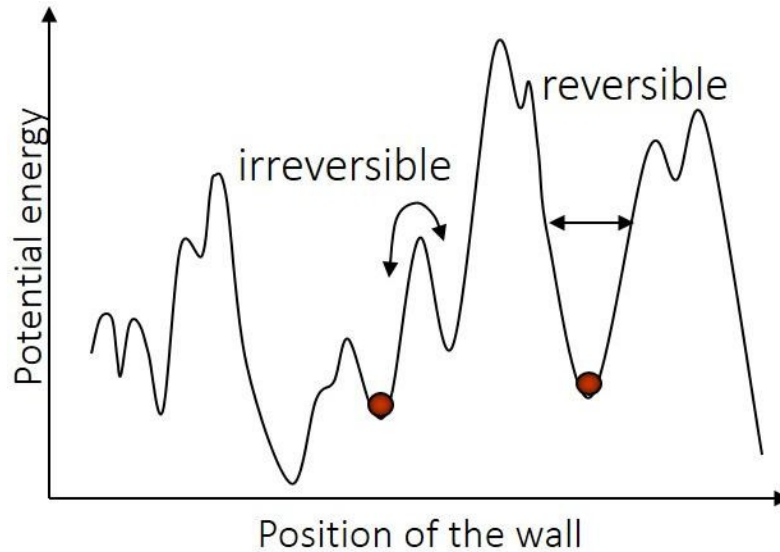


Figure 2.14. Schematic of the movement of domain walls, indicated by the red dots, across a complex energy landscape under subswitching AC electric fields⁴⁸

2.6. Flexoelectricity

Flexoelectricity describes the development of polarization due to the application of a strain gradient.⁵ The equations for flexoelectricity are:

$$P = \chi E + \mu \frac{\partial u}{\partial x}$$

where P is the polarization, χ is the dielectric susceptibility, E is the electric field, μ is the flexoelectric coefficient, and $\partial u / \partial x$ is the strain gradient.⁴⁹ Flexoelectricity is an even rank tensor property, and as such can occur in a material of any symmetry. For a material with macroscopic cubic symmetry, such as paraelectric or unpoled ferroelectric barium strontium titanate, the

allowable property matrix includes the μ_{1111} , μ_{1122} , and the μ_{1212} coefficients (μ_{11} , μ_{12} , and μ_{44} in matrix notation).⁵⁰

Flexoelectricity was first predicted by Mashkevich and Tolpygo, with the phenomenology developed by Kogan and adapted by Indembon, Longinov and Osipov.⁵¹ Early estimates of the flexoelectric coefficients in simple solids predicted a response of approximately 10^{-10} - 10^{-11} C/m.^{50,51} Four decades later, Ma and Cross discovered flexoelectric coefficients in lead magnesium niobate over $5 \mu\text{C}/\text{m}$.⁵⁰ These flexoelectric measurements were made on clamped cantilever samples with 1 Hz excitation strain, with strain measured via differential variable reluctance transducers which were phase locked to the charge output from the sample.⁵² The alignment of nano-polar regions, associated with relaxor ferroelectricity, due to strain-gradient poling was proposed as the justification for the enhancements in flexoelectric response.⁵⁰ However investigations of materials with a similar structure but (theoretically) lacking nanopolar regions, such as barium strontium titanate, showed an increase in the μ_{12} flexoelectric coefficient to over $100 \mu\text{C}/\text{m}$ within 2°C of the transition temperature.⁵² The temperature dependent flexoelectric results for BST are shown in Figure 2.15.⁵²

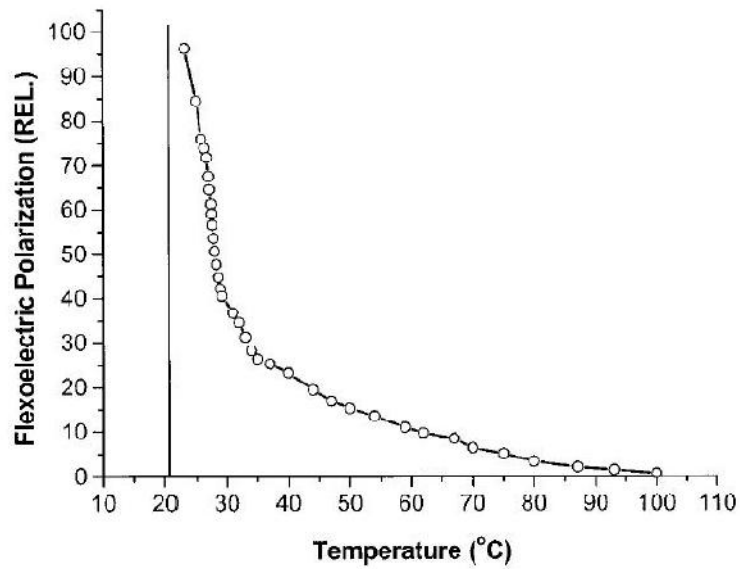


Figure 2.15. Flexoelectric response in barium strontium titanate as a function of temperature above the ferroelectric-paraelectric phase transition temperature, indicated by the line at 21°C.⁵¹

The increase in flexoelectric response six orders of magnitude above theoretical predictions was unexpected, and required revisiting the flexoelectric phenomenology for high permittivity dielectrics. Tagantsev proposed a relationship between the polarizability of the material and the polarization which develops due to an applied strain gradient.^{52,53} The relationships between dielectric susceptibility, χ , and flexoelectric coefficient, μ , are as follows:

$$\mu = f\chi$$

$$f \approx \frac{q}{4\pi\epsilon_0 a} \cong 1 - 10 \text{ V}$$

where f is the flexocoupling coefficient, q is the charge on an electron, and a is the lattice parameter. Flexocoupling is expected to be within 1-10 volts for most materials. Flexocoupling

coefficients for perovskite materials predict the destabilization of the perovskite structure into an incommensurate phase for flexocoupling factors greater than 10 volts.^{49,54} However, there have been reports of flexocoupling coefficients in barium strontium titanate over 850 V.⁴⁹ Figure 2.16 shows the discrepancy between the measured flexoelectric response, shown as dots, and theoretically predicted response, dashes, in BST.⁵² This work provides insight into the enhancements in flexocoupling coefficient in BST.

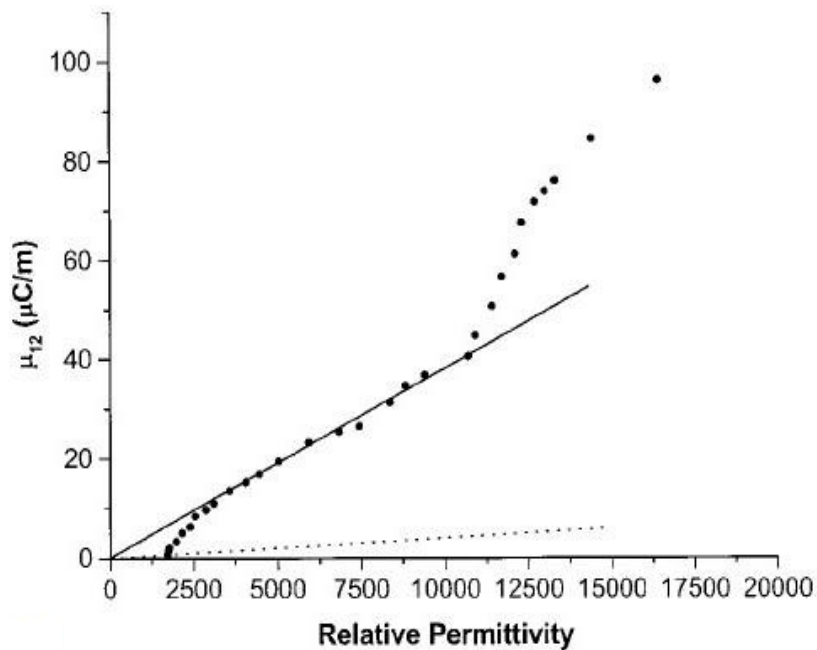


Figure 2.16. A comparison of the measured and predicted flexocoupling, relating flexoelectric coefficient and the dielectric susceptibility, for barium strontium titanate ceramics⁵²

2.7. References

1. Pervez, N. K., Hansen, P. J. & York, R. A. High tunability barium strontium titanate thin films for rf circuit applications. *Appl. Phys. Lett.* **85**, 4451–4453 (2004).
2. F. Jona & G. Shirane. *Ferroelectric Crystals*. (Dover, 1993).
3. Trolier-McKinstry, S. in *Piezoelectric Acoust. Mater. Transducer Appl.* (eds. Safari, A. & Akdoğan, E. K.) 39–56 (Springer US, 2008).
4. Moulson, A. J. ,Herbert, J. M. *Electroceramics: Materials, Properties, Applications*. England. (John Wiley & Sons, 2003).
5. Cross, L. E. Flexoelectric effects: Charge separation in insulating solids subjected to elastic strain gradients. *J. Mater. Sci.* **41**, 53–63 (2006).
6. Aksel, E. & Jones, J. L. Advances in lead-free piezoelectric materials for sensors and actuators. *Sensors* **10**, 1935–1954 (2010).
7. Zalar, B., Laguta, V. V. & Blinc, R. NMR Evidence for the coexistence of order-disorder and displacive components in barium titanate. *Phys. Rev. Lett.* **90**, 037601 (2003).
8. Comes, Robert. Etude des désordres de structure dans le titanate de barium et le niobate de potassium. Diss. Université de Paris, 1969.
9. Stern, E. A. Character of order-disorder and displacive components in barium titanate. *Phys. Rev. Lett.* **93**, 037601 (2004).
10. Cochran, W. *The dynamics of atoms in crystals*. (Edward Arnold Publishers Limited, 1973).
11. Jaffe, B., Cook, W. R. & Jaffe, H. L. *Piezoelectric ceramics*. (Academic Press, 1971).
12. Bussmann-Holder, A., Beige, H. & Völkel, G. Precursor effects, broken local symmetry, and coexistence of order-disorder and displacive dynamics in perovskite ferroelectrics. *Phys. Rev. B* **79**, 184111 (2009).

13. Ko, J.-H., Kim, T. H., Roleder, K., Rytz, D. & Kojima, S. Precursor dynamics in the ferroelectric phase transition of barium titanate single crystals studied by Brillouin light scattering. *Phys. Rev. B* **84**, 094123 (2011).
14. Levin, I., Krayzman, V. & Woicik, J. C. Local structure in perovskite (Ba,Sr)TiO₃: Reverse Monte Carlo refinements from multiple measurement techniques. *Phys. Rev. B* **89**, 024106 (2014).
15. Blinc, R. *Advanced Ferroelectricity*. **151**, (Oxford Science Publications, 2011).
16. Lee, C.-H., Skoromets, V., Biegalski, M. D., Lei, S., Haislmaier, R., Bernhagen, M., Uecker, R., Xi, X., Gopalan, V., Marti, X., Kamba, S., Kuzel, P., Schlom, D. G., Effect of stoichiometry on the dielectric properties and soft mode behavior of strained epitaxial SrTiO₃ thin films on DyScO₃ substrates. *Appl. Phys. Lett.* **102**, 082905 (2013).
17. Pertsev, N. A., Tagantsev, A. K. & Setter, N. Phase transitions and strain-induced ferroelectricity in SrTiO₃ epitaxial thin films. *Phys. Rev. B* **61**, R825–R829 (2000).
18. Biegalski, M. D. Jia, Y., Schlom, D. G., Trolier-McKinstry, S., Streiffer, S. K., Sherman, V., Uecker, R., Reiche, P. Relaxor ferroelectricity in strained epitaxial SrTiO₃ thin films on DyScO₃ substrates. *Appl. Phys. Lett.* **88**, 192907 (2006).
19. Haridasan, V., Lam, P.G.,Feng, Z.,Fathelbab, W.M.,Maria, J.-P.,Kingon, A.I.,Steer, M.B. Tunable ferroelectric microwave bandpass filters optimised for system-level integration. *IET Microw. Antennas Propag.* **5**, 1234–1241 (2011).
20. York, R. A. Tunable Dielectrics for RF Circuits, in Multifunctional Adaptive Microwave Circuits and Systems, Scitech Pub., 2009, ch. 4.

21. Teo, P. T., Vinoy, K. J., Jose, K. A., Varadan, V. K., Varadan, V. V., Gan, Y. B., Design and Development of Tunable Multi-Layer Smart Antennas Using Ferroelectric Materials. *J. Intell. Mater. Syst. Struct.* **11**, 294–299 (2000).
22. Tagantsev, A. K., Sherman, V. O., Astafiev, K. F., Venkatesh, J. & Setter, N. Ferroelectric materials for microwave tunable applications. *J. Electroceramics* **11**, 5–66 (2003).
23. Tiggelman, M. P. J., Reimann, K., Van Rijs, F., Schmitz, J. & Hueting, R. J. E. On the trade-off between quality factor and tuning ratio in tunable high-frequency capacitors. *IEEE Trans. Electron Devices* **56**, 2128–2136 (2009).
24. Hippel, A. R. V. *Dielectrics and Waves*. (Artech House Print on Demand, 1995).
25. Moulson, A. J. & Herbert, J. M. *Electroceramics: Materials, Properties, Applications*. (John Wiley & Sons, 2003).
26. Kao, K.-C. *Dielectric Phenomena in Solids: With Emphasis on Physical Concepts of Electronic Processes*. (Academic Press, 2004).
27. Astafiev, K. F., Sherman, V. O., Tagantsev, A. K., Setter, N., Kaydanova, T., Ginley, D. S. Crossover between extrinsic and intrinsic dielectric loss mechanisms in SrTiO₃ thin films at microwave frequencies. *Appl. Phys. Lett.* **84**, 2385–2387 (2004).
28. Jin, L., Porokhonsky, V. & Damjanovic, D. Domain wall contributions in Pb(Zr,Ti)O₃ ceramics at morphotropic phase boundary: A study of dielectric dispersion. *Appl. Phys. Lett.* **96**, 242902–3 (2010).
29. Tagantsev, A. Mechanisms of dielectric loss in microwave materials. *MRS Online Proc. Libr.* **603**, 221 (1999).

30. Wilke, R. H. T., Moses, P. J., Jousse, P., Yeager, C. & Trolier-McKinstry, S. Wafer mapping of the transverse piezoelectric coefficient, $e_{31,f}$, using the wafer flexure technique with sputter deposited Pt strain gauges. *Sens. Actuators Phys.* **173**, 152–157 (2012).
31. Vendik, O. G., Hollmann, E. K., Kozyrev, A. B. & Prudan, A. M. Ferroelectric tuning of planar and bulk microwave devices. *J. Supercond.* **12**, 325–338 (1999).
32. Newnham, R. E. *Properties of Materials: Anisotropy, Symmetry, Structure*. (Oxford University Press, 2005).
33. Dubois, M.-A. & Muralt, P. Measurement of the effective transverse piezoelectric coefficient $e_{31,f}$ of AlN and $\text{Pb}(\text{Zr}_x\text{Ti}_{1-x})\text{O}_3$ thin films. *Sens. Actuators Phys.* **77**, 106–112 (1999).
34. Noeth, A., Yamada, T., Tagantsev, A. K. & Setter, N. Electrical tuning of dc bias induced acoustic resonances in paraelectric thin films. *J. Appl. Phys.* **104**, 094102 (2008).
35. Berge, J., Vorobiev, A., Steichen, W. & Gevorgian, S. Tunable solidly mounted thin film bulk acoustic resonators based on $\text{Ba}_x\text{Sr}_{1-x}\text{TiO}_3$ films. *IEEE Microw. Wirel. Compon. Lett.* **17**, 655–657 (2007).
36. Berge, J., Norling, M., Vorobiev, A. & Gevorgian, S. Field and temperature dependent parameters of the dc field induced resonances in $\text{Ba}_x\text{Sr}_{1-x}\text{TiO}_3$ -based tunable thin film bulk acoustic resonators. *J. Appl. Phys.* **103**, 064508 (2008).
37. An American national standard IEEE standard definitions of terms associated with ferroelectric and related materials. *IEEE Trans. Ultrason. Ferroelectr. Freq. Control* **50**, 1–32 (2003).
38. Bokov, A. A. & Ye, Z.-G. Recent progress in relaxor ferroelectrics with perovskite structure. *J. Mater. Sci.* **41**, 31–52 (2006).

39. Randall, C. A., Barber, D. J., Groves, P. & Whatmore, R. W. TEM study of the disorder-order perovskite, $\text{Pb}(\text{In}_{1/2}\text{Nb}_{1/2})\text{O}_3$. *J. Mater. Sci.* **23**, 3678–3682 (1988).
40. Randall, C. A., Barber, D. J., Whatmore, R. W., Groves, P., A TEM study of ordering in the perovskite, $\text{PbSc}_{1/2}\text{Ta}_{1/2}\text{O}_3$. *J. Mater. Sci.* **21**, 4456–4462 (1986).
41. Chu, F., Reaney, I. M. & Setter, N. Role of defects in the ferroelectric relaxor lead scandium tantalate. *J. Am. Ceram. Soc.* **78**, 1947–1952 (1995).
42. Samara, G. A. The relaxational properties of compositionally disordered ABO_3 perovskites. *J. Phys. Condens. Matter* **15**, R367 (2003).
43. Rayleigh, Lord. XXV. Notes on electricity and magnetism.—III. On the behaviour of iron and steel under the operation of feeble magnetic forces. *Philos. Mag. Ser. 5* **23**, 225–245 (1887).
44. Taylor, D. V. & Damjanovic, D. Evidence of domain wall contribution to the dielectric permittivity in PZT thin films at sub-switching fields. *J. Appl. Phys.* **82**, 1973–1975 (1997).
45. Bassiri-Gharb, N., Fujii, I., Hong, E., Trolier-McKinstry, S., Taylor, D. V., Damjanovic, D., Domain wall contributions to the properties of piezoelectric thin films. *J. Electroceramics* **19**, 49–67 (2007).
46. N. Bassiri Gharb. Dielectric and Piezoelectric Nonlinearities in Oriented $\text{Pb}(\text{Yb}_{1/2}\text{Nb}_{1/2})\text{O}_3$ - PbTiO_3 Thin Films. Ph.D. dissertation, Dept. of Mat. Sci and Eng., Penn. State University, University Park, PA, 2005.
47. D. V. Taylor. “Dielectric and Piezoelectric Properties of Sol-Gel Derived PZT Thin Films,” Ph.D. dissertation, Dept. des Matériaux, EPFL, Lausanne, CH, 1999.
48. Ichiro Fujii. Dielectric Nonlinearity of Ferroelectrics. Ph.D. dissertation, Dept. of Mat. Sci and Eng., Penn. State University, University Park, PA, 2010.

49. Zubko, P., Catalan, G. & Tagantsev, A. K. Flexoelectric effect in solids. *Annu. Rev. Mater. Res.* **43**, 387–421 (2013).
50. Ma, W. & Cross, L. E. Large flexoelectric polarization in ceramic lead magnesium niobate. *Appl. Phys. Lett.* **79**, 4420–4422 (2001).
51. Tagantsev, A. K. A theory of the flexoelectric effect in crystals. *Zhurnal Eksp. Teor. Fiz.* **88**, 2108–2122 (1985).
52. Ma, W. & Cross, L. E. Flexoelectric polarization of barium strontium titanate in the paraelectric state. *Appl. Phys. Lett.* **81**, 3440–3442 (2002).
53. Tagantsev, A. K. Piezoelectricity and flexoelectricity in crystalline dielectrics. *Phys. Rev. B* **34**, 5883–5889 (1986).
54. Kogan, Sh M. Piezoelectric effect during inhomogeneous deformation and acoustic scattering of carriers in crystals. *Sov. Phys.-Solid State* **5** 2069–2070 (1964).

Chapter 3.

Experimental Procedure

3.1 Preparation of Materials

During the course of the work described in this thesis, samples from multiple sources were investigated. The next sections will discuss the processing for BST thin films developed internally, films provided by collaborating laboratories (sputtered BST), and samples obtained from commercial sources. After a discussion of processing methods, the physical and electrical methodologies and characterization of the aforementioned materials will be reviewed.

3.1.1 Chemical Solution Deposition of BST Thin Films

Thin films of $\text{Ba}_{0.8}\text{Sr}_{0.2}\text{TiO}_3$, $\text{Ba}_{0.7}\text{Sr}_{0.3}\text{TiO}_3$, and $\text{Ba}_{0.6}\text{Sr}_{0.4}\text{TiO}_3$ were deposited by chemical solution deposition (CSD) onto platinized silicon and MgO single crystal substrates. The BST solutions were provided by Albert Queraltó, Mar Tristany and Teresa Puig from ICMAB-CSIC, the Institut de Ciència de Materials de Barcelona- Consejo Superior de Investigaciones Científicas.⁴⁵ The solution chemistry is proprietary, as well as the exact specifications of the deposition process developed by this group, and thus an optimization of the processing parameters was necessary. The solutions were spin coated onto the platinized Si wafers at 6000 rpm for 40 seconds. The films were then pyrolyzed at 250°C and then at 400°C for two minutes each. The pyrolyzed films were then crystallized in a rapid thermal annealer (RTA-600s, Modular Process

Technology Corp.) for one minutes in flowing oxygen at 900°C with a ramp rate of 20 °C/sec. The resulting films exhibited porosity and severe cracking as shown in Figure 3.1.

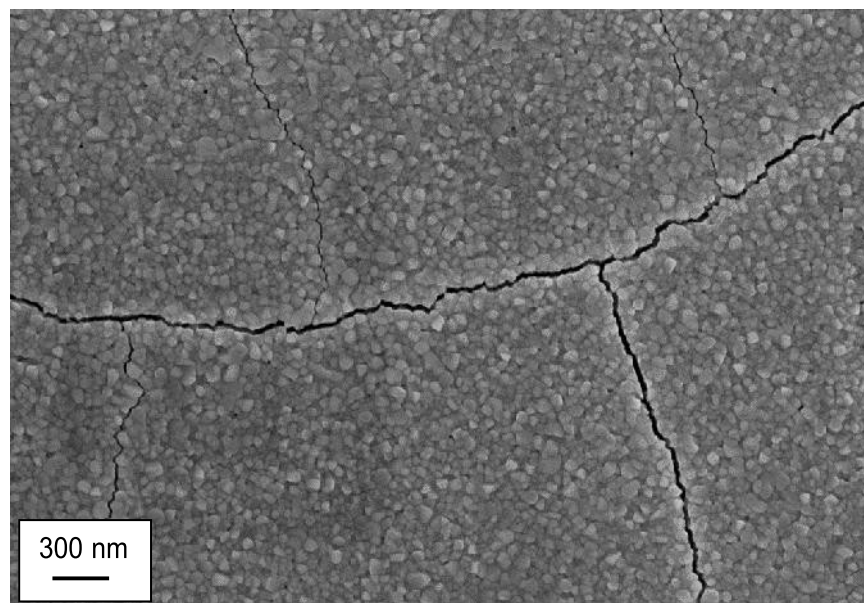


Figure 3.1. Scanning electron micrograph of CSD films on silicon crystallized at 900°C

The cracking in the microstructure was attributed to the difference in coefficient of thermal expansion between silicon and BST at 900 °C. Figure 3.2 shows the difference in coefficient of thermal expansions, CTE, for a series of different substrates in comparison to BST films deposited at 800 °C.¹ The lower thermal expansion of the silicon substrate put the BST film into tension upon decreasing temperature, leading to the production of cracks to relieve the strain. In an effort to decrease the extent of the cracking, the crystallization temperature was decreased from 900 °C to 800 °C. The decrease in crystallization temperature did reduce the number of cracks but did not entirely eliminate cracking.

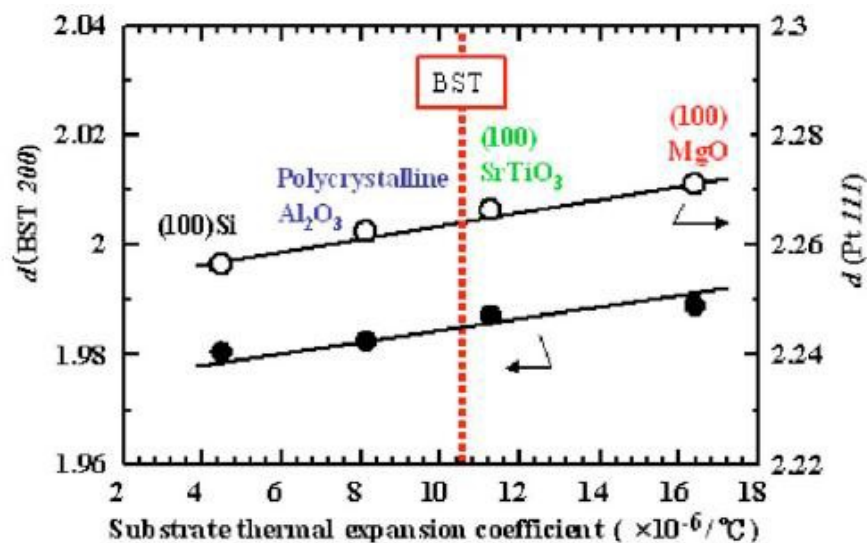


Figure 3.2. Differences in lattice parameters for different substrates as a function of coefficient of thermal expansion compared to BST¹

Another method to avoid the cracking observed in CSD BST films on Si was to employ MgO substrates. The coefficient of thermal expansion is closer to and larger than the CTE of BST, so the films would be put into compression and less likely to crack.¹ Prior to film deposition, the MgO crystals were dehydrated at 1000°C for one minute in flowing oxygen. Immediately afterwards the MgO substrates were placed in the sputter chamber (Kurt Lesker CMS #18) for the deposition of 100 nm of platinum at 750°C in 15% oxygen with a chamber pressure of 5 mTorr.

The BST solutions were spin coated onto the platinized MgO substrates at 6000 rpm for 40 seconds, pyrolyzed at 250°C and then at 400°C for two minutes each and then crystallized for one minutes in flowing oxygen at 900°C with a ramp rate of 20 °C/sec. A scanning electron

micrograph of the films developed through this process is shown in Figure 3.3. The resulting films exhibited large amounts of porosity, and high surface roughness.

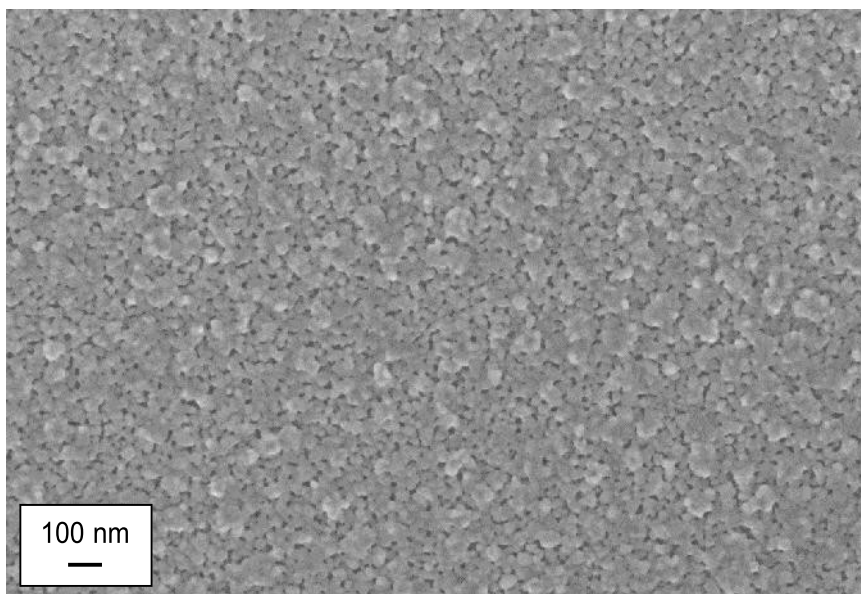


Figure 3.3. Scanning electron micrograph of Ba_{0.6}Sr_{0.4}TiO₃ films deposited crystallized for one minute at 900°C on MgO

The effects of pyrolysis time, crystallization time, ramp rate and solution solubility were investigated with the optimal parameters determined for dense, single phase, crack-free, large grain BST thin films described below. Without being able to investigate the solution chemistry further it is difficult to conclude the exact mechanisms leading to the observed microstructures, however decreases in porosity have previously been observed in dilute BST solutions.² Additionally, BST has been shown to crystallize into a barium strontium carbonate phase prior to the formation of the perovskite phase, which does not decompose until 600°C.³ Increasing the crystallization time was

proposed to remove residual carbonates and had the extra benefit of increasing the grain growth and improve the dielectric response.⁴ So the BST solutions were diluted to 0.1 molarity with the addition of propionic acid (Sigma-Aldrich). The solutions were then spin coated onto the platinized MgO wafers at 6000 rpm for 40 seconds. The films were then pyrolyzed at 250 °C for two minutes, and then 400 °C for twenty minutes. The pyrolyzed films were then crystallized in a rapid thermal annealer (RTA-600s, Modular Process Technology Corp.) for ten minutes in flowing oxygen at 900 °C with a ramp rate of 20 °C/sec. The deposition process was then repeated thirty-four times until the films were approximately 200 nm thick.

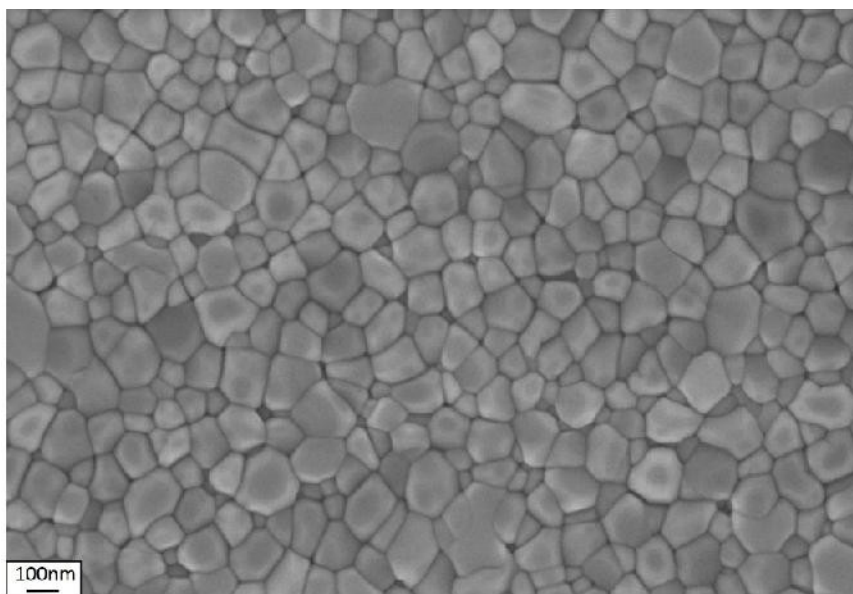


Figure 3.4. Scanning electron micrograph of the Ba_{0.7}Sr_{0.3}TiO₃ thin films deposited onto platinized MgO substrates, showing a dense film

Scanning electron microscopy was employed to determine the grain size and density of the optimized deposited films. The micrographs of the CSD films, shown in Figure 3.4, indicated that the resulting films were dense. No secondary phases or cracks were observed in the micrographs in any CSD film on MgO. The average grain size for the CSD were determined from the SEM micrographs (using Image J: Image Processing and Analysis in Java software) to be approximately 110 nm.

A photolithographic liftoff process was used to deposit 100 nm platinum top electrodes which were then annealed at 550°C for two minutes in flowing oxygen. Circular electrodes with diameters of 75 μm to 1 mm were deposited along with sputtered strain gauges for electromechanical measurements.

3.1.2 Pulsed Laser Deposition of BST Thin Films

Pulsed laser deposition was also explored as a method of BST thin film deposition. $\text{Ba}_{0.7}\text{Sr}_{0.3}\text{TiO}_3$ thin films were deposited onto platinized polycrystalline alumina substrates following the work of Maria, Troler-McKinstry and Scholm.⁵ The processing parameters are as follows:

Table 3.1. Pulsed Laser Deposition of BST Films			
Temperature	700 °C	Deposition Time	20 min
Energy Density	1.5 J/cm ²	Substrate-Target Distance	6 cm
Frequency	10 Hz	Atmosphere	50 mTorr (10% Ozone in Oxygen)

The resulting films exhibited highly faceted triangular grains, porosity, and deeply grooved grain boundaries, as shown in Figure 3.5. The grain boundary grooving and porosity inhibited electrical measurements due to electric field concentration and infant failures.

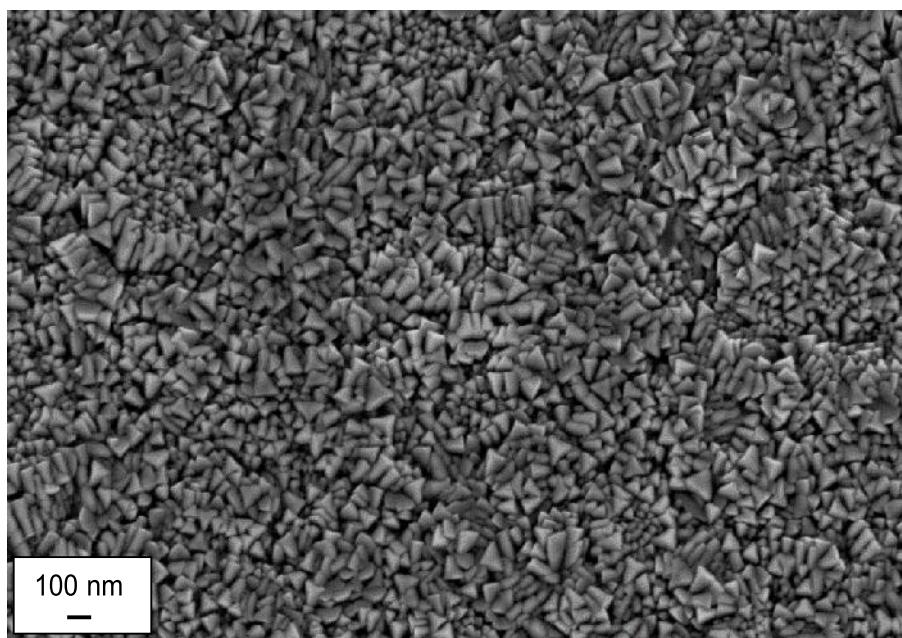


Figure 3.5. First set of pulsed laser deposited Ba_{0.7}Sr_{0.3}TiO₃ thin films on platinized alumina substrates deposited at 700°C with an energy density of 1.5 J/cm²

In an effort to reduce the surface faceting and grain boundary grooving, the energy density was decreased and the substrate-target distance slightly increased. The processing parameters were adjusted to an energy density of approximately 1.25 J/cm^2 , and the distance was increased to 7 cm, while everything else was held constant. The resulting films exhibited a trimodal grain structure, with intermixed triangular, plate-like and rectangular grains. Again the deep intergranular grooving and porosity prevented electrical measurements. As a result, this method was not investigated further for the deposition of BST thin films.

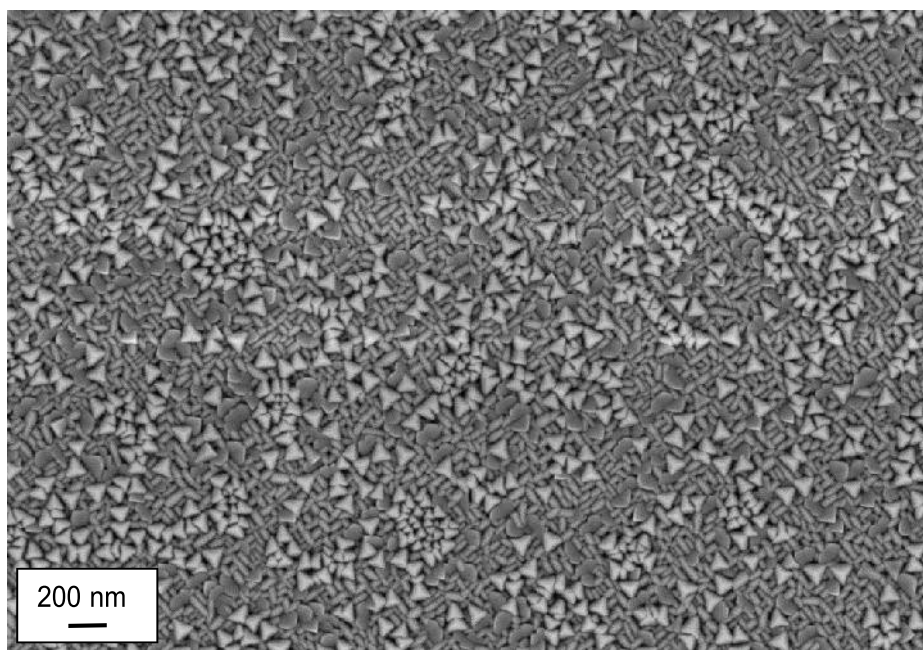


Figure 3.6. Pulsed laser deposition of Ba_{0.7}Sr_{0.3}TiO₃ thin films on alumina substrates grown at a laser energy density of 1.25 J/cm^2

3.1.3. Sputter Deposition of BST Thin Films

Sputter deposited films were provided by Dr. Jon-Paul Maria's group at the North Carolina State University. These $\text{Ba}_{0.7}\text{Sr}_{0.3}\text{TiO}_3$ thin films were deposited onto polished polycrystalline copper and Al_2O_3 substrates by RF-magnetron sputtering to a film thickness of approximately $0.5\ \mu\text{m}$ after 60 minutes. A post anneal was done *ex-situ* at $900\ ^\circ\text{C}$ in air for 20 hours with a heating ramp rate of $20\ ^\circ\text{C}/\text{min}$. The details of this process are described in Table 3.2.⁶ A photolithographic liftoff process was used to deposit interdigitated platinum electrodes on the BST samples on alumina with a finger length of $1000\ \mu\text{m}$, a width of $6\ \mu\text{m}$, and a separation distance of $6\ \mu\text{m}$, with 32 fingers per side. Sputtered films on copper employed circular platinum top electrodes from 1 mm to approximately $100\ \mu\text{m}$. Following deposition, the electrodes were annealed at $550\ ^\circ\text{C}$ for two minutes in flowing oxygen. Interdigitated top electrodes were used in order to avoid deterioration of the platinum bottom electrode during the extended annealing process. The average grain size, determined from scanning electron micrographs, of the sputtered films was approximately $95\ \text{nm}$.

Table 3.2. Sputter Processing Conditions			
Power	250W	Temperature	$300\ ^\circ\text{C}$
Base Pressure	1.0×10^{-5} Torr	Deposition Time	66 min
Pressure	10 mTorr	Annealing Temperature	$900\ ^\circ\text{C}$
Sputtering Gas	Argon	Annealing Time	20 hrs
Gas Flow	15 sccm	Thickness	380 nm

3.1.4. Materials from Commercial Sources

Two sets of ceramic BST samples with an approximate composition of $\text{Ba}_{0.67}\text{Sr}_{0.33}\text{TiO}_3$ and $\text{Ba}_{0.7}\text{Sr}_{0.3}\text{TiO}_3$ (as estimated by the temperature dependence of the permittivity), were used as a point of comparison in the studies on residual ferroelectricity and flexoelectricity. These materials were developed at Texas Instruments for long wavelength infrared dielectric microbolometer applications which required strict control of the dielectric response as a function of temperature.⁹ As such, although the exact processing parameters are proprietary, it is known that strict processing control was maintained with regards to the A-site stoichiometry. These same samples also were used in the work of Ma and Cross in studies on flexoelectricity in BST.⁹

For the calibration of the $e_{31,f}$ (Electric field and strain) piezoelectric measurement system, an intrinsically piezoelectric material was required. Lead zirconate titanate thin films were chosen as the standard for calibration in this study. The films were sputtered lead zirconate titanate, $\text{Pb}(\text{Zr}_{0.52}\text{Ti}_{0.48})\text{O}_3$, thin films provided by ULVAC Technologies, Inc.. These films were 1 μm in thickness. Electrode size and deposition method were consistent with the methods used on barium strontium titanate thin films. Prior to $e_{31,f}$ measurements dielectric and polarization electric field loops were measured.

3.2 Physical Characterization and Methods

Scanning electron microscopy and x-ray diffraction were used to verify the phase and quality of the deposited films and ceramics. Transmission electron microscopy was also used in conjunction with electron energy loss spectroscopy and energy dispersive spectroscopy to

investigate the chemical inhomogeneity in BST thin films. Film thickness measurements were made on a (Tencor 500) profilometer.

3.2.1 Scanning Electron Microscopy

All of the micrographs shown within this section were taken on a Leo 1530 field emission scanning electron microscope. The working distance was kept within 1.6 - 2.2 mm with an accelerating electric voltage of 3 kV. An in-lens electron lens was used and no degradation or charging were observed in subsequent micrographs. Image J software was then used to extract the average grain size from highly contrasted micrographs.

3.2.2 X-Ray Diffraction

The crystallinity and phase of the BST films were characterized by X-ray diffraction (PANalytical XPert Pro MPD). Figure 3.7 shows the x-ray diffraction patterns for the CSD and sputtered $\text{Ba}_{0.7}\text{Sr}_{0.3}\text{TiO}_3$ thin films. In both cases, the patterns were indexed to that of cubic bulk ceramic BST of the same composition. No second phases or peak splitting, associated with a ferroelectric phase, were observed in any film. The full width-half maxima of the sputtered films was over three times that of the CSD films, which might be a result, in part, of differences in chemical inhomogeneity.

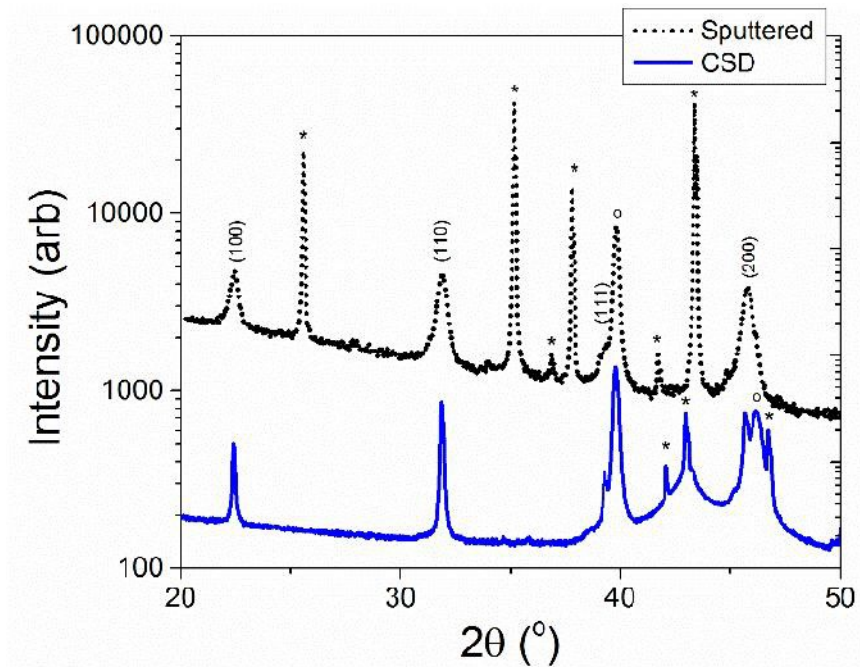


Figure 3.7. X-ray diffraction pattern for sputtered and CSD $\text{Ba}_{0.7}\text{Sr}_{0.3}\text{TiO}_3$ thin films deposited on $\text{Al}_2\text{O}_3/\text{MgO}$ substrates respectively. Substrate and electrode peaks indicated by * and °.

The lattice parameters and volumes were calculated from the peak fitting of the x-ray diffraction patterns shown in figure 3.7 using Jade software (Materials Data Inc.). The results are shown in Table 3.3. All films were found to be cubic, indicating that these materials are in the paraelectric phase.

Table 3.3. Lattice parameters and lattice volumes calculated from X-ray diffraction in figure 3.7

	a(Å)	Lattice Volume (Å³)
CSD Ba _{0.7} Sr _{0.3} TiO ₃	3.9765±0.001	62.879
Sputtered Ba _{0.7} Sr _{0.3} TiO ₃	3.9600±0.0029	62.099

3.2.3. Transmission Electron Microscopy and Electron Energy Loss Spectroscopy

Transmission electron microscopy measurements were made by the group of Dr. Elizabeth Dickey at the North Carolina State University. Electron energy loss spectroscopy (EELS) experiments were performed to assess nano-scale stoichiometry. Cross sectional samples were prepared for EELS by either focused ion beam (FIB) preparation or mechanical polishing and subsequent ion milling. FIB samples were prepared with a FEI Quanta 3D-FEG dual-beam focused ion beam, including a final mill of 2 kV to minimize sample damage. Ion milling was performed on the mechanically polished samples using a EA Fischione Model 1010 ion mill at a voltage of 0.7-2.5 kV, current of 5 mA and milling angles of 6-10° at minus 100°C to minimize sample damage. A probe-corrected FEI Titan G2 60-300 kV S/TEM equipped with an X-FEG source and a Gatan Quantum electron energy loss spectrometer was utilized. The microscope was operated at 200 kV and the energy resolution was ~0.8 eV for all spectra obtained.

Gatan DigitalMicrograph™ software was used to perform EELS spectral analysis. For this work, EELS spectrum images were taken from the bulk of the samples with pixel sizes around 2x2 nm and an image over an area of over 300 nm². Because of thickness variations across the samples, it was necessary to remove plural scattering contributions to the spectra. This was done using the

Fourier-ratio method, where the Fourier transform of the core-loss spectrum is divided by the Fourier transform of the low loss spectrum.¹⁰ Quantification of EEL spectra was then performed by using the theoretical scattering cross-sections of barium and titanium using the Hartree-Slater model.¹¹ The equation to find the concentration is shown below:

$$C_{\text{Ba}}/C_{\text{Ti}} = \sigma_{\text{Ba}}(\beta, \Delta) / \sigma_{\text{Ti}}(\beta, \Delta) \times I_{\text{Ba}}(\beta, \Delta) / I_{\text{Ti}}(\beta, \Delta)$$

where σ_i is the partial scattering cross-section determined at β , the collection angle, Δ , the edge integration width, C_i is the calculated concentration and I_i is the integrated intensity from the background-subtracted EEL spectra.

The Ba/Sr ratio could not be directly identified from the strontium L- and barium M4,5-edges as the intensity of the Sr L-edge is too weak and far removed from the Ba edge for direct quantitative comparisons. To circumvent this experimental difficulty, the Ba/Sr ratio was calculated assuming a 1:1 ratio of the A-site and B-site cations. This enabled use of the Ba M4,5 and the Ti-L edges for quantification. Any calculated difference intensity ratios then corresponds to a difference in Ba/Sr ratio. The EELS maps were 16x6 with pixel size of 2.05 nm x 2.05 nm.

3.3. Electrical Characterization

This section discusses the methods of electrical characterization used within this study. Additionally, the temperature dependence of the dielectric and Rayleigh response are reviewed.

3.3.1. Dielectric Measurements

Capacitance and dielectric loss tangent were measured on six to ten electrodes for each sample prior to other electrical measurements. With the thickness, t , and electrode area, A , known, the permittivity can be calculated from the capacitance from:

$$\varepsilon = \frac{Ct}{\varepsilon_0 A}$$

where ε_0 is the permittivity of free space.¹² All capacitance and loss tangent measurements were taken at 1 kHz and 30 mV unless otherwise specified. All dielectric and tunable measurements were taken on a precision LCR meter (Hewlett Packard 4284A).

Thin film dielectric temperature dependence was measured using a Peltier heating stage (Temptronic) on a Cascade Probe Station. The temperature was monitored by a type-K thermocouple on the surface of the sample, and read via a digital multimeter (Hewlett Packard 3478). The sample were first heated above the T_{\max} , approximately 50 °C, prior to any temperature measurement. Temperature measurements were taken first on increasing then decreasing temperature over the temperature range from -60 °C to 200 °C. For ceramic measurements the temperature response was measured with a Delta design 2300 heating/cooling oven, monitored by again by a type-k thermocouple.

3.3.2. Rayleigh Analysis

Rayleigh analysis was conducted as a function of temperature and frequency using a precision LCR meter (Hewlett Packard 4284A). For thin film measurements, the heating and cooling were

controlled by a Peltier heater, monitored by a type-K thermocouple on the surface of the sample, and read via a digital multimeter (Hewlett Packard 3478). Samples were allowed to equilibrate for five minutes at the highest temperature. Subsequent temperature steps had a tolerance of 1 °C with a hold for two minutes before making a measurement. The temperature range was chosen to span the global transition temperature determined from the dielectric temperature response. Rayleigh behavior was characterized from 100 Hz to 1 MHz.

3.3.3 Current-Voltage Measurements

Leakage current measurements were taken on a 4140 pico-Ampere Meter/DC Voltage Source (Hewlett Packard). Prior to any current-voltage measurements, the time dependent current under constant voltage was measured in order to determine the steady state conditions. Temperature dependent leakage current measurements were acquired using the same methodology as is used for measuring dielectric temperature dependence.

3.3.4 Polarization-Electric Field Loops

Thin film polarization-electric field measurements were taken on a Precision Multiferroic materials analyzer (Radiant Technologies, Inc.). Measurements were made on increasing voltage to failure in increments of 1 V for minor loops and 20 V for major loops. All reported data is the average of ten consecutive, electric field sweeps with the same initial polarity. The frequency of the applied electric field was 100 Hz unless otherwise specified. For bulk polarization-electric

field data, measurements were taken on custom charge integrator in conjunction with an amplifier (Kepco Power Supplies).

3.4. Other Measurements

3.4.1. Second Harmonic Generation

Second harmonic generation was conducted in barium strontium titanate ceramics and thin films. An Instec Inc. temperature system with liquid nitrogen coolant was used to control the sample temperature. A 800 nm 90 femtosecond laser (Coherent Inc) was used with a final frequency of 2 kHz. The sample was placed 8.5 cm away from the focus. The signal was collected by a photo multiplier tube (Hamamatsu H7826) and a lock-in amplifier with a 4.65 k Ω with an OD filter of 0.3-1.5.

3.4.2. Piezoresponse Force Microscopy

Piezoresponse force microscopy, PFM, was conducted on barium strontium titanate based ceramic samples provided by Texas Instruments. Samples were cut from the BST bulk ceramics and prepared for PFM by polishing. Samples were mounted onto a polishing disc with crystal bond and bounded on each side with a glass slide in order to insure level polishing as shown in Figure 3.8. The samples were polished with 30 μm , 15 μm and 9 μm Al₂O₃ grit for approximately three minutes each, followed by 6 μm , 3 μm , 1 μm diamond grit for ten to fifteen minutes each and then 0.5 μm diamond grit for thirty minutes to an hour. One sample set was then annealed at approximately 275 °C for 2 hours to remove residual surface strain induced during polishing.

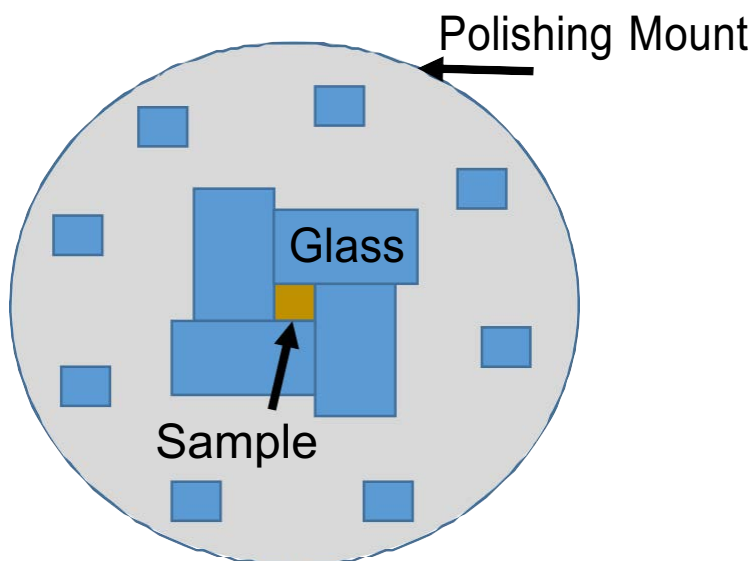


Figure 3.8. Schematic of the polishing set up for BST PFM samples

The samples were then mounted with silver paste to a Peltier heater/cooler (Marlow Industries). The heater was controlled via a thermistor feedback loop and temperature control system (Thorlabs). The thermistor was mounted on the top surface of the sample with silver epoxy. In addition to the thermistor, a K-type thermocouple, read via a digital multimeter (Hewlett Packard 3478), was attached to the surface of the sample to monitor the surface temperature. To ensure temperature equilibrium, samples were maintained at each temperature for ten minutes and the surface temperature verified prior to PFM. A 2 N/m platinum coated tip (HQ:NSC 36/Pt) was used on a Bruker atomic force microscopy system. Contact mode piezoresponse force microscopy was used to image the lateral and vertical local piezoelectric response. The laser position was calibrated using an internal standard. Prior to imaging, frequency sweeps from 100 kHz to 10 MHz were taken for the tip-sample system in order to identify the system resonance. Signals ranging from 100 mV up to 10 V were applied at 750 kHz. The scan size was from 1-5 μm , and the images

were made by scanning at 90° angle to the cantilever length. Images were taken in approximately the same location for every temperature set.

3.5. References

1. Ito, S., Funakubo, H., Koutsaroff, I. P., Zelner, M. & Cervin-Lawry, A. Effect of the thermal expansion matching on the dielectric tunability of (100)-one-axis-oriented (Ba_{0.5}Sr_{0.5})TiO₃ thin films. *Appl. Phys. Lett.* **90**, 142910–142910–3 (2007).
2. Hoffmann, S. & Waser, R. Control of the morphology of CSD-prepared (Ba,Sr)TiO₃ thin films. *J. Eur. Ceram. Soc.* **19**, 1339–1343 (1999).
3. Gust, M. C., Momoda, L. A., Evans, N. D. & Mecartney, M. L. Crystallization of Sol–Gel-Derived Barium Strontium Titanate Thin Films. *J. Am. Ceram. Soc.* **84**, 1087–1092 (2001).
4. Tahan, D. M., Safari, A. & Klein, L. C. Preparation and Characterization of Ba_xSr_{1-x}TiO₃ Thin Films by a Sol-Gel Technique. *J. Am. Ceram. Soc.* **79**, 1593–1598 (1996).
5. Maria, J.-P., Trolier-McKinstry, S. & Schlom, D. G. Size effects in barium titanate thin film heterostructures with conductive oxide electrodes. in *Proc. Tenth IEEE Int. Symp. Appl. Ferroelectr. 1996 ISAF 96* **1**, 333–336 vol.1 (1996).
6. P.G. Lam, V. Haridasan, M.B. Steer, A.I. Kingon, and J.-P. Maria. *IEEE Transactions on Ultrasonics, Ferroelectrics and Frequency Control* **59**, 198–204 (2012).
7. Park, J. H., Xu, F. & Trolier-McKinstry, S. Dielectric and piezoelectric properties of sol–gel derived lead magnesium niobium titanate films with different textures. *J. Appl. Phys.* **89**, 568–574 (2001).

8. Keech, R., Shetty, S., Kuroda, M. A., Liu, X. H., Martyna, G. J., Newns, D. M., Trolier-McKinstry, S Lateral scaling of $\text{Pb}(\text{Mg}_{1/3}\text{Nb}_{2/3})\text{O}_3\text{-PbTiO}_3$ thin films for piezoelectric logic applications. *J. Appl. Phys.* **115**, 234106 (2014).
9. Ma, W. & Cross, L. E. Flexoelectric polarization of barium strontium titanate in the paraelectric state. *Appl. Phys. Lett.* **81**, 3440–3442 (2002).
10. Egerton, R. F. & Whelan, M. J. The electron energy loss spectrum and band structure of diamond, Springer, New York, (1974).
11. Slater, J.C. A simplification of the Hartree-Fock method. *Phys Rev.* **81**. 3, 385 (1951).
12. Moulson, A. J., Herbert, J. M. *Electroceramics: Materials, Properties, Applications*. (John Wiley & Sons, 2003).

Chapter 4

$e_{31,f}$ (Electric Field and Strain)

4.1. Introduction

Barium strontium titanate thin film tunable dielectrics are becoming a viable technology for frequency agile applications, but still suffer from comparatively high loss in the microwave region.^{1,2} Although nominally operated in the cubic paraelectric phase the application of a DC electric field to a barium strontium titanate, BST, thin film during tuning spoils the center of symmetry, allowing for the development of piezoelectric responses.^{3,4} Electric field induced piezoelectricity creates resonances detectable in the impedance spectra which act as a loss mechanism in tunable dielectrics, or as an active property in tunable thin film bulk acoustic resonators.⁵ Resonances in the low GHz have previously been reported for 200-400 nm thick BST thin films, well within the frequencies of interest for RF tunable applications.⁶ Avoiding or employing induced piezoelectric resonances necessitates predictive models of the impedance response over the frequencies and electric fields of interest.^{3,7} Modeling the induced piezoelectric impedance resonances requires an understanding of the material response under electric field, which is rarely directly measured.^{6,7}

This work provides direct measurements of the DC electric field induced $e_{31,f}$ piezoelectric response and tunability for barium strontium titanate, BST, thin films with different compositions and varied strain states. The electric field dependence of the piezoelectric and dielectric response is related to the development of induced piezoelectric resonances through the piezoelectric coupling coefficient, k which is determined from:

$$k_{31} = \frac{e_{31,f}(s_{11}^E + s_{12}^E)}{\sqrt{\frac{2}{(s_{11}^E + s_{12}^E)\epsilon_3^T}}}$$

where the $e_{31,f}$ is the transverse piezoelectric coefficient, s_{11} and s_{12} are component of the elastic compliance matrix and ϵ is the permittivity at constant stress.^{8,9} Once the piezoelectric coupling coefficient and the device dimensions are known, the induced piezoelectric resonances can be predicted or avoided.

This work also covers the development and calibration of the piezoelectric metrology used to determine the electric field and strain dependency of the piezoelectric response in thin film material. Induced electric field and strain effects on the piezoelectric response of BST films measured using this metrology are discussed. Rayleigh analysis is employed to characterize the residual ferroelectric response observed in the nominally paraelectric BST thin films.

4.2 Development of $e_{31,f}$ (Electric Field and Strain) Measurement System

A schematic of the measurement system is shown in Figure 4.1 and an image of the system in operation is shown in Figure 4.2. Samples were mounted onto cantilevers made from silicon wafers with a minimum 1:4 width:length ratio so that they could be flexed to produce a known strain. A shielded piezoelectric stack actuator (Kinetic Ceramics) was used to periodically flex the cantilever for the $e_{31,f}$ measurement. For larger applied static strains, the actuator stage was moved up by a micrometer. The drive signal for the piezoelectric stack actuator was generated by a lock-in amplifier (Stanford Research SR830 DSP) at 4 Hz. In order to measure the strain at the surface

of the sample, two strain gauges (Omega) were attached to the surface of the sample with one parallel and the other perpendicular to the long axis the cantilever.

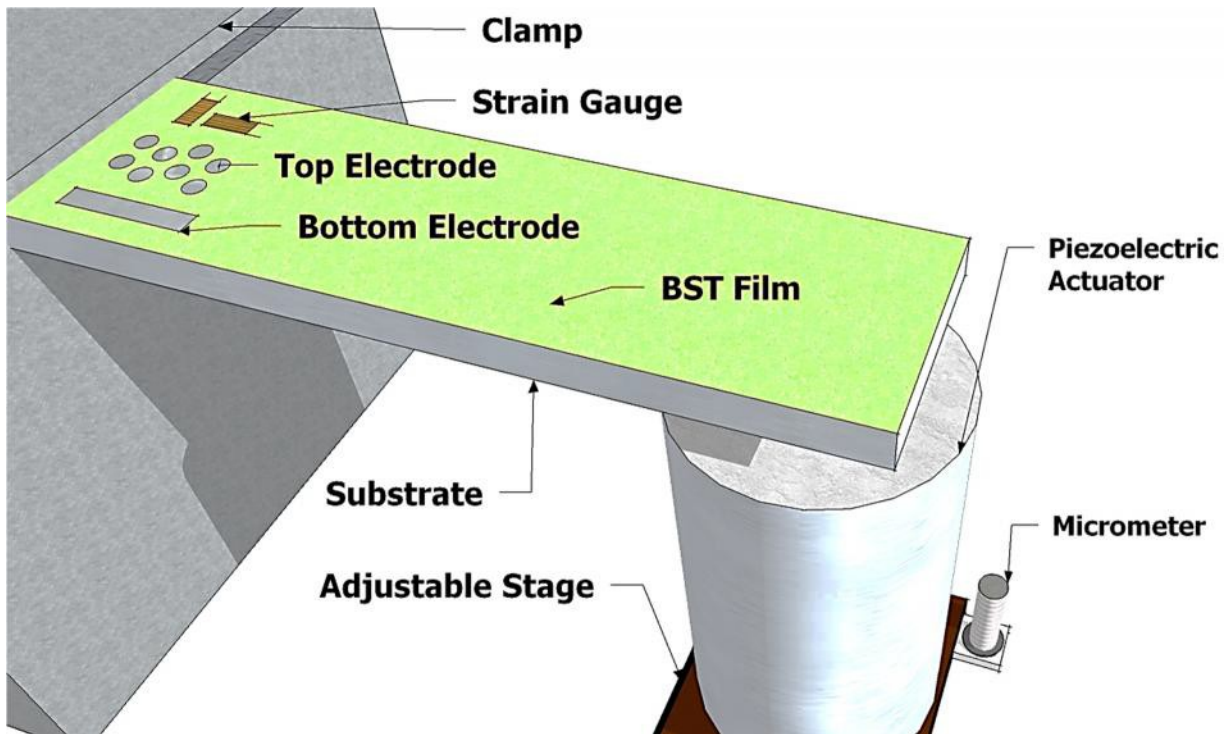


Figure 4.1. Schematic of the $e_{31,f}$ (electric field, strain) metrology and sample

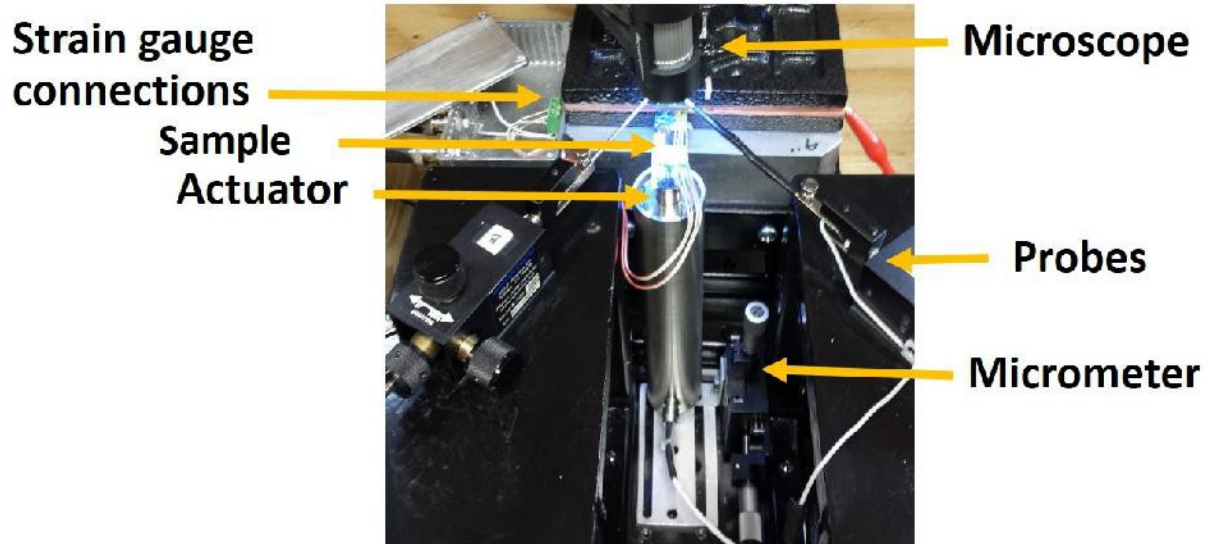


Figure 4.2. Image of $e_{31,f}$ (Electric field and Strain) measurement system in operation

Sinusoidal strain measurements were made using a quarter Wheatstone bridge configuration, shown in Figure 4.3, and a lock-in amplifier with a thirty second time constant and 24 dB settling. The charge was measured simultaneously with a custom charge integrator circuit, shown in Figure 4.4, with a feedback loop optimized for 4 Hz, and read with a lock-in amplifier (Stanford Research SR830 DSP) with a thirty second time constant and 24 dB settling.

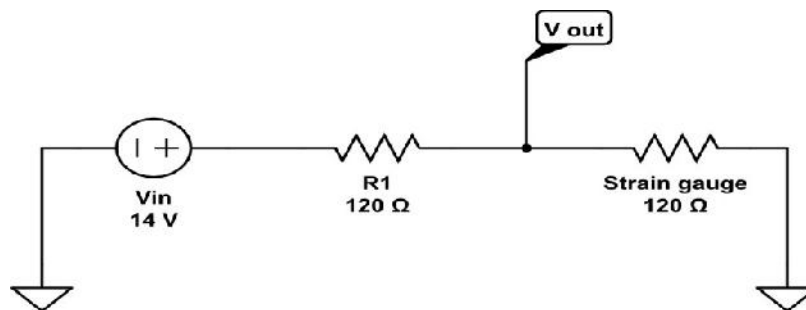


Figure 4.3. Quarter Wheatstone bridge circuit used for dynamic strain measurements

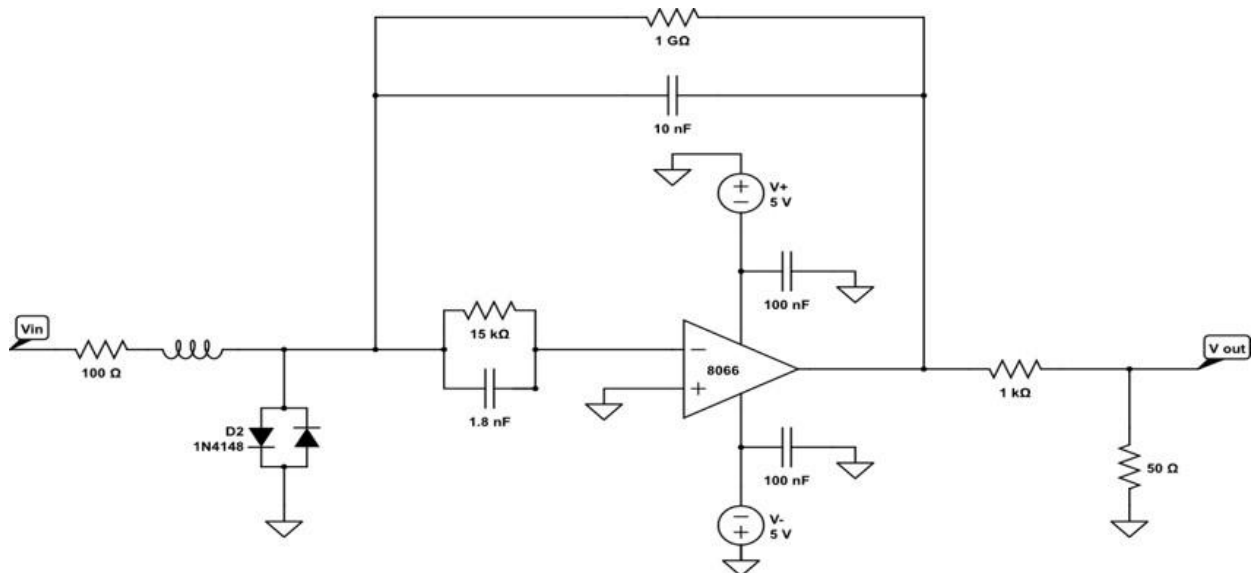


Figure 4.4. Schematic of the charge to voltage converter used in the charge portion of the piezoelectric measurements

From the charge and strain measurements the $e_{31,f}$ coefficients were calculated as:

$$e_{31,f} = \frac{Q}{A(x_1 + x_2)}$$

where Q is the charge, x is the applied strain and A is the area of the electrode. For the DC electric field $e_{31,f}$ measurements and leakage current measurements, the electric field was generated by a pA meter (HP 4140) and applied to the bottom electrode of the sample. The range of applied DC electric field used to measure $e_{31,f}$ was less than fields which initiated either degradation or breakdown.

4.3 Calibration of the $e_{31,f}$ (Electric field and Strain) Measurement System

The uniaxial $e_{31,f}$ (Electric field and Strain) measurement system was calibrated against a biaxial $e_{31,f}$ measurements system. An intrinsically piezoelectric thin film was used as standard. A $1\mu\text{m}$ thick, sputtered $\text{Pb}(\text{Zr}_{0.52}\text{Ti}_{0.48})\text{O}_3$, (ULVAC Technologies Inc.), film was used as this standard. Sample from this film were mounted onto silicon wafers or cantilevers for either the biaxial or uniaxial measurements respectively. Two strain gauges (Omega) were attached to the surface of the samples with a cyanoacrylate-based glue. For the uniaxial system these gauges were oriented parallel and perpendicular to the long axis the cantilever. Prior to strain measurements the resistance of the gauge was verified to be within 120 ± 1 Ohms. In both measurement systems, the drive signal was generated by a lock-in amplifier (Stanford Research SR830 DSP). To make concurrent strain and charge measurements, three lock-ins where connected together and the settings for each were kept at 4 Hz, with a 30 second time constant, and a 24 dB settling time. In both measurement systems, the samples were poled at 15 V for 15 minutes and were let sit for ten minutes prior to making measurements. The phase output was used to gauge the quality of the strain gauge attachment or thin film response. Calibration samples were limited to those with less than ten degrees phase output for the strain gauges and greater than 170 degrees for the charge output. Dynamic strain measurements were made using a quarter Wheatstone bridge configuration, shown in Figure 4.3 and the charge measurements were made simultaneously with a custom charge integrator circuit, shown in Figure 4.4, with a feedback loop optimized for 4 Hz. The output from the $e_{31,f}$ (Electric field and Strain) strain and charge measurement circuits were simultaneous checked against the exact same circuits used in the biaxial $e_{31,f}$ measurement system. No significant differences were observed between the measurement circuits.

The calibration measurements taken on these two systems were found to be in good agreement, as shown in Table 4.1. The variation in measurement between the two systems was within variations previously noted due to the gluing of the strain gauges. The standard deviations for the measured charge in both systems were determined for a range of electrode sizes to be less than 5 %. The standard deviation for a single strain measurement in the $e_{31,f}$ (Electric field and Strain) is approximately 4.7 % of the base strain value over six hours. The total uncertainty in this uniaxial system, is approximately 6 % due to the variations in the gluing of the strain gauges onto the samples. This uncertainty is similar to the results for the biaxial $e_{31,f}$ system. It is possible that the uncertainty in this measurement could be reduced further using platinum sputtered strain gauges directly on the surface of whole wafer parts.

Table 4.1 Calibration of the $e_{31,f}$ (Electric Field and Strain) Measurement System

	$e_{31,f}$ (Electric Field and Strain)	$e_{31,f}$ (biaxial)
	(C/m ²)	(C/m ²)
Average	-4.7 ± 0.3	-5.3 ± 0.4
Standard deviation	0.4	0.3

4.4. $\epsilon_{31,f}$ (Electric Field) in BST

Prior to $\epsilon_{31,f}$ measurements, the dielectric temperature dependence was measured in order to determine the paraelectric to ferroelectric transition temperature and ensure that the films were in the paraelectric phase. Table 4.2 includes the maximum temperature of the dielectric response, taken as the ferroelectric phase transition temperature, for each film. The transition temperatures were much lower than expected for an unstrained homogeneous composition of 70:30 or 60:40 barium to strontium ratio⁸; the most critical feature for this work is that the films are well within the paraelectric phase regime and thus should not be intrinsically piezoelectric. The transition temperature was shown to be relatively insensitive to the application of electric field. The x-ray diffraction results, such as the calculated lattice parameters and absence of peak splitting, corroborate room temperature paraelectricity. The dielectric response of these films exhibited broad transitions and significant frequency dispersion in both the permittivity and dielectric loss, indicating possible relaxor-like ferroelectric trends.¹⁰

Table 4.2. Transition temperature, tunability, dielectric loss and Rayleigh behavior for BST films at 100kHz

Sample	T_{\max}	Relative Tunability	$\tan\delta(0)$	ϵ_{init}	α (kV/cm) ⁻¹
Ba _{0.7} Sr _{0.3} TiO ₃ on Si	< -60°C	36.9 %	0.016	340	0.025 ± 0.001
Ba _{0.7} Sr _{0.3} TiO ₃ on MgO	-22°C	83.1 %	0.011	1640	1.61 ± 0.074
Ba _{0.6} Sr _{0.4} TiO ₃ on MgO	< -60°C	70.7 %	0.004	950	-0.144 ± 0.008

The electric field induced $e_{31,f}$ piezoelectric response for the BST thin films is shown in Figure 4.5. All samples in this study displayed a finite unbiased piezoelectric response despite being within the paraelectric phase regime. Each film went through a minima on increasing and decreasing field at approximately 10 kV/cm, implying an initial preferred polarization state. For all samples, uncertainty in the field induced $e_{31,f}$ response increased with increasing applied electric field even though the applied electric field was kept below the electric fields need for degradation determined by prior leakage current measurements. Field induced $e_{31,f}$ for the 60:40 BST on MgO and the 70:30 BST on Si films were both comparatively linear with a slope of 2.6×10^{-4} and $1.4 \times 10^{-4} \text{ C/kVm}$ respectively from 10-120 kV/cm. The 70:30 BST films on MgO exhibited significant hysteresis on sweeping applied electric field, which is consistent with the alignment of ferroelectric domains.⁸ The BST 70:30 films on MgO displayed a larger initial slope; the induced $e_{31,f}$ value saturated above 70 kV/cm, reaching a value similar to that of the 60:40 BST films.

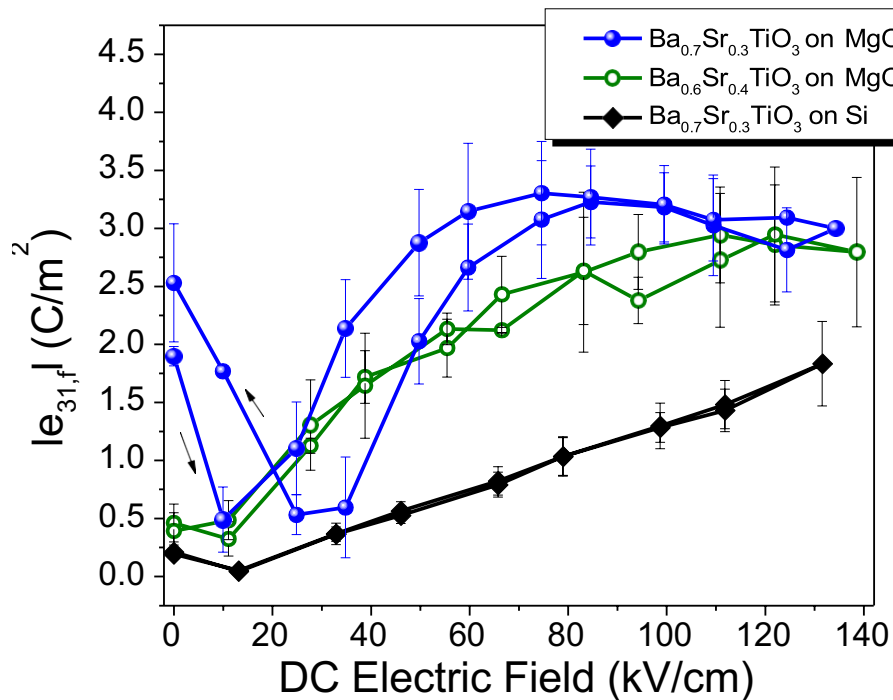


Figure 4.5. A comparison of the transverse piezoelectric response, $e_{31,f}$, as a function of applied DC electric fields for BST films with varied compositions and substrates

The DC electric field dependence of the permittivity, the tunability, is shown in Figure 4.6. Table 4.2 provides the calculated positive voltage tunability and unbiased dielectric loss tangent at 100 kHz. The permittivity and dielectric loss for the films on platinum-coated silicon are consistent with previous observations.^{11,12} The relative tunability of the 70:30 BST and 60:40 BST films on MgO is 83 % and 70 % respectively with a dielectric loss < 0.01 .^{13,14} The 70:30 BST films on MgO displayed significant imprint, over 25 kV/cm, in both $e_{31,f}$ and tunability, suggesting an internal bias, possibly due to aligned defect dipoles.^{15,16} Additionally, these films had significant hysteresis and enhanced loss, both possible indications of an induced ferroelectric response. These

results are at odds with the dielectric temperature dependence, which indicate that these films should be neither ferroelectric nor piezoelectric.

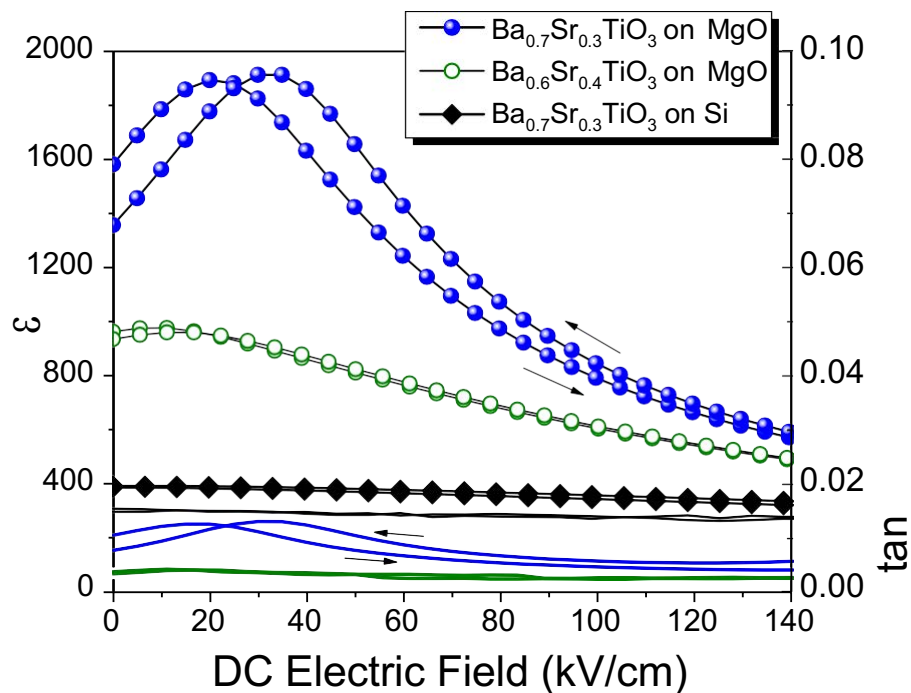


Figure 4.6. Tunability and DC electric field dependence of the dielectric loss tangent in BST films with varied composition and substrate

Polarization-electric field loops and Rayleigh analysis were employed to investigate the discrepancies between the paraelectric and ferroelectric behavior in these films. The polarization-electric field loops were exceptionally narrow, with coercive fields below 0.5 kV/cm for all films. The irreversible Rayleigh parameter was used to monitor the presence of ferroelectricity through the movement of domain walls, cluster or phase boundaries with applied AC electric field.^{17,18} The

normalized irreversible Rayleigh response for each of the films is shown in Figure 4.7. In the 70:30 BST films the observed increase in permittivity with AC electric field indicates that a finite residual ferroelectric response persists in these samples at room temperature, approximately 40°C above the global ferroelectric transition temperature. In the 60:40 BST films, however, the irreversible response is negative, which is consistent with a paraelectric phase. Residual ferroelectricity above the global ferroelectric phase transition temperature has been previously observed 50°C above the phase transition temperature.¹⁹ Residual ferroelectric and piezoelectricity could be due to composition disorder, which has been shown previously to have large effects on ferroelectric and relaxor properties,²⁰ or related to the mixed order-disorder/displacive phase transition phenomena in barium titanate based materials.²¹ The presence of residual ferroelectricity and piezoelectricity are further indicated by an increased dielectric loss, deviations from Curie-Weiss, hysteretic tunability and enhanced unbiased piezoelectricity in the BST thin films.²² Large and hysteretic piezoelectric and tuning responses were observed in the 70:30 BST thin films on MgO which was consistent with the positive irreversible Rayleigh behavior, indicating a ferroelectric contribution to the piezoelectric and dielectric response.

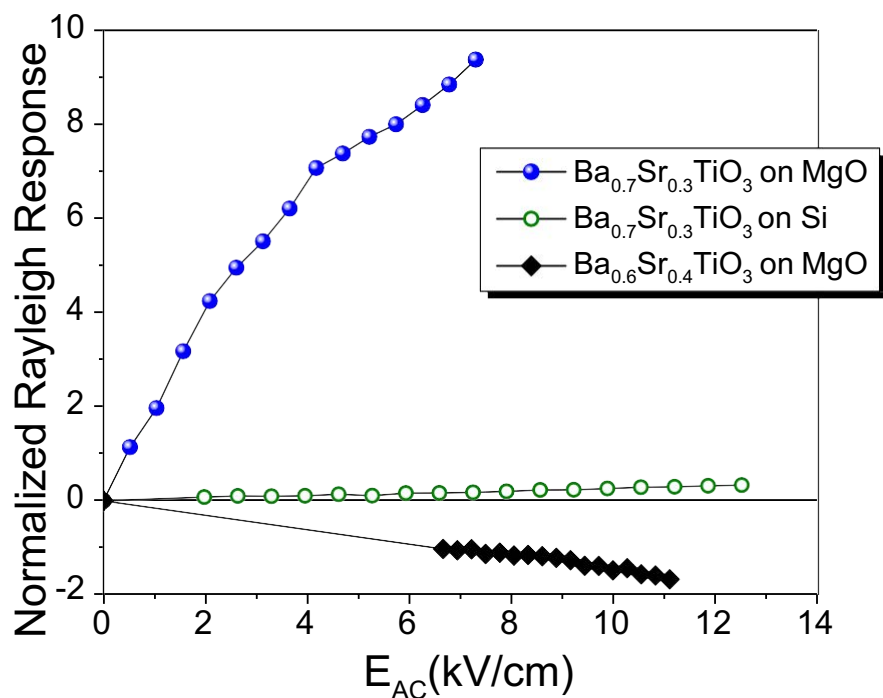


Figure 4.7. Normalized irreversible Rayleigh behavior for 70:30 BST on MgO and Si, and 60:40 BST on MgO thin films

The application of the DC electric field does not significantly impact T_{max} of the BST 70:30 or 80:20 thin films on MgO determined from the dielectric temperature dependence. For the 80:20 films the maximum in permittivity with temperature was suppressed nearly 5 °C with the application of approximately 200 kV/cm. No significant shift was observed in the BST 70:30 or 60:40 thin films on MgO. This indicates that the observed ferroelectric response is not due to a shifting of the ferroelectric transition temperature to room temperatures, over 40 °C for the 70:30 films, under dc bias.

4.5. $e_{31,f}$ (Electric Field and Strain) in BST

Measurements were also taken as a function of static applied strain, through the fixed displacement of the piezoelectric actuator, comparable to piezoelectric systems designed by Dubois and Muralt.⁹ The circuit for the DC strain measurements is provided in Figure 4.8. The strain was calculated from these circuits using the following:

$$V_r = \frac{V_{out(strained)} - V_{out(unstrained)}}{V_{ex} * (Gain)}$$

$$x = \frac{=4V_r}{GF * (1 + 2V_r)}$$

where $V_{out(strained)}$ and $V_{out(unstrained)}$ are the voltage output of a strain gauge under the and prior to the application of strain. x is the calculated strain. V_{ex} is the excitation voltage used at the input of the Wheatstone bridge and Gain is the gain from the instrumentation amplifier used to increase the signal to noise ratio. GF stands for the gauge factor of the strain gauges, which for the Omega two dimensional gauges used in this study were $1.91 \pm 1.0\%$ and $1.95 \pm 1.0\%$ for the parallel and perpendicular gauges, respectively. Prior to static strain measurements the full Wheatstone bridge was balanced so that the unstrained gauge output was zero.

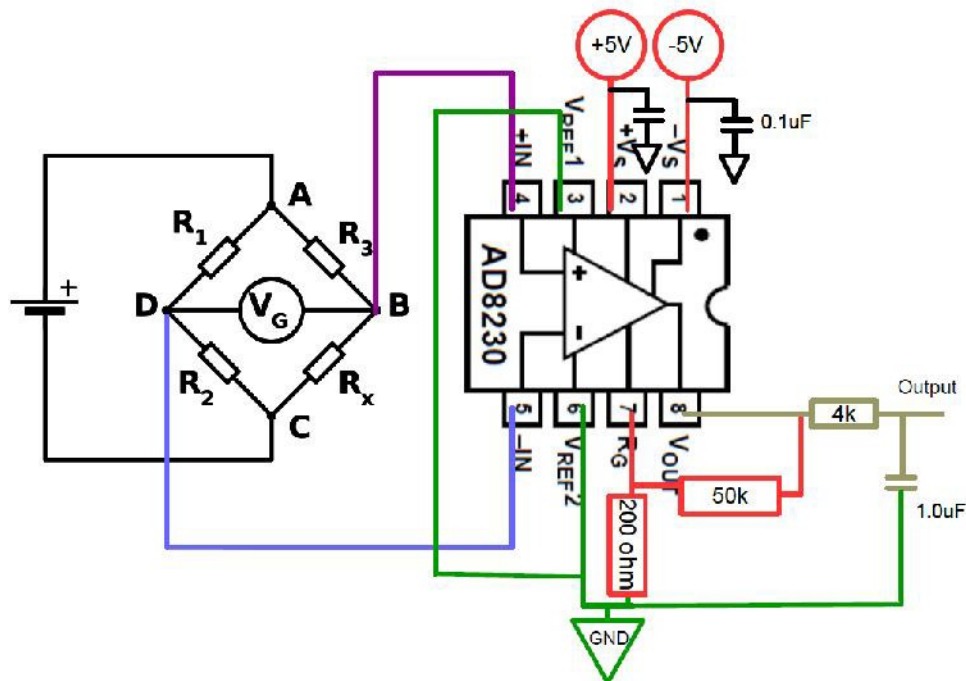


Figure 4.8. Schematic of the DC strain gauge measurement circuit

Although homogenous strain alone should not induce a piezoelectric response, strain has previously been shown to impact the dielectric response of BST.²³ To determine the impact of applied strain on the electric field induced piezoelectric response in BST concurrent applied strain and electric field piezoelectric measurements were taken. Figure 4.9 shows the results of concurrent applied strain and electric field in 70:30 BST thin films on Si. No significant change occurred in the piezoelectric response with applied strain of up to 100 $\mu\epsilon$. Continuing measurements to higher strains was inhibited by microcracking in the Si substrates. It can, however, be inferred from the enhancements in induced piezoelectricity and the doubling of the tunability of the 70:30 films on MgO over the same composition on silicon that the strain state of the sample played a large role in the electrical response.

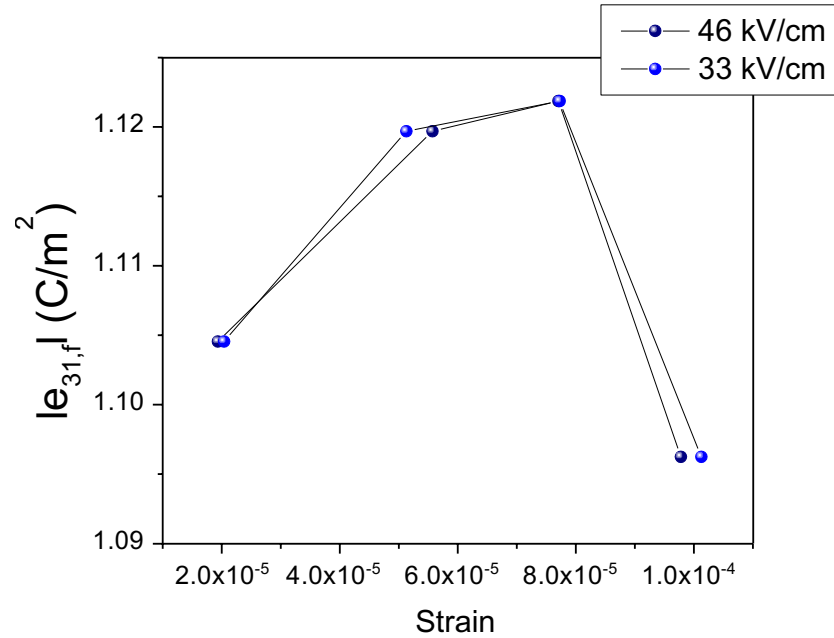


Figure 4.9. The impacts of strain on the electric field induced $e_{31,f}$ of BST 70:30 on Si measured for two different bias fields

4.6. Conclusions

In conclusion this work provides direct measurements of the tunability, dielectric non-linearity and induced electric field piezoelectricity for a series of BST. This information can be used to facilitate the development of predictive models for field induced piezoelectric impedance resonances. Additionally, the metrology for electric field induced and strain influenced $e_{31,f}$ piezoelectric characterization is discussed.

4.7. References

1. Tagantsev, A. K., Sherman, V. O., Astafiev, K. F., Venkatesh, J. & Setter, N. Ferroelectric materials for microwave tunable applications. *J. Electroceramics* **11**, 5–66 (2003).
2. York, R. A., “Tunable Dielectrics for RF Circuits”, Multifunctional adaptive microwave circuits and systems, M. Steer, W. D. Palmer (Editors), SciTech Publishing, (2009).
3. Noeth, A., Yamada, T., Tagantsev, A. K. & Setter, N. Electrical tuning of dc bias induced acoustic resonances in paraelectric thin films. *J. Appl. Phys.* **104**, 094102 (2008).
4. Morito, K., Iwazaki, Y., Suzuki, T. & Fujimoto, M. Electric field induced piezoelectric resonance in the micrometer to millimeter waveband in a thin film SrTiO₃ capacitor. *J. Appl. Phys.* vol. 94, no. 8, pp. 5199–5205, Oct. 2003.
5. Noeth, A., Yamada, T., Muralt, P., Tagantsev, A. K. & Setter, N., Tunable thin film bulk acoustic wave resonator based on Ba_xSr_{1-x}TiO₃ thin film, *IEEE Trans. Ultrason. Ferroelectr. Freq. Control*, vol. 57, no. 2, pp. 379–385, Feb. 2010.
6. Giere, A., Schafranek, R., Zheng, Y., Maune, H., Sazegar, M., Jakoby, R., Klein, A. Characterization of acoustic effects in ferroelectric thin-films for microwave components. *Frequenz* **62**, 52–56 (2008).
7. Vendik, I. B., Turalchuk, P. A., Vendik, O. G. & Berge, J. Modeling tunable bulk acoustic resonators based on induced piezoelectric effect in BaTiO₃ and Ba_{0.25}Sr_{0.75}TiO₃ films, *J. Appl. Phys.*, vol. 103, no. 1, p. 014107, Jan. 2008.
8. Jaffe, B., Cook, W. R. & Jaffe, H. L. *Piezoelectric ceramics*. (Academic Press, 1971).
9. Dubois, M.-A. & Muralt, P. Measurement of the effective transverse piezoelectric coefficient $e_{31,f}$ of AlN and Pb(Zr_xTi_{1-x})O₃ thin films,” *Sens. Actuators Phys.*, vol. 77, no. 2, pp. 106–112, Oct. 1999.

10. Viehland, D., Jang, S. J., Cross, L. E. & Wuttig, M. Deviation from Curie-Weiss behavior in relaxor ferroelectrics. *Phys. Rev. B* **46**, 8003–8006 (1992).
11. Tahan, D. M., Safari, A. & Klein, L. C. Preparation and characterization of $\text{Ba}_x\text{Sr}_{1-x}\text{TiO}_3$ thin films by a sol-gel technique. *J. Am. Ceram. Soc.* **79**, 1593–1598 (1996).
12. Li, H., Roytburd, A. L., Alpay, S. P., Tran, T. D., Salamanca-Riba, L., and Ramesh, R. Dependence of dielectric properties on internal stresses in epitaxial barium strontium titanate thin films. *Appl. Phys. Lett.* **78**, 2354–2356 (2001).
13. Ito, S., Funakubo, H., Koutsaroff, I. P., Zelner, M. & Cervin-Lawry, A. Effect of the thermal expansion matching on the dielectric tunability of (100)-one-axis-oriented $(\text{Ba}_{0.5}\text{Sr}_{0.5})\text{TiO}_3$ thin films. *Appl. Phys. Lett.* **90**, 142910–142910–3 (2007).
14. Tiggelman, M. P. J., Reimann, K., Van Rijs, F., Schmitz, J. & Huetting, R. J. E. On the trade-off between quality factor and tuning ratio in tunable high-frequency capacitors. *IEEE Trans. Electron Devices* **56**, 2128–2136 (2009).
15. Robert, G., Damjanovic, D. & Setter, N. Preisach modeling of ferroelectric pinched loops. *Appl. Phys. Lett.* **77**, 4413–4415 (2000).
16. Eichel, R.-A. Structural and dynamic properties of oxygen vacancies in perovskite oxides—analysis of defect chemistry by modern multi-frequency and pulsed EPR techniques. *Phys. Chem. Chem. Phys. PCCP* **13**, 368–384 (2011).
17. Taylor, D. V. & Damjanovic, D. Evidence of domain wall contribution to the dielectric permittivity in PZT thin films at sub-switching fields. *J. Appl. Phys.* **82**, 1973–1975 (1997).
18. Bassiri-Gharb, N., Fujii, I., Hong, E., Trolier-McKinstry, S., Taylor, D. V., Damjanovic, D., Domain wall contributions to the properties of piezoelectric thin films. *J. Electroceramics* **19**, 49–67 (2007).

19. Garten, L. M., Lam, P., Harris, D., Maria, J.-P. & Trolier-McKinstry, S. Residual ferroelectricity in barium strontium titanate thin film tunable dielectrics. *J. Appl. Phys.* **116**, 044104 (2014).
20. Bokov, A. A. & Ye, Z.-G. Recent progress in relaxor ferroelectrics with perovskite structure. *J. Mater. Sci.* **41**, 31–52 (2006).
21. Zalar, B., Laguta, V. V. & Blinc, R. NMR Evidence for the coexistence of order-disorder and displacive components in barium titanate. *Phys. Rev. Lett.* **90**, 037601 (2003).
22. Boikov, Y. A., Khamchane, K. & Claeson, T. Ferroelectric domain wall relaxation in $\text{Ba}_{0.25}\text{Sr}_{0.75}\text{TiO}_3$ films displaying Curie-Weiss behavior. *J. Appl. Phys.* **96**, 4392–4399 (2004).
23. Shaw, T. M., Suo, Z., Huang, M., Liniger, E., Laibowitz, R.B, Baniecki, J. D., The effect of stress on the dielectric properties of barium strontium titanate thin films. *Appl. Phys. Lett.* **75**, 2129–2131 (1999).

Chapter 5.

Residual Ferroelectricity

5.1 Introduction

This chapter covers the persistence of ferroelectricity in nominally paraelectric materials through the temperature dependence of the Rayleigh behavior. Relevant background literature is provided on previous observations of residual ferroelectricity and possible mechanisms which could induce a persistent ferroelectric response. After presenting the residual ferroelectric results, the final section covers the substantiation of the theory of ferroelectricity leading to the observed Rayleigh behavior.

5.2 Background

The balance between tunability and loss is often achieved in tunable dielectrics by poising the material in the paraelectric phase near the paraelectric-ferroelectric phase transition. This provides a high permittivity and field dependence of the dielectric constant, while domain wall contributions to the loss should be eliminated.^{1,2} Figure 5.1 shows a schematic of the dielectric and loss tangent response as a function of temperature through the paraelectric phase transition.

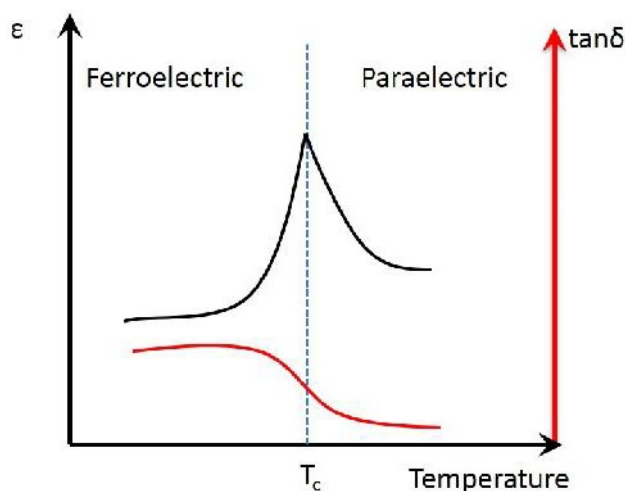


Figure 5.1. Schematic of the dielectric response as a function of temperature through the paraelectric to ferroelectric phase transition in barium strontium titanate

The displacement of domain walls with applied strain or electric fields produces a hysteretic, extrinsic contribution to the permittivity and dielectric loss by interactions with pinning centers in the material.^{3,4} Jin et al. observed an extrinsic contribution to the dielectric response of perovskite ferroelectric ceramics extending into the low gigahertz frequency range,⁵ producing both a strong dispersion and an increase in dielectric loss in the frequency range of interest for tunable devices. In addition to increasing the dielectric loss, in the ferroelectric phase, the material is also piezoelectric. When such a material is excited with an oscillating electric field, piezoelectric resonances can produce additional losses.⁶ As a result of these additional loss mechanisms, ferroelectricity is generally avoided in tunable dielectrics. Despite the criticality of reducing loss, the ferroelectric response of tunable dielectric materials is rarely fully characterized.⁶

The presence of residual ferroelectricity –a persistent ferroelectric response above the macroscopic phase transition temperature –in tunable dielectrics, can be inferred from hysteresis in the field dependence of the permittivity, piezoelectricity in the paraelectric phase, or excessive dielectric loss.^{6,7,8,9,10} Direct measurements of this phenomena would provide a better understanding of the prevalence, and origins (and thus routes to mitigation) of residual ferroelectricity. A precedence for residual ferroelectricity has been established in barium titanate, for which the existence of local polarization above the temperature of the displacive phase transition is well documented.^{11,12,13,14} It has been reported that coalescence of the titanium ion displacements along the $\langle 111 \rangle$ orientations leads to nanopolar-like regions, analogous to those found in relaxor ferroelectrics.^{8,11,12} Anomalous birefringence, associated with local symmetry breaking due to the titanium displacements, has been observed in bulk barium titanate single crystals to persist 50°C above the global phase transition temperature, though models of elastic coefficients predict the onset of nanopolar regions up to 75°C.^{13,15}

These local structural distortions are not unique to barium titanate, but have been identified in a range of materials which were considered to undergo exclusively displacive phase transitions to the ferroelectric state.¹³ In barium strontium titanate, symmetry forbidden first-order Raman scattering has been identified above the phase transition temperature.^{8,16,17} Forbidden scattering modes, accompanied by soft-mode overdamping, have been ascribed to the strong coupling of the nanopolar regions to the polar soft modes in relaxor ferroelectrics such as lead magnesium niobate.¹⁸ Kim et al. observed significant increases in the microwave dielectric loss in well crystallized samples correlated to the onset of local symmetry breaking in BST materials.¹⁷ However, the full temperature extent and impact to dielectric loss due of these order-disorder derived nanopolar regions in BST has not been established.

In addition to intrinsic mechanisms, barium strontium titanate materials have the added complication of many processing –or history –related sources for residual ferroelectricity in thin films and bulk ceramics. Among the possibilities are chemical inhomogeneity,^{19,20,21} self-polarization mechanisms due to injected or trapped charge,^{22,23,24} field-induced long range ordering of local polar regions,²⁵ local strain and local distortions due to doping, point defects or defect dipoles.^{8,17,26,27,28} Chemical inhomogeneity on the A-site would produce areas rich in barium with higher transition temperature than areas depleted of barium, leading to a diffuse phase transition. Using confocal scanning optical microscopy to probe the local ferroelectric response across the surface of chemical solution deposited BST thin films, Tikhomirov et al., observed 100°C variance in the local ferroelectric transition temperature.¹⁹ Additionally, substrate and processing induced strain has been shown to shift or broaden the transition temperature in BST.^{1,29} While uniform uniaxial strain, below the critical strain required to induce a phase transition, would not break the symmetry of the system, strains due to defects could lead to regions of local ferroelectric distortion. Local strains have been credited with the polar character along the grain boundaries of incipient ferroelectric strontium titanate ceramics and oxygen vacancies have been implicated in appearance of local polar response in STO and BST materials.^{22,26}

This work describes the prevalence and temperature extent of residual ferroelectricity in barium strontium titanate thin films as measured by Rayleigh analysis. Rayleigh analysis was used to monitor the presence of domain walls (or other mobile interfaces, including the boundaries of nanopolar regions) and the subsequent contribution to loss at temperatures above the global phase transition temperature. Measurement of the dielectric temperature dependence and polarization-electric field response are used to supplement and support the Rayleigh analysis and determine possible origins of the residual ferroelectricity.

5.3. Sample Preparation

In this section, BST films from two different sources are discussed. Sputtered $(\text{Ba}_{0.7}\text{Sr}_{0.3})\text{TiO}_3$ thin films on polycrystalline alumina substrates were provided from Dr. Maria's group. The sputtered films employed interdigitated top electrodes, IDE, due to the degradation which would occur to a platinum bottom electrode during the annealing of these films. The dielectric response of these films is presented in capacitance. This is due to the increase in uncertainty associated with the extraction of permittivity for these films from the Gevorgian IDE calculations (due to variations in IDE arm thickness, spacing, and sample thickness).

Additionally $(\text{Ba}_{0.8}\text{Sr}_{0.2})\text{TiO}_3$, $(\text{Ba}_{0.7}\text{Sr}_{0.3})\text{TiO}_3$, $(\text{Ba}_{0.6}\text{Sr}_{0.4})\text{TiO}_3$ thin films were deposited by chemical solution deposition, CSD, onto platinized MgO. These samples employed a metal-insulator-metal structures with platinum top electrodes.

5.4. Tunability

Figure 5.2 shows the characteristic tunability of the CSD BST thin films, taken at 25°C and 100 kHz. The relative tunability for the CSD $(\text{Ba}_{0.8}\text{Sr}_{0.2})\text{TiO}_3$, $(\text{Ba}_{0.7}\text{Sr}_{0.3})\text{TiO}_3$, $(\text{Ba}_{0.6}\text{Sr}_{0.4})\text{TiO}_3$, at 100 kHz, were characterized to fields over 250 kV/cm. The relative tunability and minimum quality factor for the CSD BST films at 100 kHz is shown in table 5.1. At 1kHz the relative tunability for the $(\text{Ba}_{0.8}\text{Sr}_{0.2})\text{TiO}_3$, $(\text{Ba}_{0.7}\text{Sr}_{0.3})\text{TiO}_3$ and $(\text{Ba}_{0.6}\text{Sr}_{0.4})\text{TiO}_3$ films are 90%, 86% and 72% and a dielectric loss of 0.0185, 0.005 and 0.002.

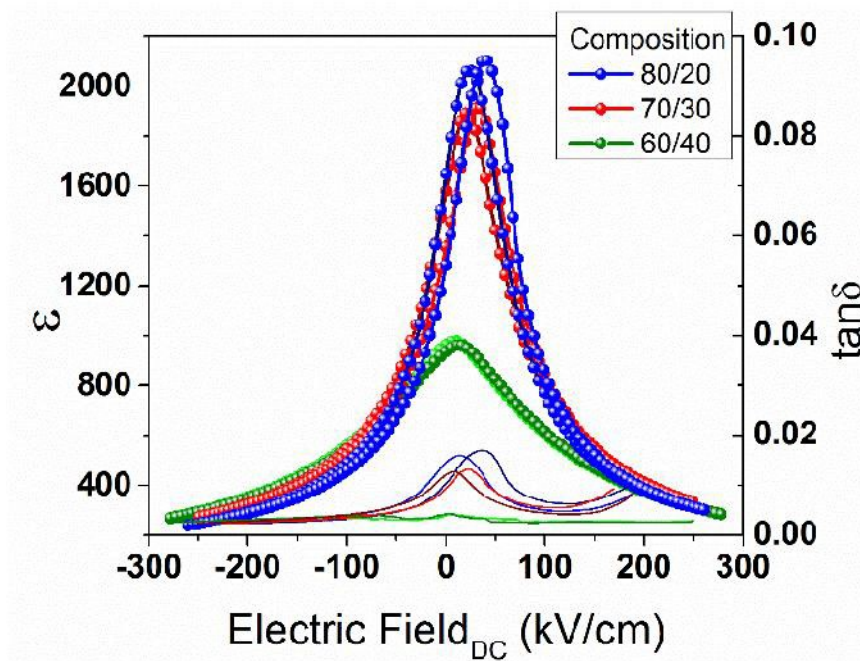


Figure 5.2. DC electric field dependence of the capacitance (symbols) and dielectric loss tangent (thin lines), for CSD $\text{Ba}_x\text{Sr}_{1-x}\text{TiO}_3$ thin films at room temperature and 100kHz.

Table 5.1. Relative tunability and minimum quality factor at maximum tunability calculated for the CSD $\text{Ba}_{1-x}\text{Sr}_x\text{TiO}_3$ thin films at 100kHz

Sample	Relative Tunability	Min. Quality Factor
$\text{Ba}_{0.8}\text{Sr}_{0.2}\text{TiO}_3$	89.0%	58.8
$\text{Ba}_{0.7}\text{Sr}_{0.3}\text{TiO}_3$	85.7%	76.9
$\text{Ba}_{0.6}\text{Sr}_{0.4}\text{TiO}_3$	72.5%	238

Slight hysteresis with applied voltage occurred in the dielectric response and loss, both in virgin and repeated measurements. This is indicative of the possibility of ferroelectricity, although charge trapping in the dielectric could, in principle, produce similar results. Dielectric hysteresis

at room temperature decreased with decreasing barium concentration, which is also consistent with the decrease in ferroelectric response that would be expected with the suppression of T_c .

Figure 5.3 shows the characteristic tunability of the sputtered $Ba_{0.7}Sr_{0.3}TiO_3$ thin films, with IDEs, taken at 25°C and 100 kHz. Again the tunability and dielectric loss tangent were slightly hysteretic with applied DC electric field. The relative tunability for the sputtered films was approximately 32%. The maximum in dielectric loss tangent was approximately 0.03. Compared to the CSD thin films, the relative tunability of the sputtered films was considerably lower and the dielectric loss was higher.

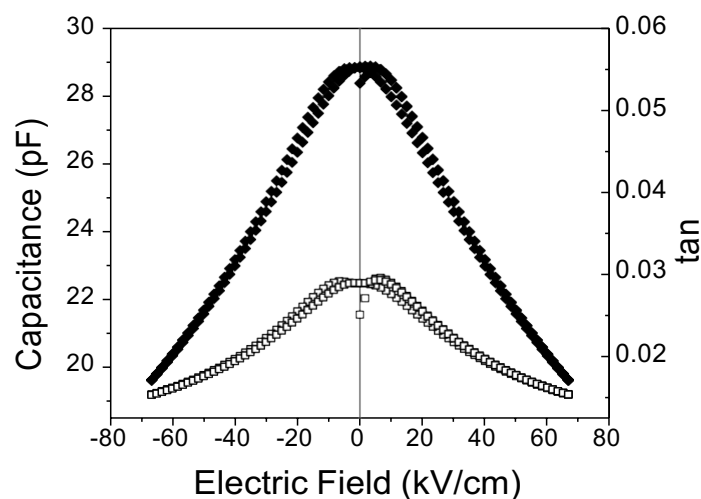


Figure 5.3. Tunability (filled symbols) and dielectric loss tangent (open symbols), for a sputtered $Ba_{0.7}Sr_{0.3}TiO_3$ thin film on alumina with interdigitated top electrodes, IDEs

5.5. Dielectric Temperature Dependence

Characterization of the temperature dependence of the dielectric response was used to determine the global phase transition temperature. Measurements were taken upon increasing and

decreasing temperature over a range of frequencies. Figure 5.4 shows the capacitance for the sputtered samples with a maximum near 15°C at 1 kHz, shifting to 38°C at 1MHz. The measured transition temperature and the breadth of the permittivity peak are comparable to values reported in the literature for thin films of BST with a 70/30 composition on similar substrates.^{1,29} For BST films processed on sapphire, 900 °C anneals will result in thermal expansion mismatch induced biaxial tensile strains on the order of 0.015, which are likely contributors to the elevated T_c values. The dielectric temperature response was broad, which could point to a distribution of transition temperatures, the influence of small grain size, or the effects of soft mode over-damping, which has previously been associated with the presence of nanopolar regions.^{8,20} The frequency dispersion of the maximum capacitance, coupled with the reduced dispersion above the permittivity maximum is characteristic of a relaxor-type ferroelectric. Relaxor characteristics are often associated with the existence of chemical nanoregions^{30,31} which would be consistent with the relaxor tendencies observed in BST thin films by Raman spectroscopy.⁸ No maximum in $\tan\delta$ was observed over the same temperature range.

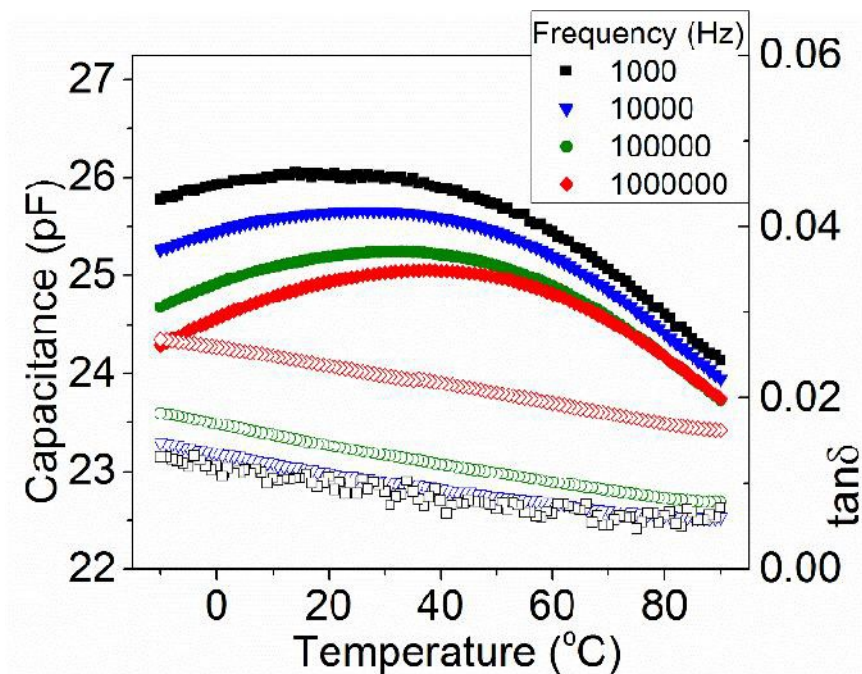


Figure 5.4. Capacitance (filled symbols) and dielectric loss tangent (open symbols) as a function of temperature from 1kHz to 1MH for a sputtered $\text{Ba}_{0.7}\text{Sr}_{0.3}\text{TiO}_3$ thin film. The maximum in capacitance with temperature at a given frequency is taken as the global phase transition temperature.

The dielectric temperature dependence and Rayleigh behavior for the CSD films were also characterized. Figure 5.5 presents the dielectric temperature response, at 100 kHz of the $\text{Ba}_{0.7}\text{Sr}_{0.3}\text{TiO}_3$ thin films deposited by chemical solution deposition. The temperature maximum of permittivity was determined as -22°C at 100 kHz, well below the expected phase transition for the bulk composition near room temperature. The dielectric temperature response showed a broad maximum which is, again, consistent with the gradual decay of the A-soft mode in BST films

determined by Raman spectroscopy.¹⁶ Similar to the sputtered films, frequency dispersion in the maximum permittivity was also observed for all compositions of CSD thin films.

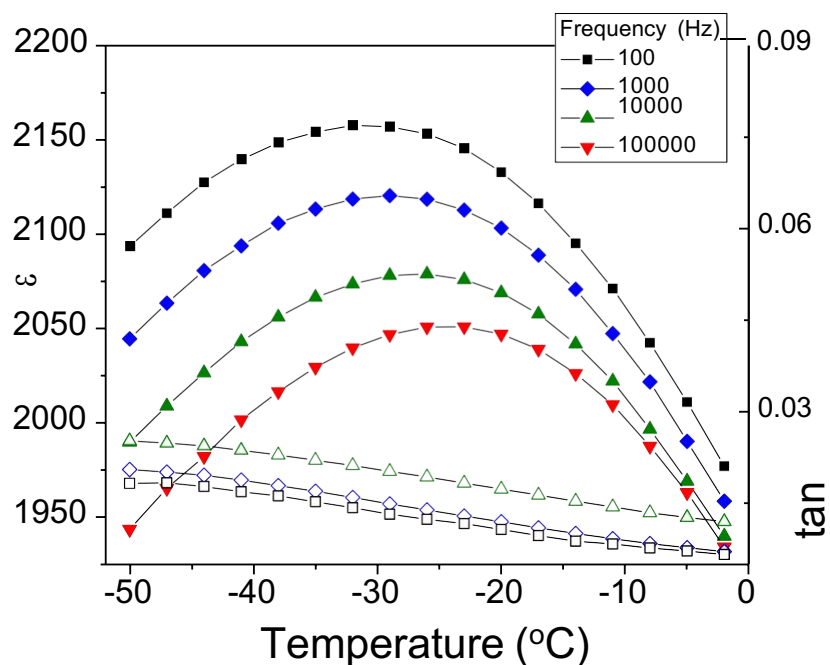


Figure 5.5. Permittivity (filled symbols) and dielectric loss tangent (open symbols) as a function of temperature from 100Hz to 1MHz for a CSD $\text{Ba}_{0.7}\text{Sr}_{0.3}\text{TiO}_3$ thin film with IDEs.

5.6. Temperature Dependence of Rayleigh Behavior

Figure 5.6-a presents characteristic measurements of capacitance as a function of the AC electric field for sputtered BST films, at 1MHz. Data were acquired from 90 to 10°C on cooling through the paraelectric to ferroelectric phase transition determined from the dielectric temperature dependence. The applied electric field was limited to 15 kV/cm. Both capacitance and loss tangent increased linearly with the applied AC electric field over this field range for all temperatures

measured. Rayleigh behavior continues over the entire temperature range measure, for a minimum of 50°C above the global phase transition temperature, indicating that mobile interfaces (e.g. domain walls or boundaries of nanopolar regions), and hence a residual ferroelectric response, persist over the same range.⁴ No discontinuities were observed in Rayleigh behavior upon going through the global phase transition temperature, as shown in figure 5.7; instead the Rayleigh parameters decreased linearly with temperature over the entire temperature range measured. Figure 5.6-b, shows the ac field dependence of the dielectric loss. For room temperature operation, the application of 10kV/cm AC electric field increased the dielectric loss over 100%.

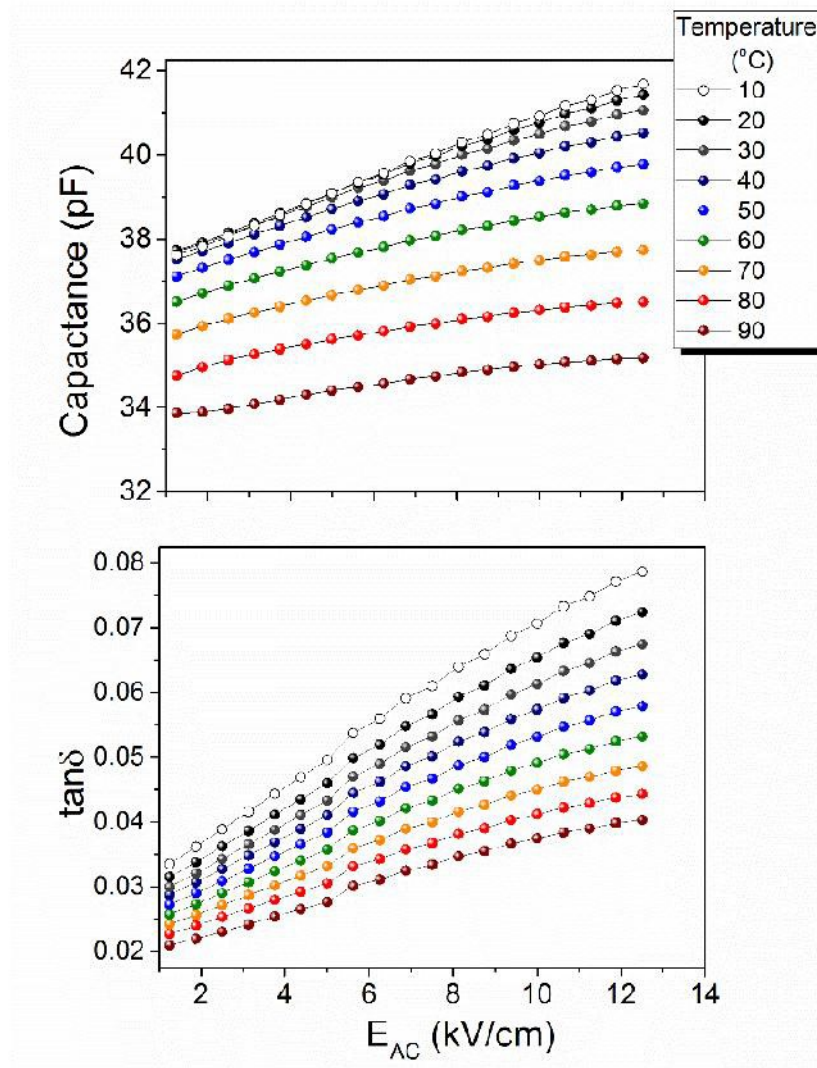


Figure 5.6. Characteristic capacitance (above) and dielectric loss tangent (below) small signal AC electric field response for a sputtered $\text{Ba}_{0.7}\text{Sr}_{0.3}\text{TiO}_3$ thin film measured through the temperature range of the global phase transition determined by the dielectric temperature response at a frequency of 1MHz (lines are added to guide the eye).

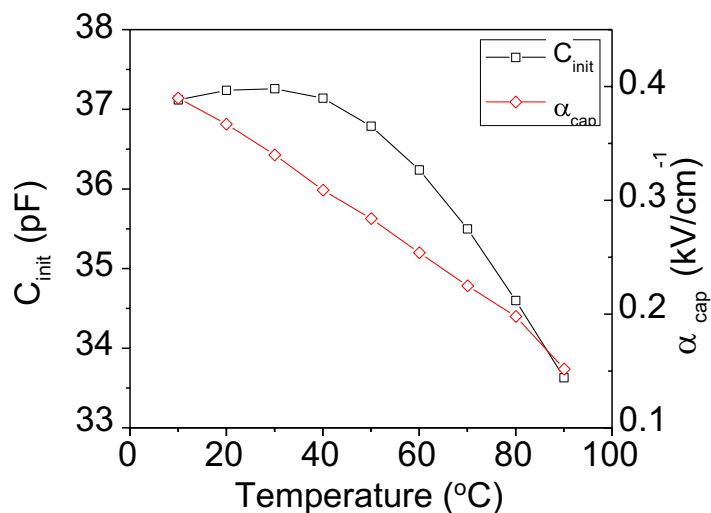


Figure 5.7. Rayleigh response for a sputtered BST thin film on alumina substrates as a function of temperature, $Ba_{0.7}Sr_{0.3}TiO_3$ thin film as a function of temperature. Here, since IDT electrodes were utilized, the Rayleigh behavior was assessed via $C = C_{init} + \alpha_{cap}$.

Rayleigh behavior as a function of temperature was also measured for the CSD BST thin films. First the polarization-electric field loops of these films were measured, as shown in Figure 5.10. The polarization-electric field loops of the CSD films were extremely narrow, making a determination of the coercive field (and thus the range of sub-switching voltages) difficult, so these measurements were made within with electric fields not exceeding 11 kV/cm.

Figure 5.8 shows the Rayleigh behavior, measured through the global phase transition temperature. The permittivity and loss were found to increase linearly with applied electric field up to 4 kV/cm and then displayed a shallow sub-linear region. Only the linear region was used for Rayleigh analysis.³² No discontinuities in Rayleigh behavior were observed at or near the

temperature of maximum permittivity, with the Rayleigh response decreasing with increasing temperature, until disappearing completely at 44°C for the measurement conditions employed.

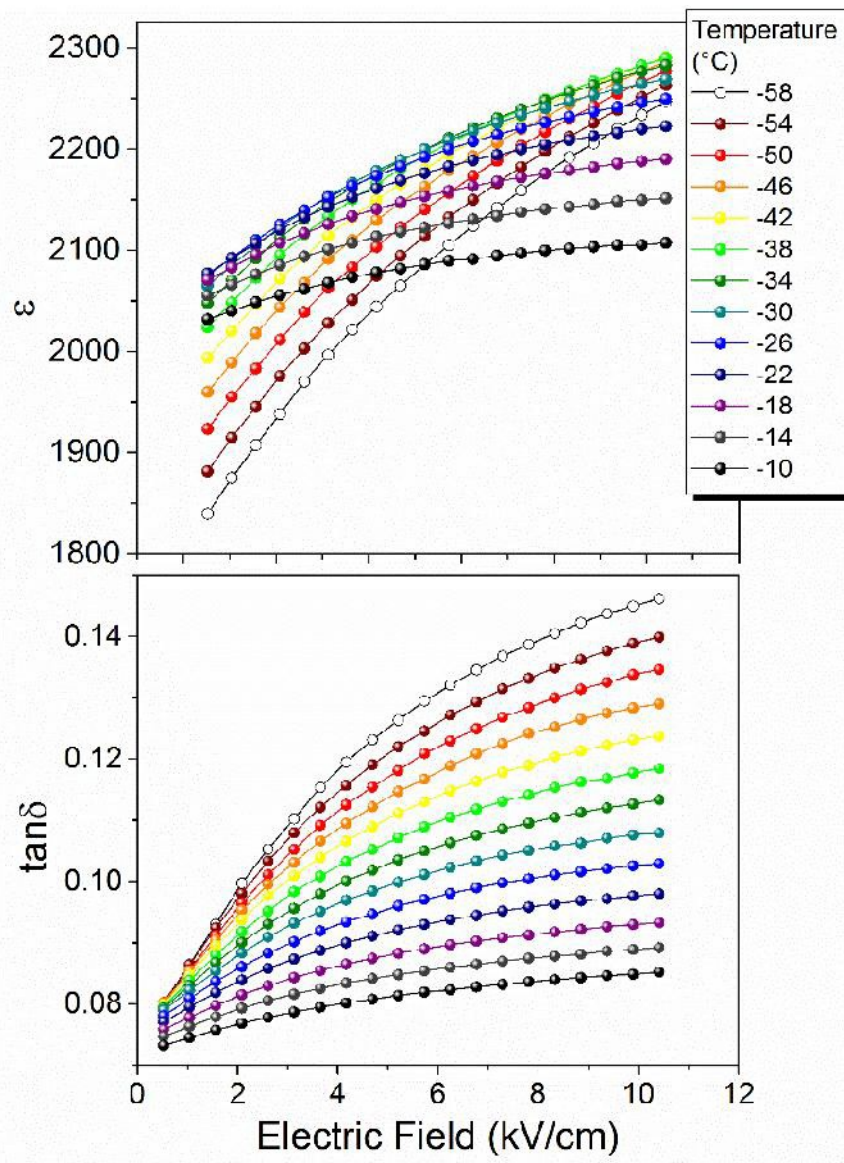


Figure 5.8. Characteristic permittivity (above) and dielectric loss (below) as a function of AC electric field response for a CSD $\text{Ba}_{0.7}\text{Sr}_{0.3}\text{TiO}_3$ thin film with a global phase transition temperature of -22°C at 100 kHz

Figure 5.9 shows the irreversible Rayleigh response, α , as a function of normalized global phase transition temperature for both CSD and sputtered samples. Temperatures are normalized to the temperature of maximum permittivity. Rayleigh behavior persists at least 50°C above the global phase transition temperature in the sputtered films; if the temperature dependence is extrapolated, Rayleigh behavior would be predicted to persist as much as 94°C above T_{\max} . In the CSD $\text{Ba}_{0.7}\text{Sr}_{0.3}\text{TiO}_3$ films, Rayleigh behavior persists 65°C above the global phase transition. Rayleigh behavior in the CSD films decreased exponentially with temperature, while the Rayleigh response of sputtered films decreased approximately linearly. For these two sample sets, the global strain states of the films were different due to the difference in CTE mismatch of the substrates, which could account for the difference in T_{\max} , but not for the disparity in the temperature dependence of the Rayleigh response. Difference in processing method could also lead to differences in chemical inhomogeneity or defect concentrations between these sample sets.

A finite irreversible response was observed above T_{\max} in all samples measured, even though the samples were made by different processing routes. This suggests that residual ferroelectricity above T_{\max} is comparatively common in barium strontium titanate based tunable dielectrics. Additionally, no discontinuities or significant differences were observed in initial permittivity upon subsequent electric field sweeps, as might have been expected if the response was due to the field-induced long range ordering of local polar regions. It is also important to note that the electric fields utilized in these measurements are considerably lower than those utilized during operation of tunable dielectrics. Thus, if field-induced ferroelectric ordering is responsible for the observation of Rayleigh-like behavior of the permittivity and loss, it is very likely to exist in many tunable microwave devices as well. There are previous reports that at high dc bias fields, electrostriction can contribute significantly to dielectric losses in tunable dielectrics.³³ Here,

however, no dc bias was utilized during the measurements, and the ac field was modest ($\sim 1 - 10$ kV/cm). One would also expect that contributions from electrostriction should appear in the second harmonic (rather than the first harmonic response that was measured here). Finally, since electrostriction is intrinsic, there should also be no dielectric loss associated with electrostriction, in contradiction to the experimental data. Thus, it is believed that electrostriction does not dominate the observed Rayleigh behavior.

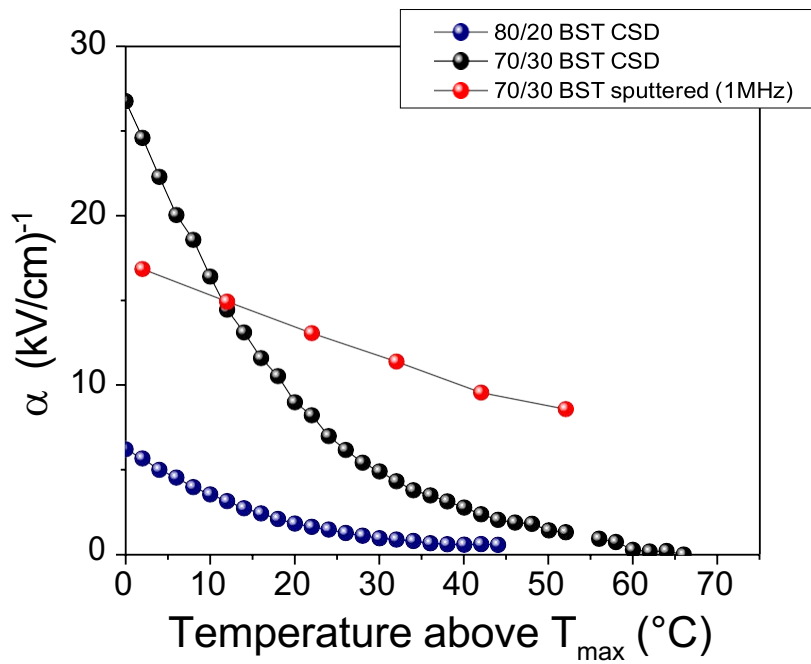


Figure 5.9. A comparison of the irreversible Rayleigh response as a function of normalized temperature for sputtered and CSD $Ba_xSr_{1-x}TiO_3$ thin films

5.7. Substantiation of Rayleigh Analysis

In order to further validate the Rayleigh data, minor polarization-electric, PE, field hysteresis traces were acquired for comparison for the sputtered BST thin films. In this work, polarization-electric field loops were taken to determine the coercive field of the thin films, to validate the Rayleigh analysis and to verify that the application of electric field during Rayleigh analysis did not induce a macroscopic ferroelectric phase.

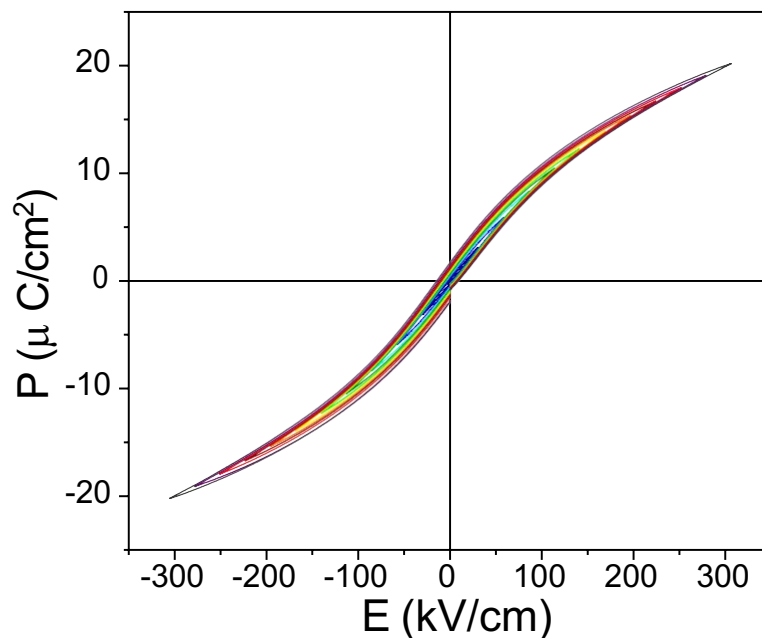


Figure 5.10. Polarization-electric field for the sputtered $\text{Ba}_{0.7}\text{Sr}_{0.3}\text{TiO}_3$ thin film taken on increasing voltage at room temperature and 100Hz. No discontinuities were observed before resistance degradation, indicating that the application of the AC electric field for Rayleigh analysis did not induce a phase change.

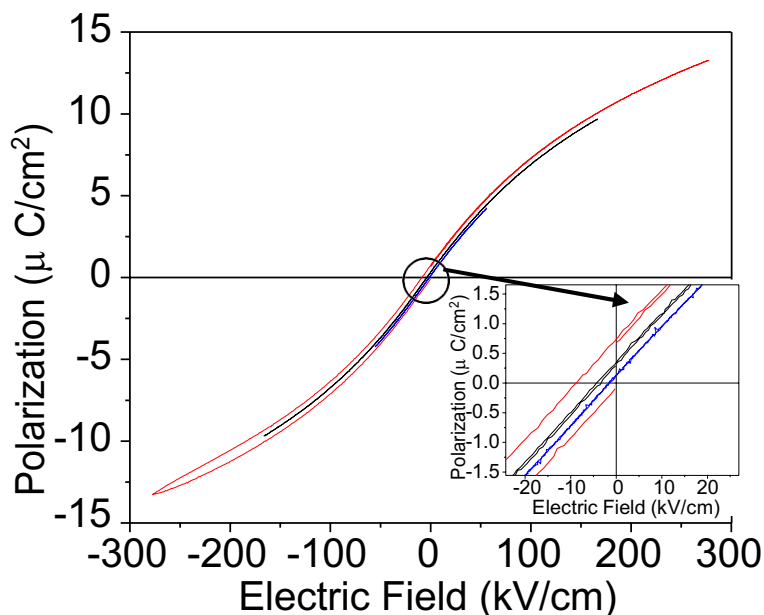


Figure 5.11. Polarization electric field loops for the CSD $\text{Ba}_{0.7}\text{Sr}_{0.3}\text{TiO}_3$ thin film taken at room temperature. **b.(inset)** Magnification showing the remanent polarization and the coercive electric field. P-E loops were extremely slim, indicating the materials were likely macroscopically paraelectric at room temperature.

Polarization-electric field loops for the CSD and sputtered films are shown in Figure 5.10 and 5.11. P-E loops were taken upon increasing the applied electric field and are an average of ten measurements per electric field step. The average coercive field and remanent polarization measured at the maximum field for the sputtered films were 15 kV/cm and $1.75 \mu\text{C}/\text{cm}^2$ respectively. Over this field range, there were no discontinuities in the polarization as would be observed for an electric field induced ferroelectric phase transition. This supports that assumption the measured Rayleigh response is due to the movement of preexisting domain walls or boundaries of nanopolar regions. Minor P-E hysteresis traces were also calculated from the Rayleigh data as follows:

$$P = (\varepsilon_{init} + \alpha E_{AC})E \pm \frac{\alpha}{2}(E_{AC}^2 - E^2).^{34}$$

The measured and calculated minor PE loops, taken at the same frequency, shown in Figure 5.12, are comparable with a slight over estimation of the Rayleigh derived P-E loop which is consistent with what has been reported on the Rayleigh analysis of PZT thin films.³⁴ Similarly, minor polarization-electric field loops for the CSD BST films were found to be without discernable hysteresis, supporting the conclusion that films are indeed in the paraelectric phase, and are consistent with the P-E loops modeled from Rayleigh data. Additionally, the sharp tips and narrow hysteresis of the measured minor loops indicates that the small signal leakage current, which for these samples was lower than or comparable to values reported previously for BST thin films.³⁵ The agreement of the Rayleigh results to the minor polarization-electric field loops supports the viability of Rayleigh analysis for residual ferroelectric measurements.

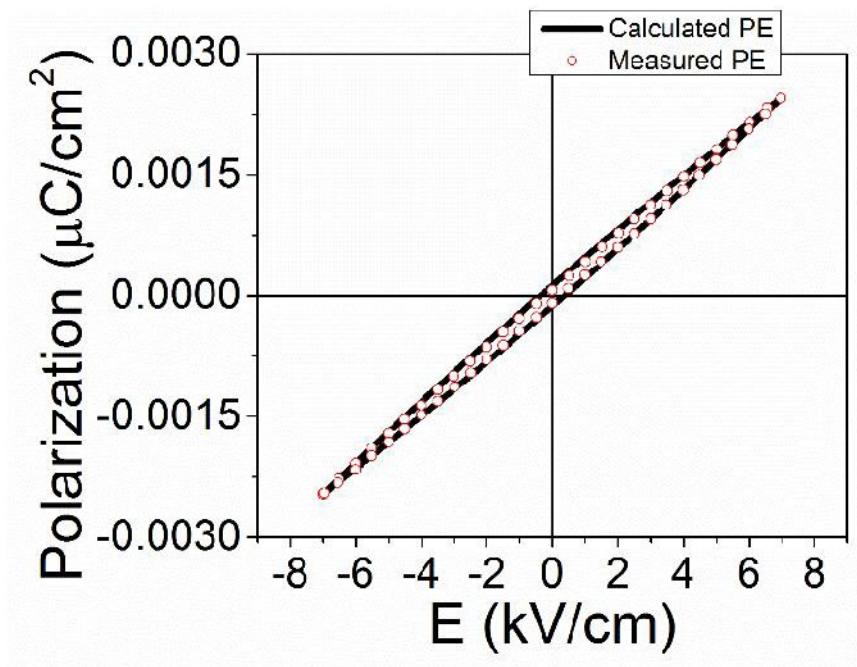


Figure 5.12. Minor polarization-electric field loop for a sputtered $\text{Ba}_{0.7}\text{Sr}_{0.3}\text{TiO}_3$ thin film taken at room temperature and 100 Hz. Calculated values from the Rayleigh response taken at the same frequency are compared to the measured minor loops

The frequency dependence of the Rayleigh responses was measured at room temperature, shown in Figure 5.13. A finite Rayleigh response persists into the megahertz and is expected to continue into the frequency regime of interest for tunable dielectric applications. The observed logarithmic frequency dependence of both the reversible and irreversible contributions are consistent with reports of Rayleigh response in other perovskite ferroelectric thin films.³⁴ While self-polarization mechanisms could emulate portions of the Rayleigh-like behavior, none are consistent with the frequency, AC electric field, and polarization-electric field response of the Rayleigh behavior observed in these materials.³⁶

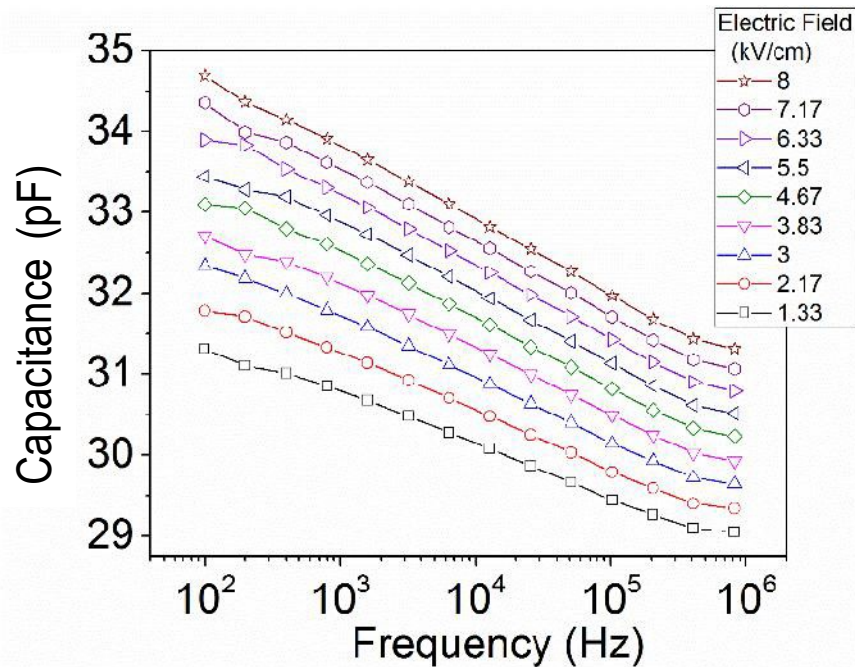


Figure 5.13. Frequency dependence of the capacitance as a function of applied small signal AC electric field for a sputtered $\text{Ba}_{0.7}\text{Sr}_{0.3}\text{TiO}_3$ thin film.

Leakage current as a function of electric field was also measured for the CSD and sputtered BST thin films, shown in Figure 5.14. Over the range of electric field used in the Rayleigh analysis the leakage current is well below 10^{-10} A (which corresponds to a leakage current density of less than 10^{-9} A/cm² for the samples with top and bottom electrodes). The leakage current results, which are in agreement with the sharp tips of the polarization electric field loops, in the range of applied electric field strengthens the conclusion that leakage current is not a significant contributor to the residual ferroelectric response.

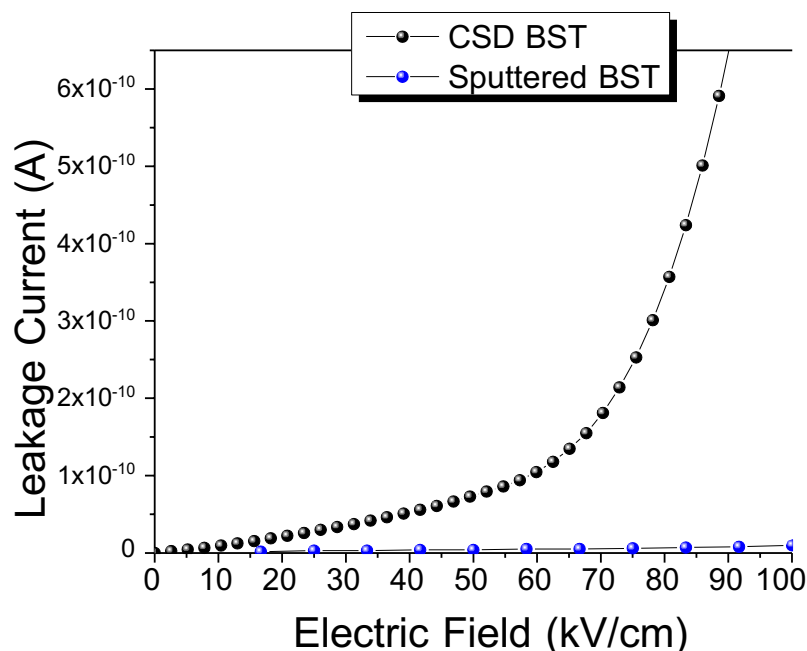


Figure 5.14. Leakage current for the CSD and sputtered BST thin films

In the next chapter the impact of chemical inhomogeneity on the presence of residual ferroelectricity and relaxor ferroelectric characteristics is discussed for barium strontium titanate thin films and ceramics. It is clear that residual ferroelectricity is observed in films prepared by completely different routes (and hence with different processing defects). The implications of the observed temperature extent of the measured Rayleigh response in the sputtered and CSD thin films is that complete removal of the ferroelectric contributions to loss would require the suppression of T_{\max} well below room temperature in addition to well-controlled processing. Ferroelectric measurements become more relevant as the ratio of barium to strontium pushes the phase transition temperature of the BST solid solution closer to room temperature. While processing defects, such as point defects, local strain or self-polarization mechanisms, do contribute to the dielectric loss of these materials, defects alone could not account for the observed frequency and temperature dependence of the residual ferroelectricity. It should be stressed that

the electric field range used in Rayleigh analysis are well below those the material will experience in operation, making ferroelectric measurements under operation conditions critical. Moreover, the prevalence of residual ferroelectricity highlights the importance of ferroelectric measurements in understanding and mitigating loss in tunable dielectrics. Additionally, the prevalence of residual ferroelectricity suggests that comparable measurements should be made in similar perovskite materials, especially those with coexistent order-disorder and displacive phase transition characteristics.

5.8. Conclusions

In conclusion, residual ferroelectricity in $(\text{Ba}_{1-x}\text{Sr}_x)\text{TiO}_3$ thin films was identified and characterized by Rayleigh analysis. Measurements of Rayleigh response as a function of temperature determined that residual ferroelectricity in the sputtered and CSD thin films persisted at least 50°C and 65°C respectively above the global transition temperature determined from the capacitive temperature response. Frequency dispersion in the dielectric temperature response points towards the presence of nanopolar regions as one source of residual ferroelectricity. The Rayleigh behavior was found to be consistent with the minor polarization-electric field loops.

5.9. References

1. Tagantsev, A. K., Sherman, V. O., Astafiev, K. F., Venkatesh, J. & Setter, N. Ferroelectric materials for microwave tunable applications. *J. Electroceramics* **11**, 5–66 (2003).

2. York, R.A. , “Tunable Dielectrics for RF Circuits”, Multifunctional Adaptive Microwave Circuits and Systems, M. Steer, W. D. Palmer (Editors), SciTech Publishing, (2009).
3. Damjanovic, D. Hysteresis in piezoelectric and ferroelectric materials. *The science of hysteresis*, 3, 337-465. (2006).
4. D. V. Taylor. Dielectric and Piezoelectric Properties of Sol-Gel Derived PZT Thin Films. **Ph.D. dissertation**, EPFL (1999).
5. Jin, L., Porokhonsky, V. & Damjanovic, D. Domain wall contributions in $\text{Pb}(\text{Zr},\text{Ti})\text{O}_3$ ceramics at morphotropic phase boundary: A study of dielectric dispersion. *Appl. Phys. Lett.* **96**, 242902–242902–3 (2010).
6. Gevorgian, S. S. & Kollberg, E. L. Do we really need ferroelectrics in paraelectric phase only in electrically controlled microwave devices? *IEEE Trans. Microw. Theory Tech.* **49**, 2117–2124 (2001).
7. Vendik, O. G., Hollmann, E. K., Kozyrev, A. B. & Prudan, A. M. Ferroelectric tuning of planar and bulk microwave devices. *J. Supercond.* **12**, 325–338 (1999).
8. A. Soukiassian D. A. Tenne. Raman study of $\text{Ba}_x\text{Sr}_{1-x}\text{TiO}_3$ films: Evidence for the existence of polar nanoregions. *Phys. Rev. B* **67**, 1, 012302 (2003).
9. Nath, R., Zhong, S., Alpay, S. P., Huey, B. D. & Cole, M. W. Enhanced piezoelectric response from barium strontium titanate multilayer films. *Appl. Phys. Lett.* **92**, 012916–3 (2008).
10. Fu, C., Yang, C., Domain configuration and dielectric properties of $\text{Ba}_{0.6}\text{Sr}_{0.4}\text{TiO}_3$ thin films. *Appl. Surf. Sci.* **252**, 461–465 (2005).
11. Zalar, B., Laguta, V. V. & Blinc, R. NMR Evidence for the coexistence of order-disorder and displacive components in barium titanate. *Phys. Rev. Lett.* **90**, 037601 (2003).

12. Blinc, R., *Advanced Ferroelectricity*. Oxford Science Publications, 151, (2011).
13. Bussmann-Holder, A., Beige, H. & Völkel, G. Precursor effects, broken local symmetry, and coexistence of order-disorder and displacive dynamics in perovskite ferroelectrics. *Phys. Rev. B* **79**, 184111 (2009).
14. Petkov, V., Gateshki, M., Niederberger, M. & Ren, Y. Atomic-Scale structure of nanocrystalline $\text{Ba}_x\text{Sr}_{1-x}\text{TiO}_3$ ($x = 1, 0.5, 0$) by x-ray diffraction and the atomic pair distribution function technique. *Chem. Mater.* **18**, 814–821 (2006).
15. Ko, J.-H., Kim, T. H., Roleder, K., Rytz, D. & Kojima, S. Precursor dynamics in the ferroelectric phase transition of barium titanate single crystals studied by Brillouin light scattering. *Phys. Rev. B* **84**, 094123 (2011).
17. Tenne, D. A. *et al.* Lattice dynamics in $\text{Ba}_x\text{Sr}_{1-x}\text{TiO}_3$ thin films studied by Raman spectroscopy. *J. Appl. Phys.* **96**, 6597–6605 (2004).
18. Tae-Gon Kim, J. O. Effect of crystallinity on the dielectric loss of sputter-deposited $(\text{Ba,Sr})\text{TiO}_3$ thin films in the microwave range. *J. Mater. Res.* **18**, 682 – 686 (2003).
18. Wakimoto, S., Stock, C., Birgeneau, R. J., Ye, Z.-G. Chen, W., Buyers, W. J. L., Gehring, P. M. and Shirane, G. Ferroelectric ordering in the relaxor $\text{Pb}(\text{Mg}_{1/3}\text{Nb}_{2/3})\text{O}_3$ as evidenced by low-temperature phonon anomalies. *Phys. Rev. B* **65**, 172105 (2002).
19. Tikhomirov, O., Jiang, H. & Levy, J. Direct observation of local ferroelectric phase transitions in $\text{Ba}_x\text{Sr}_{1-x}\text{TiO}_3$ thin films. *Appl. Phys. Lett.* **77**, 2048–2050 (2000).
20. Li, S., Eastman, J. A., Newnham, R. E. & Cross, L. E. Diffuse phase transition in ferroelectrics with mesoscopic heterogeneity: Mean-field theory. *Phys. Rev. B* **55**, 73831–12078 (1997).

21. Pervez, N. K., Hansen, P. J. & York, R. A. High tunability barium strontium titanate thin films for rf circuit applications. *Appl. Phys. Lett.* **85**, 4451–4453 (2004).
22. Chynoweth, A. G. Surface space-charge layers in barium titanate. *Phys. Rev.* **102**, 705–714 (1956).
23. Peng, C.-J. & Krupanidhi, S. B. Structures and electrical properties of barium strontium titanate thin films grown by multi-ion-beam reactive sputtering technique. *J. Mater. Res.* **10**, 708–726 (1995).
24. Pontes, F. M., Liete, E. R., Longo, E., Varela, J. A., and Eiras, J. A. Effects of the postannealing atmosphere on the dielectric properties of (Ba, Sr)TiO₃ capacitors: Evidence of an interfacial space charge layer. *Appl. Phys. Lett.* **76**, 2433–2435 (2000).
25. Lookman, A., McAeney, J., Bowman, R. M., Gregg, J. M., Kut, J., Rios, S., Ruediger, A., Dawber, M., Scott, J. F. Effects of poling, and implications for metastable phase behavior in barium strontium titanate thin film capacitors. *Appl. Phys. Lett.* **85**, 5010 (2004).
26. Pertsev, N. A., Tagantsev, A. K. & Setter, N. Phase transitions and strain-induced ferroelectricity in SrTiO₃ epitaxial thin films. *Phys. Rev. B* **61**, R825–R829 (2000).
27. Hyun, S. et al., Effects of strain on the dielectric properties of tunable dielectric SrTiO₃ thin films. *Appl. Phys. Lett.* **79**, (2001).
28. Herner, S. B., Selmi, F. A., Varadan, V. V. & Varadan, V. K. The effect of various dopants on the dielectric properties of barium strontium titanate. *Mater. Lett.* **15**, 317–324 (1993).
29. Ito, S., Funakubo, H., Koutsaroff, I. P., Zelner, M. and Cervin-Lawry, A. Effect of the thermal expansion matching on the dielectric tunability of (100)-one-axis-oriented (Ba_{0.5}Sr_{0.5})TiO₃ thin films. *Appl. Phys. Lett.* **90**, 142910–3 (2007).

30. Davies, P., and Akbas, M., Chemical order in PMN-related relaxors: structure, stability, modification, and impact on properties. *J. Phys. Chem. Solids* **61**, 159–166 (2000).
31. Randall, C. A., Barber, D. J., Groves, P., and Whatmore, R. W. TEM study of the disorder-order perovskite, $\text{Pb}(\text{In}_{1/2}\text{Nb}_{1/2})\text{O}_3$. *J. Mater. Sci.* **23**, 3678–3682 (1988).
32. Bassiri Gharb, N., Dielectric and Piezoelectric Nonlinearities in Oriented $\text{Pb}(\text{Yb}_{1/2}\text{Nb}_{1/2})\text{O}_3$ - PbTiO_3 Thin Films. Ph.D. dissertation, Dept. of Mat. Sci and Eng., Penn. State University, University Park, PA, 2005.
33. Tappe, S., Bottger, U., and Waser, R. Electrostrictive resonances in $(\text{Ba}_{0.7}\text{Sr}_{0.3})\text{TiO}_3$ thin films at microwave frequencies. *Appl. Phys. Lett.* **85**, 624–626 (2004).
34. Taylor, D. V., and Damjanovic, D. Evidence of domain wall contribution to the dielectric permittivity in PZT thin films at sub-switching fields. *J. Appl. Phys.* **82**, 1973–1975 (1997).
35. Zafar, S., Jones, R. E., Jiang, B., White, B., Kaushik, V., Gillespie, S. The electronic conduction mechanism in barium strontium titanate thin films. *Appl. Phys. Lett.* **73**, 3533–3535 (1998).
36. Afanas'ev, V. P., Pronin, I. P. & Kholkin, A. L. Formation and relaxation mechanisms of the self-polarization in thin ferroelectric films. *Phys. Solid State* **48**, 1214–1218 (2006).

Chapter 6

Further Evidence for Residual Ferroelectricity in BST

6.1. Introduction

Barium strontium titanate is the primary candidate for tunable dielectric applications but suffers decreased performance due to high dielectric loss.¹ Reducing this loss requires an understanding of the ferroelectric and dielectric factors leading to increased loss.

In the previous chapter, the presence of residual ferroelectricity in BST thin films was presented. This chapter expands upon these findings and presents data on the residual ferroelectric response for a series of thin films and ceramics. Nano-scale polar clusters, and nano-scale chemical inhomogeneity are characterized and discussed as underlying mechanisms contributing to the observed residual ferroelectric response.

Relaxor ferroelectricity has previously been suggested to occur in barium strontium titanate, as evidenced by disallowed first order phonon peaks in Raman spectroscopy.² Additionally, frequency dispersion which collapses above T_{\max} has previously been reported in 40:60 BST ceramics, as shown in Figure 6.1. Zhou et al. investigated the impact of the pre-calcination mixing time on the dielectric temperature response.³ It was noted that with decreasing mixing, and one would infer increasing chemical heterogeneity, frequency dispersion appeared in the dielectric response. It is possible that relaxor-like ferroelectric behavior is related to the residual ferroelectricity observed in this study.

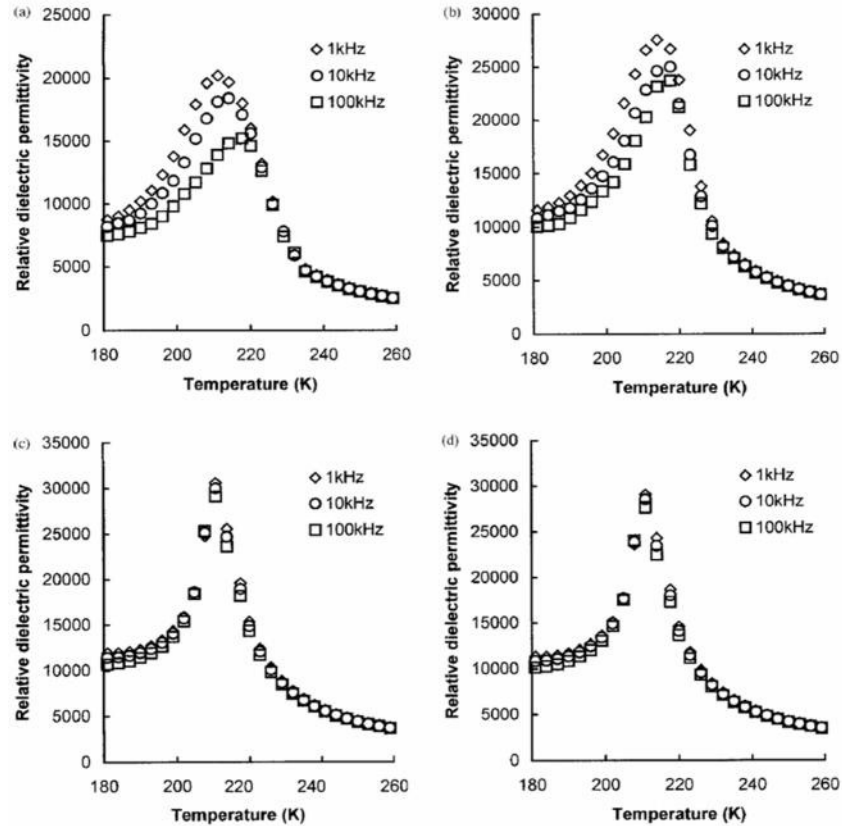


Figure 6.1. $\text{Ba}_{0.4}\text{Sr}_{0.6}\text{TiO}_3$ ceramics with different pre-calcination mixing times a.) 0 hours, b.) 3 hours, c.) 6 hours, and d.) 9 hours³. The amount of dielectric dispersion characteristic of relaxor ferroelectric characteristics is larger for shorter mixing times.

A series of experimental techniques, including second harmonic generation was employed here to determine the presence of nano-scale polar clusters in barium strontium titanate films and ceramics, and to investigate the impact of chemical inhomogeneity on the development of relaxor behavior in BST. The development of relaxor behavior is also discussed in the context of variations in chemical inhomogeneity as observed through electron energy loss spectroscopy.

6.2. Methods

Film deposition conditions and sample preparation for films produced by chemical solution deposited, CSD, and radio frequency-magnetron sputtered are discussed in chapter 3 and provided in reference ⁴. The sputter deposited BST thin films employed platinum interdigitated electrodes, while the CSD films had a metal-insulator-metal electrode structure with platinum top and bottom electrodes. The ceramic samples used in this investigation had approximate compositions of $\text{Ba}_{0.7}\text{Sr}_{0.3}\text{TiO}_3$ and $\text{Ba}_{0.67}\text{Sr}_{0.33}\text{TiO}_3$ and were fabricated by Texas Instruments using a wet chemical approach with strict tolerances on the level of chemical inhomogeneity.⁵

6.3 Results

6.3.1. Dielectric Temperature Response

Figure 6.2 provides the temperature dependence of the dielectric response of the $\text{Ba}_{0.8}\text{Sr}_{0.2}\text{TiO}_3$ (80:20) chemical solution deposited thin films. The maximum in the dielectric response was taken as the transition from the paraelectric to ferroelectric phase. The broad maximum observed in the CSD 80:20 BST thin films is characteristic of the response seen in all of the measured thin films. The frequency dispersion in the dielectric temperature response, along with the reduced dispersion above T_{max} is indicative of relaxor ferroelectric behavior.⁶ Data for sputtered and CSD films are shown in chapter 5.

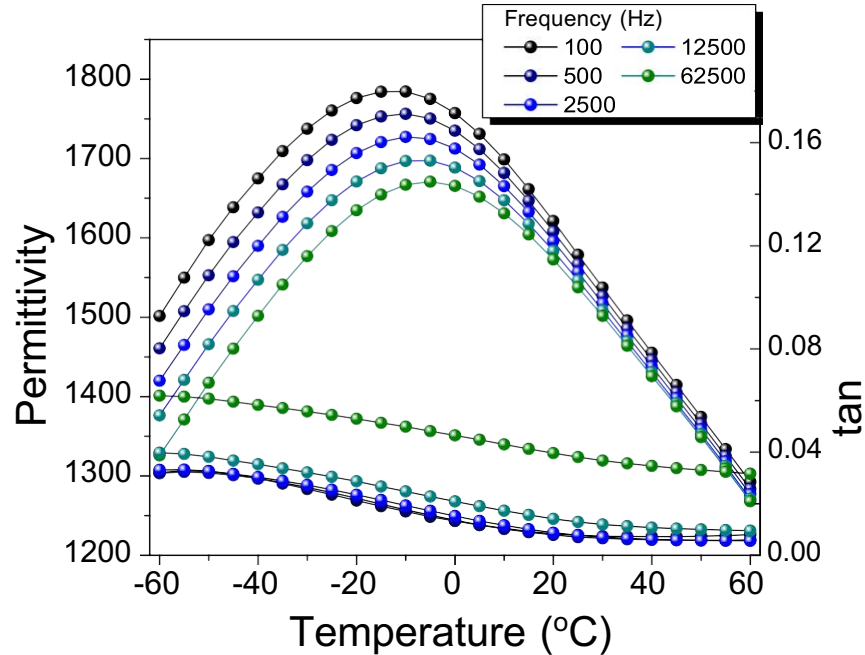


Figure 6.2. The dielectric temperature dependence of $\text{Ba}_{0.8}\text{Sr}_{0.2}\text{TiO}_3$ chemical solution deposited thin films on MgO showing a broad maximum and frequency dispersion

6.3.2. Rayleigh analysis

Figure 6.3 shows the irreversible Rayleigh response as a function of temperature for a series of BST materials. The temperature scale is normalized to the maximum in the dielectric response for each material, in order to compare the temperature extent of irreversible Rayleigh behavior. All measurements were taken at 100 kHz, with the exception of the sputtered BST thin films, which were taken at 1MHz (as the interdigitated electrodes had a smaller capacitance). Every material measured exhibits a finite irreversible Rayleigh response above T_{max} . This is indicative of the presence (and movement under AC fields) of domain walls, cluster boundaries or phase boundaries above the transition temperature, a residual ferroelectric response. Residual

ferroelectricity persists to at least $T_{\max} + 40^{\circ}\text{C}$ in all measured films. Similar results have been reported in lead magnesium niobate-lead titanate thin films where the irreversible Rayleigh response persisted over 70°C above the T_{\max} .⁷ Associated with the presence of residual ferroelectricity is an increase in the dielectric loss.

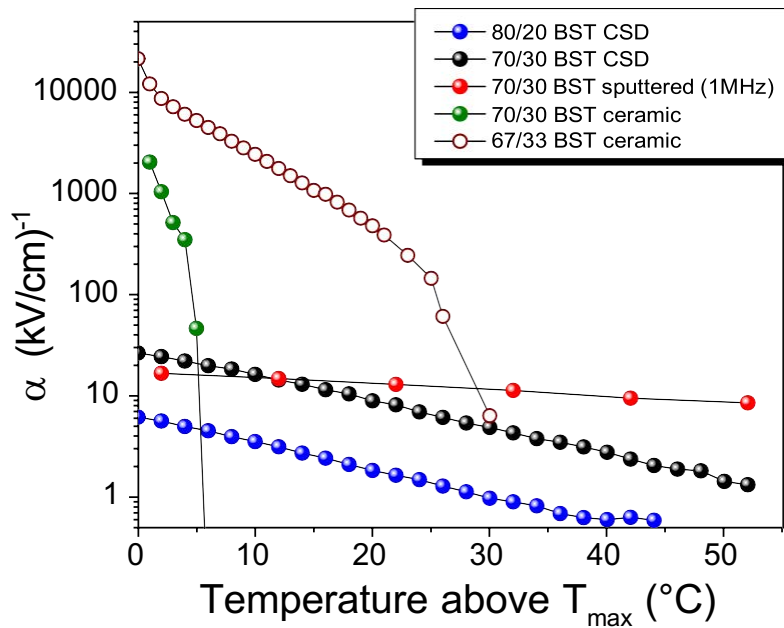


Figure 6.3. The irreversible Rayleigh response of various BST materials normalized to temperatures above the ferroelectric phase transition

Although all of the tested materials exhibit residual ferroelectricity, the temperature extent of the ferroelectric response varies greatly between materials processed in different manners. In the 70:30 BST ceramic samples (produced at TI) irreversibility becomes undetectable within 8°C above the transition temperature. In sputtered BST thin films of the same composition, a positive

α was measured at least 50 °C above T_{\max} ; a linear extrapolation suggests that it should persist to $T_{\max} + 90$ °C. The persistence of an irreversible Rayleigh response indicates mobile boundaries in BST. Coupled with the measurements of dielectric dispersion, it seems likely that polar cluster boundaries contribute at least part of the response. The drastic differences in the temperature extent of the irreversible Rayleigh behavior in these materials point towards additional factors which influence the development of the residual ferroelectricity. If these underlying mechanisms can be understood, it would provide routes to mitigate the high dielectric loss which plagues BST based tunable dielectrics.

6.3.3. Second Harmonic Generation

Second harmonic generation was used to investigate the presence of polar distortions above the transition temperature. The experimentation was conducted in the lab of Dr. Gopalan with the help of Arnab Sen Gupta and Ryan Haislmaier. As this method does not require the application of electric field, this can also be a check to insure that the Rayleigh behavior observed is not field induced. Figure 6.4 shows the SHG response of the 70:30 BST ceramic on heating and cooling through the transition temperature. The SHG response was normalized to the incident laser intensity. A first order transition occurs at approximately 35 °C, with little hysteresis in the transition temperature on heating or cooling. This is in agreement with the dielectric temperature response which shows a sharp transition at approximately 36 °C.

Figure 6.5 the decay of the SHG response above the transition temperature in the 70:30 BST ceramic samples plotted on a log scale. Hysteresis was observed in the magnitude of the SHG response above the transition temperature. The amount of hysteresis did not significantly

change with the ramp rates from 1-6 °C/min. At approximately 190 °C there is a change in the slope of the SHG response. It is possible that this indicates the Burns temperature, although other authors suggest that T_{Burns} is closer to 100 °C above T_{max} (e.g. $\sim 130^{\circ}\text{C}$ in this case).¹² There are no other likely structural or electrical transitions within this temperature regime. A second possibility is that the change in slope could be due to oxygen vacancies or vacancy cluster movement.¹³ Near 250 °C the hysteresis in the response on heating and cooling collapses. The SHG response continues to decrease in a linear fashion until hitting a noise floor at approximately 440 °C. A finite noise floor above that determined by the SHG equipment is expected in all measured samples due to the symmetry breaking at the grain boundaries.

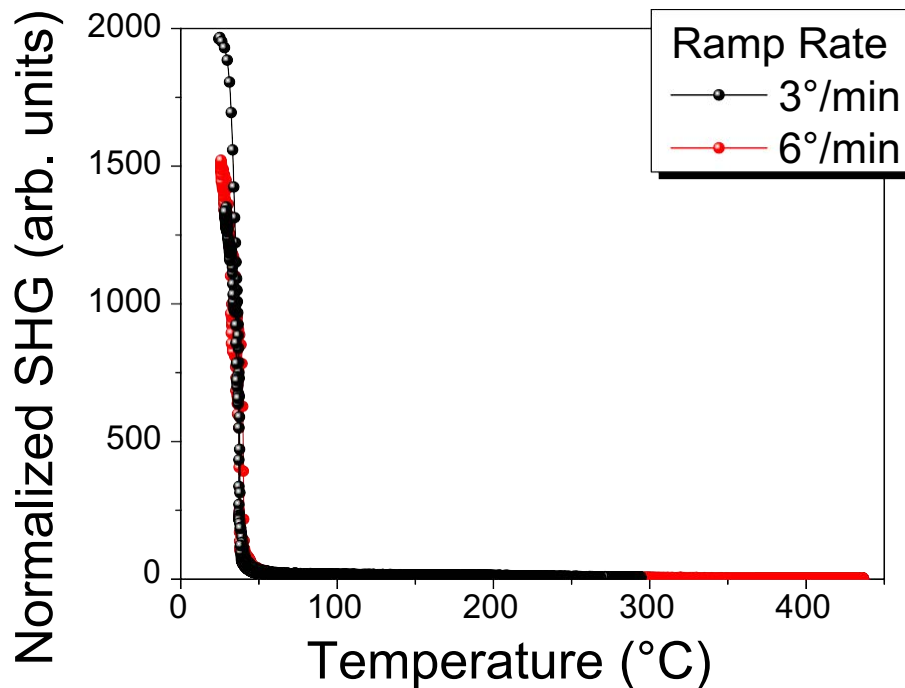


Figure 6.4. Normalized SHG response from the 70:30 BST ceramic samples taken at a ramp rate of 3 °C/min and 6 °C/min

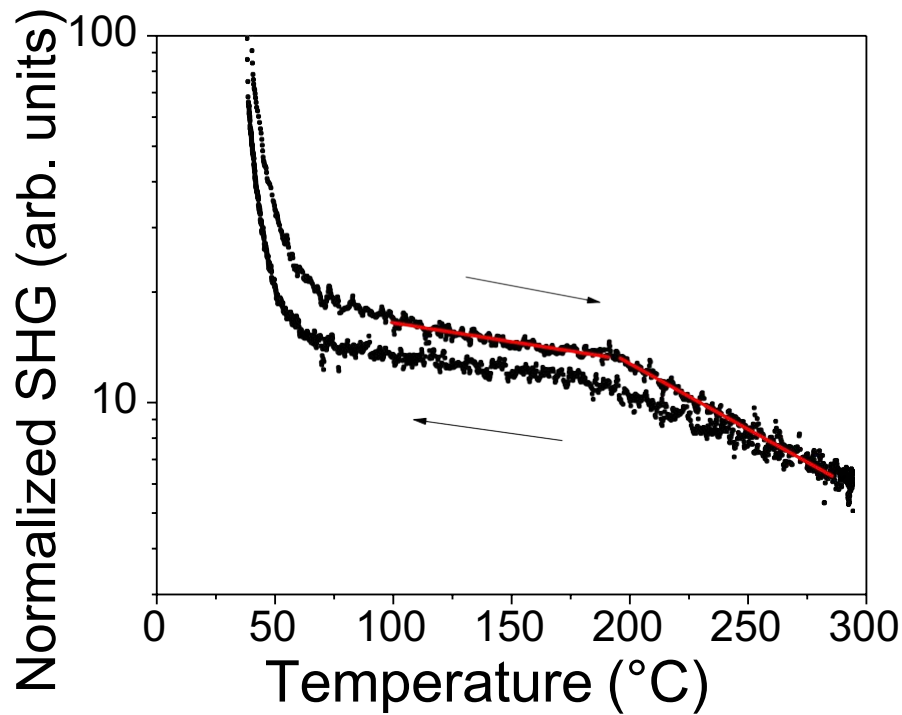


Figure 6.5. Normalized SHG response above the transition temperature in the 70:30 BST ceramic samples taken at a ramp rate of 3 °C/min measured first on heating then on cooling. The red lines are added as a guide to highlight the change in slope.

Figure 6.6 presents the SHG response of the CSD 70:30 BST thin film on MgO. Again the SHG response was normalized to the incident laser intensity. These measurements were taken on heating, followed immediately by cooling measurements and then another reheating run. The sample was held at each temperature for five minutes prior to taking an SHG measurement. A weak first order transition appeared between -40 and -20 °C, which is in agreement with the dielectric measurements (which showed a broad transition with a maximum at -22 °C). The decrease in SHG response occurred over a much larger temperature range than in the ceramic BST

samples. Minor hysteresis on temperature cycling was observed. The SHG response persisted over 45 °C above the transition temperature determined by the temperature dependence of the dielectric response, indicating the persistence of symmetry breaking features, such as polar clusters, within this temperature regime. The SHG response persisted until hitting a noise floor near 80 °C. Again, the effective noise floor in these measurements is likely to be due to the grain boundaries within the sample.

The SHG response for the sputtered 70:30 BST thin films on alumina are shown in Figure 6.7. A steady loss in SHG intensity extended throughout the entire temperature range measured, with a finite signature even at 250°C. No distinct features were observed near T_{\max} , at approximately 42 °C at 1 MHz, from the dielectric measurements near room temperature.

The SHG measurements support the Rayleigh measurements, in that a polar distortion exists above the global phase transition temperature. Additionally, as no electric field was applied during these measurements, it can be confirmed that residual ferroelectricity is not a result only of the application of the electric field.

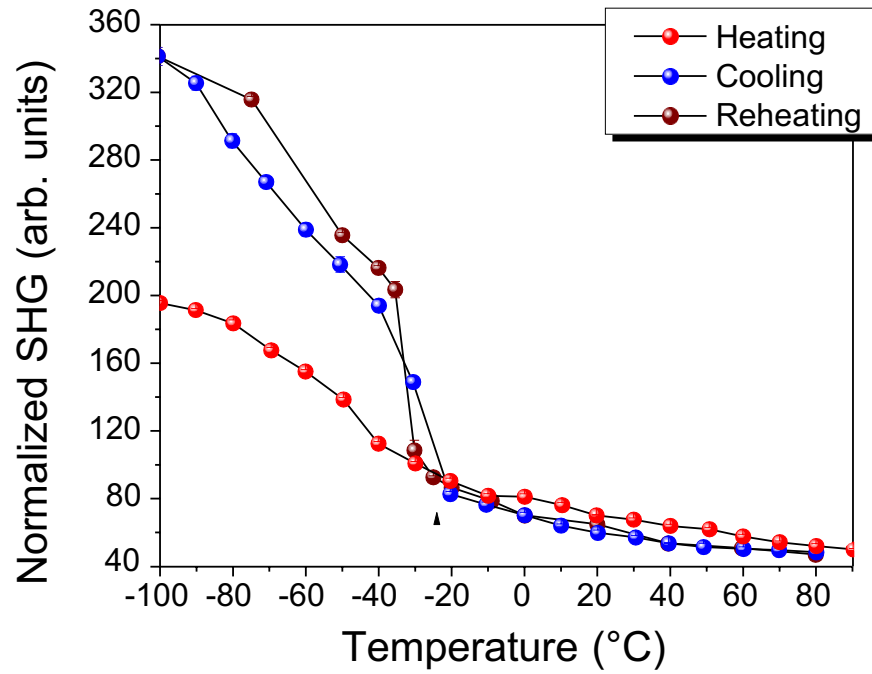


Figure 6.6. Normalized SHG response for the CSD 70:30 BST thin films, with the temperature of the maximum in the dielectric response indicated by the arrow for comparison.

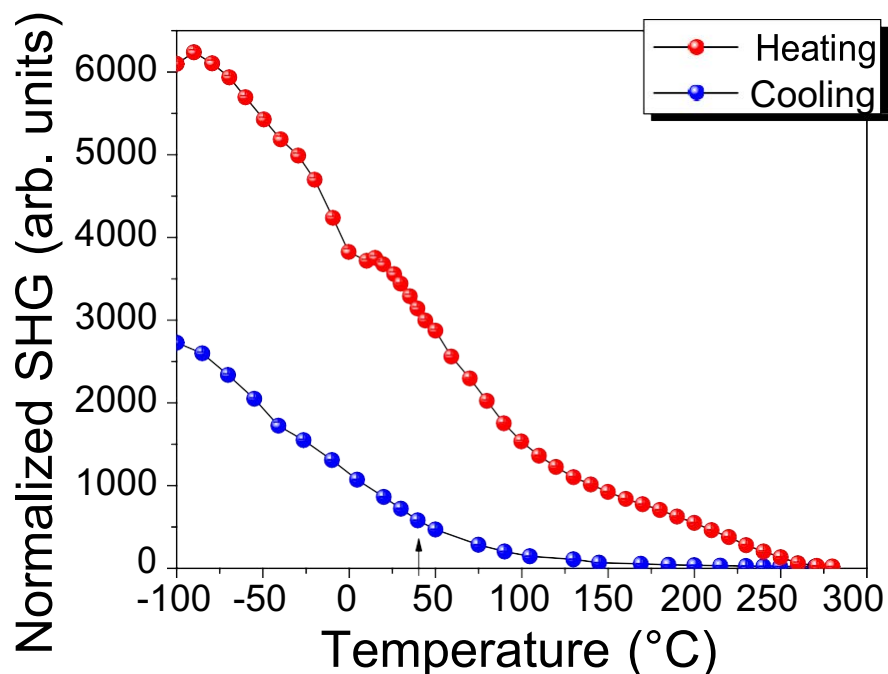


Figure 6.7. Normalized SHG response for the sputtered 70:30 BST thin films, with the temperature of the maximum in the dielectric response indicated by the arrow for comparison.

6.3.4. Transmission Electron Microscopy

Transmission electron microscopy was employed to investigate the nanoscale chemical inhomogeneity in the BST thin films and ceramics. Measurements were made at the North Carolina State University by the group of Prof. Elizabeth Dickey. The 70:30 BST ceramics from TI and the sputtered 70:30 BST thin films on alumina were studied. A probe-corrected FEI Titan G2 S/TEM operated at 200 kV was used to perform detailed electron energy loss spectroscopy (EELS) experiments. The Ba/Sr ratio was calculated assuming a 1:1 ratio of the A-site and B-site cations. Under this approximation, which does not account for the small reported solid solution regime,¹⁴

the Ba M_{4,5} and the Ti-L edges can be used for quantification. Any difference in intensity ratios then corresponds to a difference in Ba/Sr ratio.

Figure 6.8 presents the TEM and EEL results for the 70:30 BST ceramics near a dislocation. The calculated Ba/Ti ratio for the ceramic sample was 0.665 ± 0.014 based on 96 measurements. From this the average relative compositional variation across 37 nm was 2.1%. The standard deviation was within the estimated measurement error. Figure 6.9 shows the TEM and EELS maps for the sputtered 70:30 BST thin films. The average Ba/Ti ratio was 0.463 ± 0.028 . The average relative compositional variation was between 5.8-6% over 33 nm of the sputtered BST thin film. This shows that the A-site chemical inhomogeneity for the sputtered thin films is greater than that of the BST ceramics, which is consistent with the larger difference in the residual ferroelectric response observed in these materials.

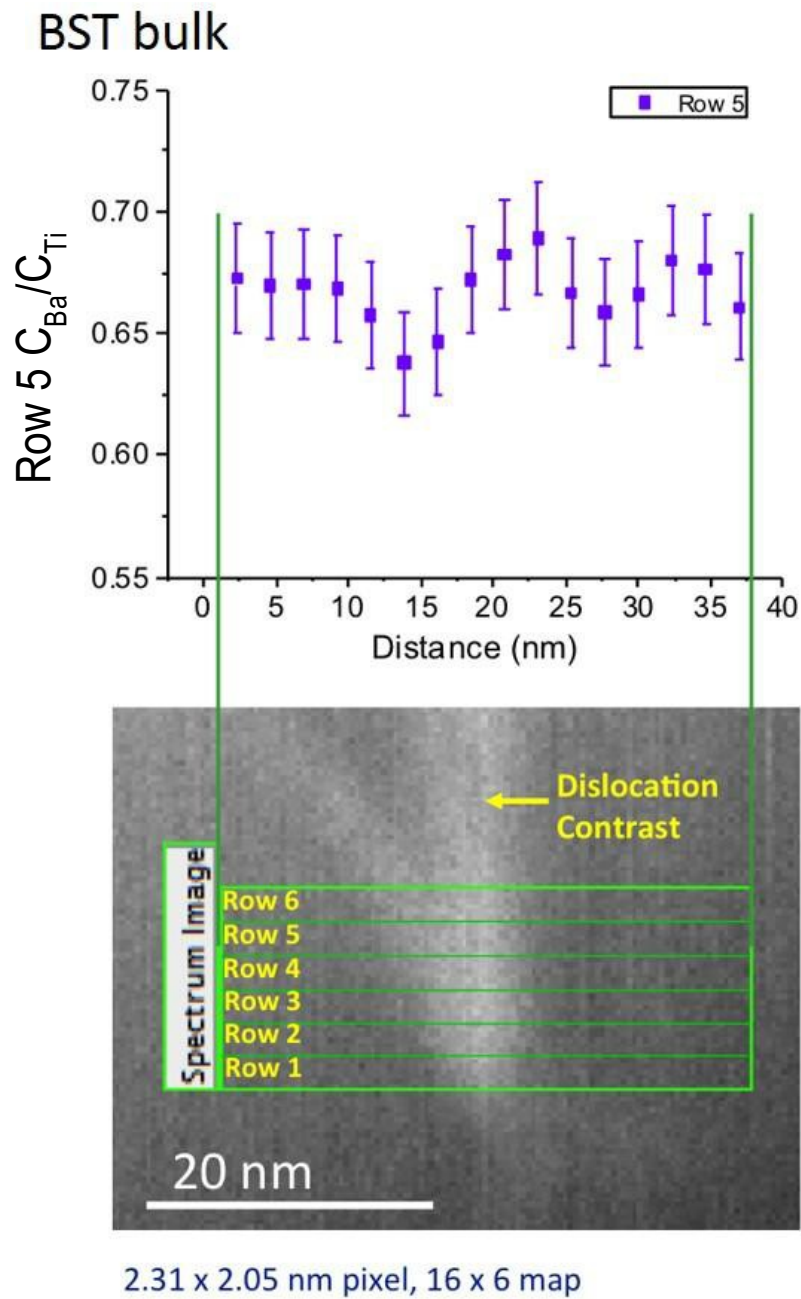


Figure 6.8. Transmission electron microscopy and electron energy loss spectroscopy of 70:30 BST ceramics

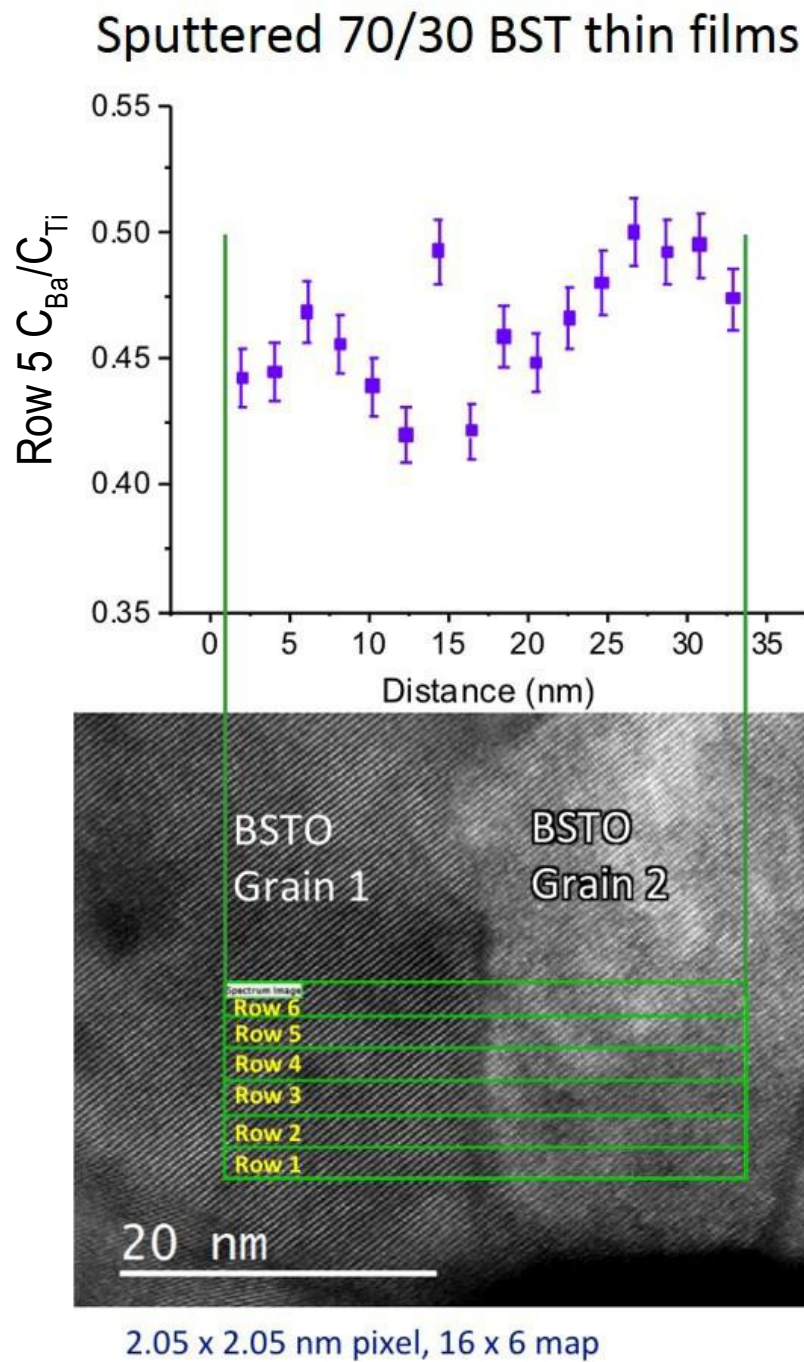


Figure 6.9. Transmission electron microscopy and electron energy loss spectroscopy of sputtered 70:30 BST thin films

6.4. Conclusion

In this chapter the residual ferroelectric behavior in barium strontium titanate thin films and ceramics was characterized through electrical, optical and physical methods. The existence of polar clusters was observed in the dielectric, Rayleigh and SHG response. The development of polar clusters was also found to be greater in samples with increased chemical inhomogeneity. The presence of polar clusters above the transition temperature corroborates the residual ferroelectric response measured in these materials. Variations in chemical inhomogeneity agree with the temperature extent of the residual ferroelectric response.

6.5. References

1. Tiggelman, M. P. J., Reimann, K., Van Rijs, F., Schmitz, J. & Hueting, R. J. E. On the trade-off between quality factor and tuning ratio in tunable high-frequency capacitors. *IEEE Trans. Electron Devices* **56**, 2128–2136 (2009).
2. A. Soukiassian D. A. Tenne. Raman study of $\text{Ba}_x\text{Sr}_{1-x}\text{TiO}_3$ films: Evidence for the existence of polar nanoregions. *Phys. Rev. B*, **67**, 012302 (2003).
3. Zhou, L., Vilarinho, P. M., Baptista, J. L., Dependence of the structural and dielectric properties of $\text{Ba}_{1-x}\text{Sr}_x\text{TiO}_3$ ceramic solid solutions on raw material processing. *J. Eur. Ceram. Soc.* **19**, 2015–2020 (1999).
4. Garten, L. M., Lam, P., Harris, D., Maria, J.-P. & Trolier-McKinstry, S. Residual ferroelectricity in barium strontium titanate thin film tunable dielectrics. *J. Appl. Phys.* **116**, 044104 (2014).

5. Ma, W. & Cross, L. E. Flexoelectric polarization of barium strontium titanate in the paraelectric state. *Appl. Phys. Lett.* **81**, 3440–3442 (2002).
6. Samara, G. A. The relaxational properties of compositionally disordered ABO_3 perovskites. *J. Phys. Condens. Matter* **15**, R367 (2003).
7. N. Bassiri Gharb. Dielectric and Piezoelectric Nonlinearities in Oriented $\text{Pb}(\text{Yb}_{1/2}\text{Nb}_{1/2})\text{O}_3$ - PbTiO_3 Thin Films. **Ph.D. dissertation**, Dept. of Mat. Sci and Eng., Penn. State University, University Park, PA, 2005.
8. Ko, J.-H., Kim, T. H., Roleder, K., Rytz, D. & Kojima, S. Precursor dynamics in the ferroelectric phase transition of barium titanate single crystals studied by Brillouin light scattering. *Phys. Rev. B* **84**, 094123 (2011).
13. Scott, J. F., Jiang, A., Redfern, S. A. T., Zhang, M. & Dawber, M. Infrared spectra and second-harmonic generation in barium strontium titanate and lead zirconate-titanate thin films: Polaron artifacts. *J. Appl. Phys.* **94**, 3333–3344 (2003).
10. Lee, S., Randall, C. A. & Liu, Z.-K. Modified phase diagram for the barium oxide–titanium dioxide system for the ferroelectric barium titanate. *J. Am. Ceram. Soc.* **90**, 2589–2594 (2007).

Chapter 7

The Flexoelectric Response in BST

7.1. Introduction

Interest in flexoelectricity has intensified after reports of flexoelectric coefficients exceeding $100 \mu\text{C}/\text{m}$ in barium strontium titanate (BST), which is six orders of magnitude higher than theoretically predicted.^{1,2,3} Flexoelectricity describes the development of polarization due to the application of a strain gradient, or conversely the development of a strain which increases linearly with an electric field gradient.^{2,4} Flexoelectric phenomenology predicts a linear relationship between the polarizability of the material and the polarization which develops due to an applied strain gradient. The constant of proportionality is known as the flexocoupling coefficient. Theoretical predictions of the flexocoupling coefficient extend from 1-10 Volts.^{5,6} Models of flexocoupling in perovskites suggest that anything exceeding 10-15 Volts will destabilize the perovskite structure, producing an incommensurate phase.² Despite this, flexocoupling coefficients of 850 Volts have been reported for BST.^{1,2} Thus, the anomalously large and varied flexocoupling coefficients in BST challenge a simple interpretation of the flexoelectric effect in paraelectric materials. An improved understanding of this heightened response would facilitate the development of novel flexoelectric-based sensors and energy harvesters.^{2,7,8}

Any local structural distortions, such as nanopolar regions, ferroelectricity, defects, or self-polarization could influence the measured flexoelectric response. Tagantsev has also suggested that surface piezoelectricity and flexoelectricity contribute to the overall flexoelectric response.⁹ Surface flexoelectricity, although unique to the particular surface chemistry, is predicted to be on

the order of $\sim 10^{-10}$ C/m.^{4,3} In a study on GaN based quantum dots, a fifty percent reduction in the modeled internal electric field occurred due to defect modulated flexoelectricity, for a flexoelectric response in the nC/m.. Additionally, self-polarization induced through localized space charge, asymmetric Schottky barriers and/or defect dipoles could contribute to flexoelectricity.^{10,11} Local strains associated with interfaces, grain boundaries, or defects have also been reported to produce polarization in the incipient ferroelectric SrTiO₃;^{12,13,14} for example, strain gradients on the order of 10^{-7} m⁻¹ reported in the vicinity of defects could produce localized polarizations of 1-10 $\mu\text{C}/\text{cm}^2$.¹⁵ Defects alone, however, still do not account for the reported flexoelectric constants observed in BST.¹⁵

Another potential source of enhanced flexoelectricity is ferroelectricity. It stands to reason that the measured flexoelectric polarization would be significantly increased by the large reorientable spontaneous polarization which develops in ferroelectrics. Recent reports in relaxor ferroelectric materials show a correlation between the onset of nano-polar regions and increased flexoelectric response.^{16,17} Narvaez and Catalan observed hysteresis in the flexoelectric response upon heating and cooling, associated changes in elasticity, and enhanced flexocoupling which persist up to the temperature where the nanopolar regions disappeared.¹⁶ It is notable that relaxor behavior has also been observed in Ba_{1-x}Sr_xTiO₃, as described in the previous chapter.

Furthermore, many perovskites which can become ferroelectric also display abnormally large flexocoupling coefficients. For example, the flexocoupling factors measured in the paraelectric phase are: BaTiO₃ $f \approx 560\text{V}$, PMN-PT $f \approx 110\text{-}270\text{V}$, Pb_{0.3}Sr_{0.7}TiO₃ $f \approx 170\text{V}$, Pb(Zr,Ti)O₃ $f \approx 72$).^{18,2,3,19} Many of these flexocoupling measurements were acquired within a few degrees of the paraelectric-ferroelectric phase transition, a region in which ferroelectricity likely

persists. In contrast, SrTiO₃, which does not become ferroelectric at any temperature, displays significantly smaller flexoelectric responses and flexocoupling factors. For example, in undoped, high purity SrTiO₃ the predicted transverse flexoelectric coefficients is ~ 2.3 nC/m and the measured response is 4 nC/m, which is well below the 100 μ C/m observed in BST.^{15,20} All of these results point to the importance of understanding the interactions between ferroelectricity and flexoelectricity.

Significant enhancements in flexocoupling have been observed in relaxor ferroelectrics like PMN-PT, BST, and Ba(Ti_{0.87},Sn_{0.13})O₃, close to T_{\max} .^{1,3,21} The accessibility of a high permittivity, low temperature ferroelectric to paraelectric phase transition in BST offers an opportunity to study flexoelectricity near T_C in order to provide answers to the disparity between the theoretical and measured flexoelectric response.

This work addresses several questions concerning the mechanisms of enhanced flexoelectric coupling in Ba_{1-x}Sr_xTiO₃. In particular, it is proposed that the flexoelectric coupling is enhanced by the existence of nano/micropolar regions above T_C in BST. A direct comparison is made between the residual ferroelectric contributions in the paraelectric phase, which are characterized by the irreversible Rayleigh behavior, and the temperature dependences of the flexoelectric response. Direct measurements of the flexoelectric poling are discussed and then compared to the strain gradient induced polarization and induced piezoelectric response.

7.2. Methods

The barium strontium titanate ceramics used in this analysis were developed at Texas Instruments using a wet chemistry route in order to maintain strict control over the A-site

stoichiometry.¹ These materials are from the same source as those utilized for studies of flexoelectricity in BST conducted by Ma and Cross.¹ Platinum sputtered top and bottom electrodes were used for all electrical measurements. Rayleigh analysis was conducted as a function of temperature and frequency using a precision LCR meter (Hewlett Packard 4284A) and a Delta design 2300 heating/cooling oven. The global paraelectric phase transition temperature was determined from the temperature dependence of the dielectric response measured at 100 kHz, using a HP4284A LCR meter. The sample temperature was monitored and recorded from a type-k thermocouple and a digital multimeter (Hewlett Packard 3478). Rayleigh measurements were taken at multiple frequencies and with applied electric fields less than 1/3 of the room temperature coercive electric field, in order to stay within the Rayleigh regime. The coercive electric field was determined from the average of ten consecutive polarization-electric field and strain-electric field measurements. Polarization-electric field loops were also taken as a function of applied strain gradient using ten consecutive initially positive sweeps followed by ten initially negative sweeps. Flexural stress-strain data were measured using an Instron 5866 in 4-point geometry.

Figure 7.1 shows the apparatus used for the flexoelectric measurements. Samples were sectioned into cantilevers with dimensions of 2cm x 7cm x 0.65mm, with 1.5cm x 5cm continuous sputtered platinum top and bottom electrodes. The electrode geometry insured that the measured polarization was above the noise-floor of the measurement system. However, since the strain gradient varies along the length of the cantilever, only an effective flexoelectric response was calculated.

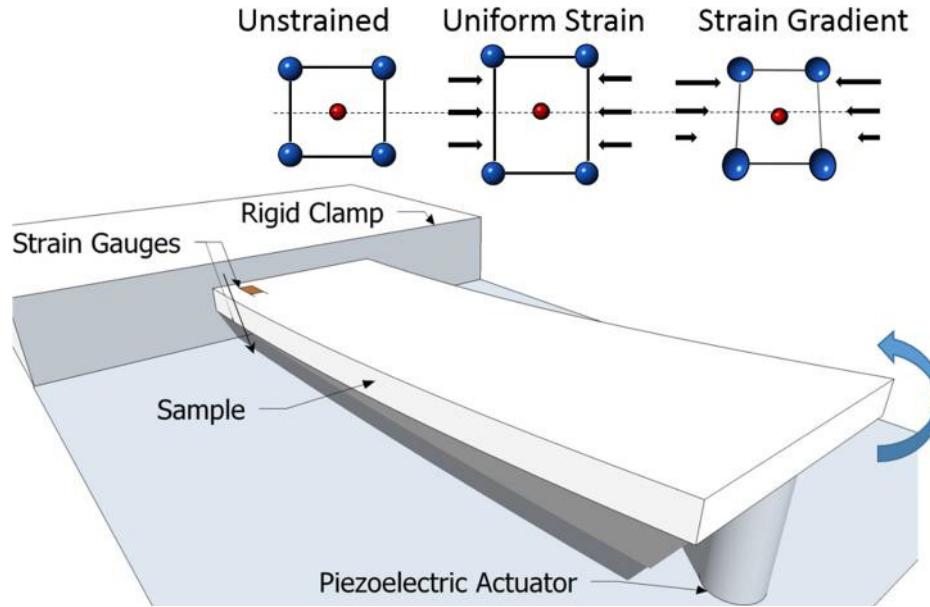


Figure 7.1. Schematic of the flexoelectric testing system and flexoelectric response

For the measurement system, lock-in amplifiers (Stanford Research SR830 DSP) were employed to simultaneously measure the charge output of the two orthogonal components of dynamic strain, while the static strain was measured by an amplified Wheatstone bridge. The strain gradient was measured via commercial strain gauges (Omega) attached to the top and bottom surfaces of the sample, parallel to the long axis of the cantilever as shown in Figure 1. The strain gradient was calculated from the output of the top and bottom gauge and the thickness of the sample as shown:

$$\nabla s = \frac{(s_t - s_b)}{t}$$

where t is the thickness and s_t , the strain at the upper surface, and s_b is the strain at the lower surface. The d_{33} piezoelectric measurements were taken on a Berlincourt meter (ZJ-2, Institute of

Acoustics Academia Sinica). This method was chosen in order to avoid the application of electric field, which could influence the domain state of the sample.

7.3. Results and Discussion

Rayleigh analysis can be used to characterize domain wall, polar cluster boundary and phase boundary movement in ferroelectrics.^{22,23,24} In this work, Rayleigh analysis was utilized to investigate residual ferroelectricity – the persistence of a (potentially local) ferroelectric phase in a globally paraelectric material. Rayleigh analysis of the reversible, ϵ_{init} , and irreversible, α , dielectric contributions as a function of temperature were made on increasing and decreasing temperature, near and above the paraelectric phase transition temperature, at 100kHz. The Rayleigh data were found to be in good agreement with the minor polarization-electric field loops, indicating that the origins of the Rayleigh response stem from the movement of domain, cluster, or phase boundaries through a random potential profile.^{25,26}

Figure 7.2 shows ϵ_{init} , αE , and total relative permittivity (total response = $\epsilon_{init} + \alpha E_{AC}$) as a function of temperature, normalized to the phase transition temperature. The presence of a finite irreversible contribution to the permittivity indicates the persistence of mobile boundaries over 30 °C above the phase transition temperature. These results are consistent with previous studies identifying the persistence of residual ferroelectricity in BST thin films 50°C above the global phase transition temperature.²⁷ These results were found to be in good agreement with the minor polarization-electric field loops, indicating that the origins of the Rayleigh response stem from the movement of domain, cluster, or phase boundaries through a random potential profile.^{25,26} In addition, the Rayleigh parameters dropped approximately linearly with the logarithm of

frequency, as has previously been reported for ferroelectric domain walls.^{25,28} The residual ferroelectricity also adds a contribution to dielectric loss under applied electric fields. For the AC electric fields used during Rayleigh analysis, less than 0.3 kV/cm, the dielectric loss increased by 38% at T_{\max} relative to the small signal value.

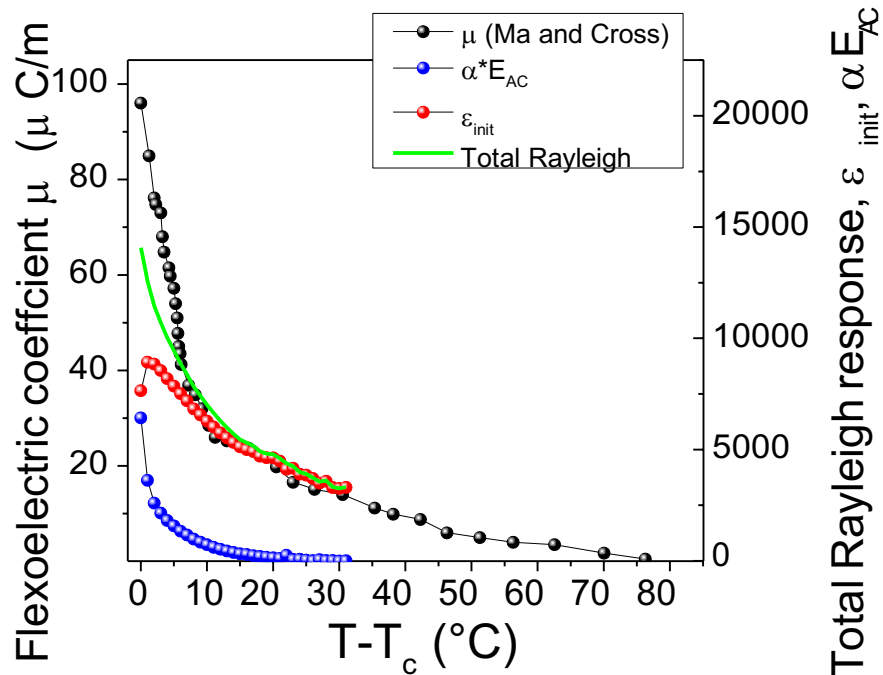


Figure 7.2. Temperature dependence of the Rayleigh response and flexoelectric coefficient (Ma and Cross), normalized to the ferroelectric-paraelectric phase transition temperature

It is important to note that the temperature extent of the observed residual ferroelectricity overlaps with the temperature range over which anomalously high flexoelectric coupling constants are reported.^{2,4} This both provide an extrinsic contribution to the polarization, and may also produce local strain gradients which add to the flexoelectric response.²

In principle, the presence of residual ferroelectricity may be correlated with local chemical inhomogeneity and/or local polar regions. Chemical inhomogeneity on the A-site has been detected in BST in other work,²⁹ and might be expected to affect the flexoelectric response through variations in local strain.⁹ However, it is important to note that flexoelectricity resulting from local strains associated with interfaces, grain boundaries, or defects^{12,13,14} would not produce the observed temperature or frequency dependence, or the irreversible Rayleigh behavior observed in this work.²⁵

Another possible source of residual ferroelectricity originates from the mixed order-disorder/displacive phase transition in BaTiO₃-based materials.^{30,31} Local symmetry breaking occurs above the displacive phase transition within the order-disorder regime, 50-75 °C above T_C.^{30,32,33,34} Forbidden Raman scattering modes and soft-mode overdamping in BST and been attributed to the strong coupling of the nanopolar regions to the polar soft modes.³⁵ Ma and Cross ascribe the large flexoelectric response in lead magnesium niobate to the reorientation of nanopolar regions. Recently the contribution from nanopolar regions to the flexoelectric response in lead magnesium niobate was confirmed in the work of Narvaez and Catalan.¹⁶ Comparable behavior in Ba_{1-x}Sr_xTiO₃ would account for both the Rayleigh behavior and the enhanced flexoelectric response.¹⁷ Given this, it seems probable that local polar regions associated with the order-disorder component of the phase transition in BST could also contribute to the flexoelectric response above T_C.

A comparison of the temperature dependence of the Rayleigh response and the flexoelectric response from reference 1 is shown in Figure 2. It is apparent that the anomalous increase in the flexoelectric response upon cooling towards the transition temperature is consistent

with the onset of residual ferroelectricity. This confirms the speculation from Ma and Cross concerning the presence of a residual ferroelectric phase (due to the deviations from Curie-Weiss behavior and increased loss upon approaching the transition temperature from above).¹ Not only is the observed flexoelectric response orders of magnitude higher than predicted, upon cooling towards T_c , the flexocoupling response increases, given that the flexoelectric coefficient rises faster than the permittivity.

Polarization-electric field (P-E) hysteresis measurements were made at room temperature under applied strain gradients in order to directly investigate the impact of strain gradients on the ferroelectric domains. It should be stressed that uniform applied strains do not allow for poling. Strain gradients, however, do break symmetry, allowing for the alignment of polar structures, including local polar regions. Figure 7.3 shows the average positive and negative coercive electric field, calculated from ten consecutive polarization-electric field loops measured at various strain gradients. The unstrained material exhibits negligible imprint. Furthermore, a separate test of unstrained samples cycled through tens of consecutive P-E field loops produced no imprint or discernable charge injection using the same measurement conditions. Thus, the measured difference in coercive fields when a strain gradient was applied corresponds to flexoelectric poling. No discontinuities associated with structural changes or physical damage were detected in the P-E response under strain gradients. Additionally, no pinching (as might be due to randomly oriented defect dipoles) was seen in any P-E sweeps.³⁶ Significant imprinting occurs even at modest strain gradients. Increasing the strain gradient beyond 1.3m^{-1} produced an imprint of 9.2 kV/m . The imprinting of the polarization-electric field loop towards the bottom electrode is consistent with the direction of applied strain gradient.

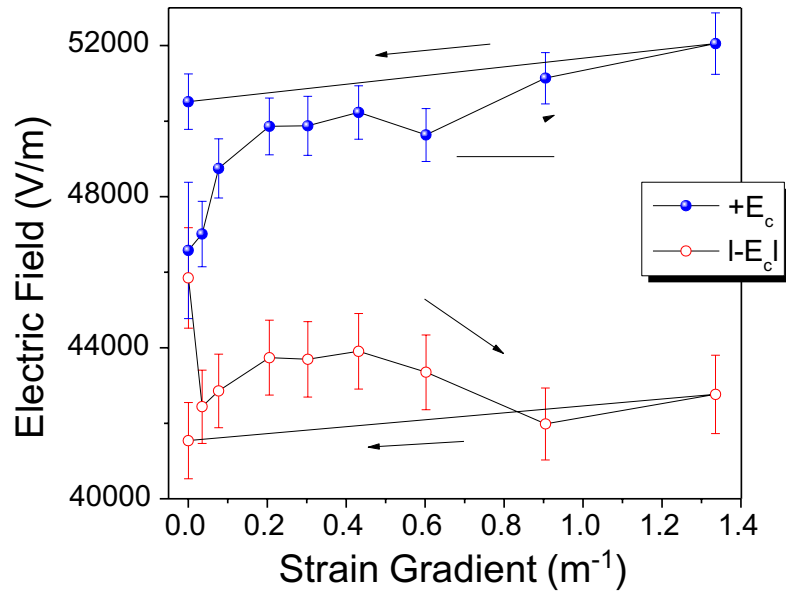


Figure 7.3. Impact of applied strain gradient on the coercive field of a flexoelectric sample showing flexo-poling and residual imprint upon removal of the electric field.

Upon the removal of the strain gradient, a residual imprint of approximately 9.0 kV/m is maintained. This persistent bias did not decay over a period of hours. It is hypothesized that this might be due to the strain-gradient-induced alignment of defect dipoles that could not be reoriented using electric field cycling alone. These results suggest that flexo-poling would be a viable option for materials too leaky to withstand electric poling. Furthermore, they also confirm that flexoelectric measurements in a material with some ferroelectric contribution (presumably either long or short range ordered) will be enhanced by the response of the pre-existing polarization. The observations of reorientation of polar structures under applied strain gradient is consistent with previous observations.^{37,38}

Changes in the piezoelectric response in lead zirconate titanate and BaTiO_3 thin films measured via piezoresponse force microscopy have also been attributed to flexoelectric poling.^{39,40} Flexoelectric poling was also observed in ferroelectric lead zirconate titanate ceramics, as shown in Figure 7.4 as a change in slope.¹⁹

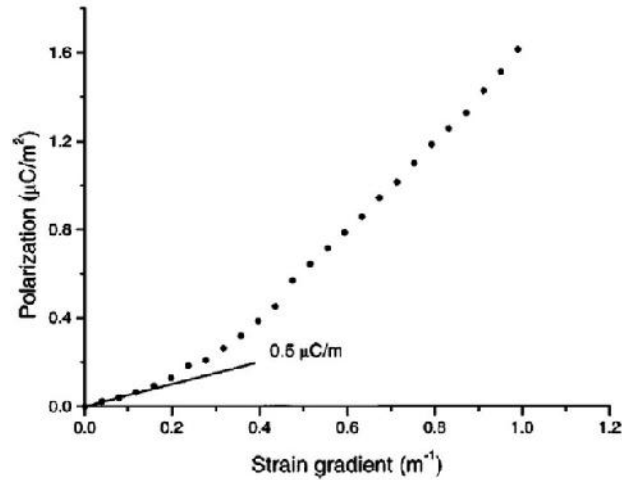


Figure 7.4. The polarization as a function of applied strain gradient in lead zirconate titanate¹⁹

This work established that the largest flexoelectric response in BST samples are measured while the material has local polar regions, and that the application of a strain gradient influences the alignment of the ferroelectric domain structure.

In order to directly study the impact of ferroelectricity on the flexoelectric response, a measurement apparatus was developed to characterize the flexoelectric polarization as a function of applied static and dynamic strain gradients. Remanent piezoelectric d_{33} measurements were made prior to and after each flexoelectric measurement using a Berlincourt meter, to assess the alignment of the polarization due to the applied strain gradient.

The measured polarization as a function of increasing and decreasing strain gradient is shown in Figure 7.5. It can be seen that the flexoelectric response increases rapidly at low applied strain gradients, with a slope of $209 \pm 7 \mu\text{C}/\text{m}$, slightly larger than the measurements made by Ma and Cross.¹ For applied strain gradients above 0.2 m^{-1} the slope levels off, indicating a decrease in the flexoelectric response. Similar behavior in lead zirconate titanate was attributed to the changes in the ferroelastic-ferroelectric response, allowing for the partial relaxation of the strain gradient.¹⁹

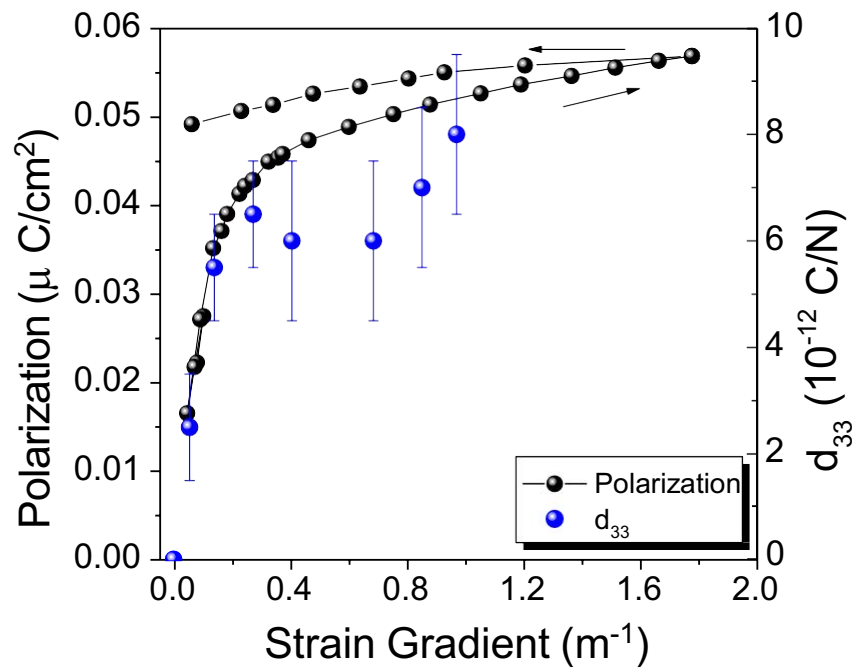


Figure 7.5. Hysteresis in polarization with increasing and decreasing applied strain gradient and the development of a piezoelectric response. The d_{33} measurements were taken after the strain gradient was removed, and hence are remanent piezoelectric coefficients.

The data in Fig. 7.6 on the remanent piezoelectric measurements show no initial d_{33} , which is consistent with an unpoled ferroelectric. However, after removal of the applied strain gradient there is a persistent polarization which produces the remanent d_{33} . These results are consistent with the flexo-poling results discussed previously. Although the piezoelectric response is small, the presence of piezoelectricity shows definitively that the flexoelectric measurement led to permanent changes in the alignment of the polar structures, and thus a non-flexoelectric enhancement to the polarization.

The Rayleigh analysis, flexoelectric poling and synchronized flexoelectric-piezoelectric measurements support the role of residual ferroelectricity in enhancing flexoelectricity in ceramic $\text{Ba}_{1-x}\text{Sr}_x\text{TiO}_3$. Local polar regions, associated with the order-disorder phenomena, would account for the observed residual ferroelectric behavior above T_C and the enhanced flexo-poling induced polarization, akin to what has been observed in relaxor ferroelectrics.²⁵ Although this is the first reported use of Rayleigh analysis above T_c in bulk BST ceramics, it can be inferred that residual ferroelectricity is likely prevalent, as evidenced by the hysteresis in the field dependence of permittivity, piezoelectricity in the paraelectric phase, or excessive dielectric loss observed in many studies.^{42,43,44,45} In the ferroelectric phase, piezoelectricity in BST provides some contribution to the total measured polarization under strain/strain gradient.

Given the fact that the motion of mobile interfaces contributes to the measured flexoelectric response above T_C , the processing, thermal, and elastic history should be expected to influence the measured flexoelectric response. This explains the anomalously large and diverse flexocoupling coefficients which have been reported.² As inconsistencies in flexocoupling are common amongst

ferroelectric perovskites, it is likely that ferroelectricity plays a role in the discrepancies observed in these materials as well.

7.4. Conclusions

In summary, residual ferroelectricity was observed in $\text{Ba}_{1-x}\text{Sr}_x\text{TiO}_3$ ceramics 30°C above the global phase transition temperature, within the temperature range commonly employed for flexoelectric measurements. Furthermore, the application of a strain gradient lead to strain gradient-induced poling, or flexoelectric poling, as observed by the development of remanent polarization in flexoelectric measurements, an induced d_{33} piezoelectric response and the production of an internal permanent bias within the polarization-electric field loops. All of these results point towards the flexoelectric poling of the residual ferroelectric response as the source of the observed enhancements in flexoelectric response.

7.5. References

1. Ma, W. & Cross, L. E. Flexoelectric polarization of barium strontium titanate in the paraelectric state. *Appl. Phys. Lett.* **81**, 3440–3442 (2002).
2. Zubko, P., Catalan, G. & Tagantsev, A. K. Flexoelectric Effect in Solids. *Annu. Rev. Mater. Res.* **43**, 387–421 (2013).
3. Cross, L. E. Flexoelectric effects: Charge separation in insulating solids subjected to elastic strain gradients. *J. Mater. Sci.* **41**, 53–63 (2006).

4. Fu, J. Y., Zhu, W., Li, N. & Cross, L. E. Experimental studies of the converse flexoelectric effect induced by inhomogeneous electric field in a barium strontium titanate composition. *J. Appl. Phys.* **100**, 024112 (2006).
5. Kogan, Sh M. Piezoelectric effect during inhomogeneous deformation and acoustic scattering of carriers in crystals. *Sov. Phys.-Solid State* **5** 2069–2070 (1964).
6. Tagantsev, A. K. Piezoelectricity and flexoelectricity in crystalline dielectrics. *Phys. Rev. B* **34**, 5883–5889 (1986).
7. Kwon, S. R., Huang, W. B., Zhang, S. J., Yuan, F. G. & Jiang, X. N. Flexoelectric sensing using a multilayered barium strontium titanate structure. *Smart Mater. Struct.* **22**, 115017 (2013).
8. Huang, W., Kwon, S.-R., Zhang, S., Yuan, F.-G. & Jiang, X. A trapezoidal flexoelectric accelerometer. *J. Intell. Mater. Syst. Struct.* **25**, 271-277 (2013).
9. Tagantsev, A. K. Pyroelectric, piezoelectric, flexoelectric, and thermal polarization effects in ionic crystals. *Sov. Phys. Uspekhi* **30**, 588 (1987).
10. Afanas'ev, V. P., Pronin, I. P. & Kholkin, A. L. Formation and relaxation mechanisms of the self-polarization in thin ferroelectric films. *Phys. Solid State* **48**, 1214–1218 (2006).
11. Jiangpeng Chen, Y. L. Upward ferroelectric self-polarization induced by compressive epitaxial strain in (001) BaTiO₃ films. *J. Appl. Phys.* **113**, 20 (2013).
12. Pertsev, N. A., Tagantsev, A. K. & Setter, N. Phase transitions and strain-induced ferroelectricity in SrTiO₃ epitaxial thin films. *Phys. Rev. B* **61**, R825–R829 (2000).
13. Uwe, H., Yamaguchi, H. & Sakudo, T. Ferroelectric microregion in KTa_{1-x}Nb_xO₃ and SrTiO₃. *Ferroelectrics* **96**, 123–126 (1989).

14. Petzelt, J., Ostapchuk, T., Pashkin, A. & Rychetský, I. FIR and near-millimetre dielectric response of SrTiO₃, BaTiO₃ and BST films and ceramics. *J. Eur. Ceram. Soc.* **23**, 2627–2632 (2003).
15. Zubko, P., Catalan, G., Buckley, A., Welche, P. R. L. & Scott, J. F. Strain-Gradient-Induced polarization in SrTiO₃ single crystals. *Phys. Rev. Lett.* **99**, 167601 (2007).
16. Narvaez, J. & Catalan, G. Origin of the enhanced flexoelectricity of relaxor ferroelectrics. *Appl. Phys. Lett.* **104**, 162903 (2014).
17. Ma, W. & Cross, L. E. Large flexoelectric polarization in ceramic lead magnesium niobate. *Appl. Phys. Lett.* **79**, 4420–4422 (2001).
18. Ma, W. & Cross, L. E. Flexoelectricity of barium titanate. *Appl. Phys. Lett.* **88**, 232902 (2006).
19. Ma, W. & Cross, L. E. Strain-gradient-induced electric polarization in lead zirconate titanate ceramics. *Appl. Phys. Lett.* **82**, 3293–3295 (2003).
20. Xu, T., Wang, J., Shimada, T. & Kitamura, T. Direct approach for flexoelectricity from first-principles calculations: cases for SrTiO₃ and BaTiO₃. *J. Phys. Condens. Matter* **25**, 415901 (2013).
21. Shu, L., Wei, X., Jin, L., Li, Y., Wang, H., & Yao, X. Enhanced direct flexoelectricity in paraelectric phase of Ba(Ti_{0.87}Sn_{0.13})O₃ ceramics. *Appl. Phys. Lett.* **102**, 152904 (2013).
22. Rayleigh, Lord. XXV. Notes on electricity and magnetism.—III. On the behaviour of iron and steel under the operation of feeble magnetic forces. *Philos. Mag. Ser. 5* **23**, 225–245 (1887).
23. Damjanovic, D., Taylor, D. Contributions to the nonlinear dielectric and piezoelectric response of ferroelectric thin films and ceramics. *Ferroelectrics*, 221.1, 137-146. (1999).

24. Jin, L., Porokhonsky, V. & Damjanovic, D. Domain wall contributions in $\text{Pb}(\text{Zr},\text{Ti})\text{O}_3$ ceramics at morphotropic phase boundary: A study of dielectric dispersion. *Appl. Phys. Lett.* **96**, 242902 (2010).
25. Taylor, D. V. & Damjanovic, D. Evidence of domain wall contribution to the dielectric permittivity in PZT thin films at sub-switching fields. *J. Appl. Phys.* **82**, 1973–1975 (1997).
26. N. Bassiri Gharb. Dielectric and Piezoelectric Nonlinearities in Oriented $\text{Pb}(\text{Yb}_{1/2}\text{Nb}_{1/2})\text{O}_3$ - PbTiO_3 Thin Films. Ph.D. dissertation, Dept. of Mat. Sci and Eng., Penn. State University, University Park, PA, 2005.
27. Garten, L. M., Lam, P., Harris, D., Maria, J.-P. & Trolier-McKinstry, S. Residual ferroelectricity in barium strontium titanate thin film tunable dielectrics. *J. Appl. Phys.* **116**, 044104 (2014).
28. Bassiri-Gharb, N., Fujii, I., Hong, E., Trolier-McKinstry, S., Taylor, D. V., Damjanovic, D., Domain wall contributions to the properties of piezoelectric thin films. *J. Electroceramics* **19**, 49–67 (2007).
29. Tikhomirov, O., Jiang, H. & Levy, J. Direct observation of local ferroelectric phase transitions in $\text{Ba}_x\text{Sr}_{1-x}\text{TiO}_3$ thin films. *Appl. Phys. Lett.* **77**, 2048–2050 (2000).
30. Bussmann-Holder, A., Beige, H. & Völkel, G. Precursor effects, broken local symmetry, and coexistence of order-disorder and displacive dynamics in perovskite ferroelectrics. *Phys. Rev. B* **79**, 184111 (2009).
31. D. A. Tenne, A. Soukiassian, X. X. Xi, H. Choosuwana, R. Guo, and A. S. Bhalla, “Lattice dynamics in $\text{Ba}_x\text{Sr}_{1-x}\text{TiO}_3$ thin films studied by Raman spectroscopy,” *Journal of Applied Physics*, vol. 96, no. 11, pp. 6597–6605, Nov. 2004.

32. Ko, J.-H., Kim, T. H., Roleder, K., Rytz, D. & Kojima, S. Precursor dynamics in the ferroelectric phase transition of barium titanate single crystals studied by Brillouin light scattering. *Phys. Rev. B* **84**, 094123 (2011).
33. Petkov, V., Gatashki, M., Niederberger, M. & Ren, Y. Atomic-Scale Structure of Nanocrystalline $\text{Ba}_x\text{Sr}_{1-x}\text{TiO}_3$ ($x = 1, 0.5, 0$) by X-ray Diffraction and the Atomic Pair Distribution Function Technique. *Chem. Mater.* **18**, 814–821 (2006).
34. Dobal, P. S., Dixit, A., Katiyar, R. S., Garcia, D., Guo, R., & Bhalla, A. S. Micro-Raman study of $\text{Ba}_{1-x}\text{Sr}_x\text{TiO}_3$ ceramics. *J. Raman Spectrosc.* **32**, 147–149 (2001).
35. A. Soukiassian D. A. Tenne. Raman study of $\text{Ba}_x\text{Sr}_{1-x}\text{TiO}_3$ films: Evidence for the existence of polar nanoregions. *Phys. Rev. B* **67**, 012302 (2003).
36. Robert, G., Damjanovic, D. & Setter, N. Preisach modeling of ferroelectric pinched loops. *Appl. Phys. Lett.* **77**, 4413–4415 (2000).
37. Catalan, Gustau, A. Lubk, A. H. G. Vlooswijk, E. Snoeck, C. Magen, A. Janssens, G. Rispens, G. Rijnders, D. H. A. Blank, and B. Noheda. Flexoelectric rotation of polarization in ferroelectric thin films. *Nat. Mater.* **10**, 963–967 (2011).
38. Lee, D., Yoon, A., Jang S. Y., Yoon, J.-G., Chung, J.-S., Kim, M., Scott, J. F., Noh, T. W. Giant flexoelectric effect in ferroelectric epitaxial thin films. *Phys. Rev. Lett.* **107**, 057602 (2011).
39. Gruverman, A., Rodriguez, B. J., Kingon, A. I., Nemanich, R. J., Tagantsev, A. K., Cross, J. S., & Tsukada, M. Mechanical stress effect on imprint behavior of integrated ferroelectric capacitors. *Appl. Phys. Lett.* **83**, 728–730 (2003).
40. Lu, H., Bark, C. W., De los Ojos, D. E., Alcalá, J., Eom, C. B., Catalan, G., & Gruverman, A. Mechanical Writing of Ferroelectric Polarization. *Science* **336**, 59–61 (2012).

41. Gevorgian, S. S. & Kollberg, E. L. Do we really need ferroelectrics in paraelectric phase only in electrically controlled microwave devices? *IEEE Trans. Microw. Theory Tech.* **49**, 2117–2124 (2001).
42. Vendik, O. G., Hollmann, E. K., Kozyrev, A. B. & Prudan, A. M. Ferroelectric tuning of planar and bulk microwave devices. *J. Supercond.* **12**, 325–338 (1999).
43. Nath, R., Zhong, S., Alpay, S. P., Huey, B. D. & Cole, M. W. Enhanced piezoelectric response from barium strontium titanate multilayer films. *Appl. Phys. Lett.* **92**, 012916 (2008).
44. Fu, C., Yang, C., Chen, H., Hu, L., & Dai, L. Domain configuration and dielectric properties of $\text{Ba}_{0.6}\text{Sr}_{0.4}\text{TiO}_3$ thin films. *Appl. Surf. Sci.* **252**, 461–465 (2005).

Chapter 8

Reliability, Degradation and Failure Mechanisms in Lead Zirconate Titanate Films

8.1 Introduction

As electronics usage grows, defining the limits of reliability and lifetime for electronic components becomes a priority. The reliability of thin film tunable dielectrics and piezoelectrics impacts a wide range of applications including personal electronics, sensors, and energy harvesters.^{1,2} As with any electrical system, electrical failure can occur under electric field, stress, or thermal cycling.

Although reliability in bulk BaTiO₃ capacitors is understood to be controlled by the migration of oxygen vacancies under electric fields,³ in PZT thin films there is no consensus on the dominant conduction mechanisms or lifetime-controlling defect.⁴ Table 8.1 provides a survey of the literature on reliability for lead zirconate titanate, PZT, thin films. The first column indicates the reference, the second the reported conduction mechanism (SC: space charge, PF: Poole-Frenkel), the next few columns describe the electrodes, the film thickness (t), the deposition method (CSD: chemical solution deposition, RF: radio frequency sputtering), crystallization conditions, the method of characterization, the criteria for failure, p or n-type conductivity, and the activation energy or voltage acceleration factors if reported. The disparate conclusions from each of these studies highlight the importance of avoiding assumptions about the conduction mechanisms while developing lifetime models.

In this work, the reliability of sputtered and CSD PZT thin films is characterized using highly accelerated lifetime testing and leakage current-voltage measurements. Lifetime models are developed based on the dominant conduction mechanisms determined from the measured leakage current-voltage response. Additionally, supplemental methods of reliability characterization, such as voltage contrast microscopy are discussed. This chapter also summarizes work from former group members Manabu Hagiwara and Song Won Ko.

Table 8.1. Compilation of previous literature on reliability in PZT thin films

Ref#	Conduction Mechanism	Electrodes	t	Deposit	Testing	Criteria	E_a	N
		Btm/top	nm				eV	
[5]	SC	Pt/IrO ₂	250	CSD	Model	FS	--	--
[6]	Schottky	Pt/Au	450	CSD	I(V,t)	SF	--	--
[7]	Schottky	Pt/Au	170	RF	I(V,t)	SF	--	--
[4]	PF	Pt/Pt	800	CSD	HALT	10x Jmin	0.6--1.0	4--5
[8]		Pt/Pt	880	CSD	HALT	10 ⁻³ A	1.1	5.3
[9]		Pt/Pt	1000	CSD	HALT	10 ⁻³ A	0.78	7.8
[10]	PF	LSCO	300	PLD	I(V,T)	SF	0.5-0.6	--
[11]	SC	Pt/Au	600	RF	I(t)	FS	--	9.6
[12]	Schottky	Pt/Pt	150	CSD	I(V)	SF	--	0.33
[13]	Schottky	Pt/Pt	280	CSD	I(V,t)	SF	--	--
[13]	PF	Pt/Pt	281	CSD	I(V,t)	SF	--	--
[14]	Ionic	Pt/Pt	950	CSD	I(V,t)	SF	--	--
[15]	Schottky	Pt/Au	600	RF	I(V,t)	SF	--	--
[16]	Schottky	Pt/Pt, IrO ₂	380	CSD	I(V,t)	SF	--	--
[16]	SC	Pt/SRO	380	CSD	I(V,t)	SF	--	--
[17]	PF	Pt/LSCO	160	CSD	I(V,t)	SF	--	--
[17]	PF	Pt/SRO	160	CSD	I(V,t)	SF	--	--
[17]	Schottky	Pt/Pt	160	CSD	I(V,t)	SF	--	--

8.2 Methods

Samples were measured from three different PZT thin film sources. Chemical solution deposited and sputtered, approximately 1 μm thick $\{100\}$ oriented $\text{Pb}(\text{Zr}_{0.52},\text{Ti}_{0.48})\text{TiO}_3$ thin films provided by Samsung Electromechanics. These will be referred to as Sol-gel (100) and Sputtered (100). Chemical solution deposited $\text{Pb}(\text{Zr}_{0.52},\text{Ti}_{0.48})\text{TiO}_3$ thin films were also developed at Penn State. These films were also approximately 1 μm thick and are referred to as PSU sol-gel (111). All films used top and bottom platinum electrodes.

Leakage current measurements were taken on a 4140 pico-Ampere Meter/DC Voltage Source (Hewlett Packard). Prior to any current-voltage measurements, the time dependent current under constant voltage was measured in order to determine the steady state conditions.

Highly accelerated lifetime testing, HALT, was conducted on sputtered and chemical solution deposited $\text{Pb}(\text{Zr}_{0.52},\text{Ti}_{0.48})\text{TiO}_3$ thin films provided by Samsung Electromechanics, as well as films of the same composition made by chemical solution deposition at PSU. 200 μm diameter top platinum electrodes were deposited by sputtering and annealed at 550 $^{\circ}\text{C}$ for two minutes in flowing oxygen. The films were then sectioned into approximately 1cm by 1cm squares which were mounted with silver paste to 24 pin DIP packages (Spectrum Semiconductor Materials, Inc.). After allowing the past to set for 24 hours, the top electrodes were wirebonded (Kulicke and Soffa) to the contact pads of the package with gold wire as shown in Figure 8.1. Capacitance and dielectric loss measurements were taken before and after wirebonding to insure no degradation occurred due to wirebonding. Five samples with approximately 20 capacitors per condition were made for highly accelerated lifetime testing, for three tests at constant voltage and three at constant temperature.

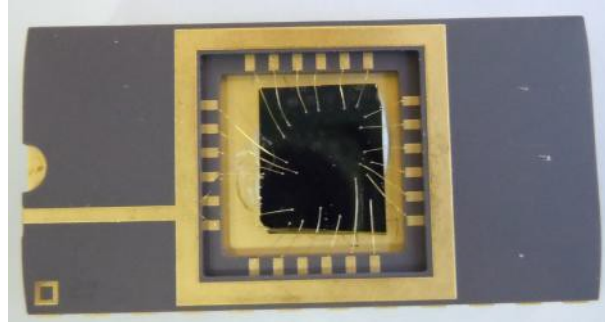


Figure 8.1. Image of the PZT films after wire bonding to the top and bottom electrodes

Constant voltage HALT tests were conducted at temperature from 120 °C to 220 °C at 150 kV/cm for all samples (except the sputtered samples, which were tested at 100 kV/cm due to low lifetimes). This HALT temperature and voltage range was pre-determined by current-voltage measurements within this range. HALT tests were conducted from 95 kV/cm to 250 kV/cm at 100°C or 120°C. Weibull analysis was used to determine the median time to failure for each temperature-voltage set, as well as the distribution of failure times within each set.

Once the mean time to failure of a set of capacitors was determined from the lifetime measurements under a set applied voltage and temperature, then the expected lifetime under different conditions was predicted by the Eyring Equation, shown below:

$$\frac{t_1}{t_2} = \left(\frac{V_1}{V_2} \right)^{-N} \exp \left[\frac{E_a}{k_B} \left(\frac{1}{T_1} - \frac{1}{T_2} \right) \right]$$

where t is the mean time to failure, V is the applied voltage, N is the voltage acceleration factor, E_a is the activation energy, k_B is the Boltzmann's constant, and T is the measurement temperature.⁸

This equation was used to determine the activation energy and the voltage acceleration factor. In this equation, it is implicitly assumed that the dominant mechanism of conduction does not change over the temperature and field range probed

8.3 Results

Figure 8.2 shows the characteristic leakage current response as a function of time under applied voltage and temperature for a randomly oriented, 1 μm thick, chemical solution deposited $\text{Pb}(\text{Zr}_{0.52}\text{Ti}_{0.48})\text{O}_3$ thin film. The leakage current at each temperature and voltage underwent a long interval of steady state prior to a period of gradual degradation. The period of degradation was followed by a nearly instantaneous increase in the leakage current. This type of response is commonly observed in PZT thin films⁴ but differs greatly from the more gradual degradation to failure seen in bulk BaTiO_3 dielectrics³, which suggests differences in the failure mechanisms. The time of failure was set as the time at which the leakage current increased an order of magnitude from the minimum measured leakage current at steady state, as indicated by an arrow in Figure 8.2. The discontinuous increase in leakage current was often concurrent with the onset of failure, although occasional spikes in leakage occurred during local Joule heating failure events which then recovered once the short was removed.

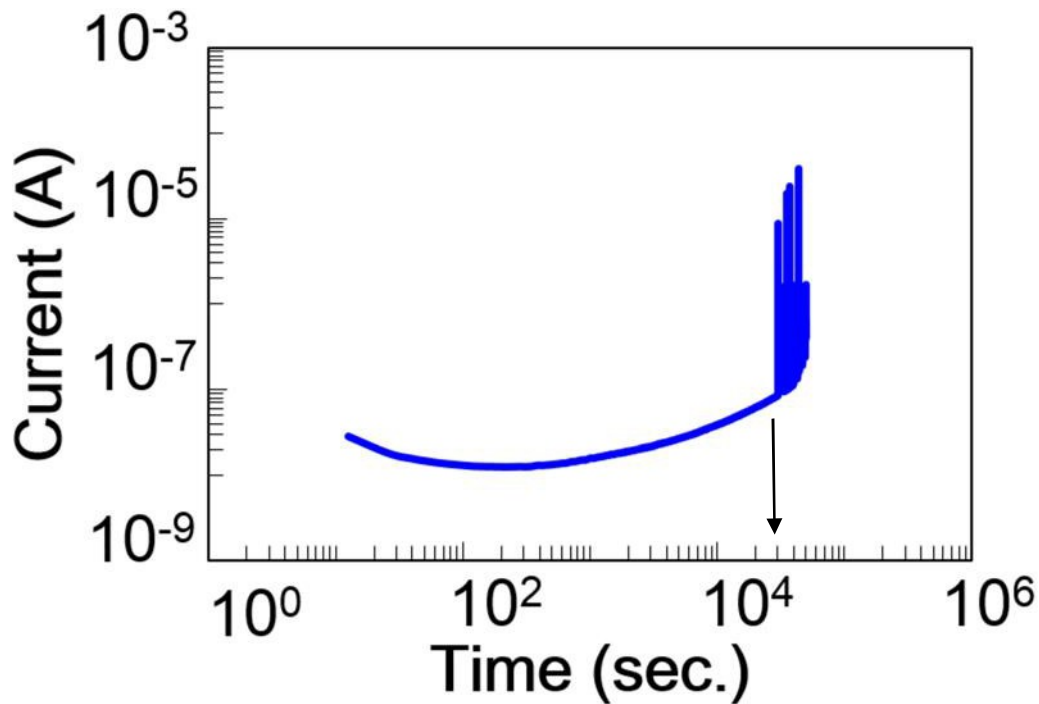


Figure 8.2. Leakage current as a function of time for a randomly oriented, 1 μm thick, chemical solution deposited $\text{Pb}(\text{Zr}_{0.52}\text{Ti}_{0.48})\text{O}_3$ thin film taken at 150 kV/cm and 180 $^{\circ}\text{C}$

Figure 8.3 shows the time to failure for a set of 23 PZT capacitors from a chemical solution deposited film. The black lines indicate the data range used to calculate the median time to failure. Premature failures were excluded from the fit as they likely are induced by flaws and do not reflect the same conduction mechanism dominating the response of the material. Weibull analysis was used to calculate the median time to failure, MTF, for each data set. Table 8.2 presents the median time to failure and Weibull fitting parameters for the data set shown in Figure 8.3. Materials with a Weibull fitting parameter (Weibull modulus) less than one were excluded because of the large uncertainty in the fit.

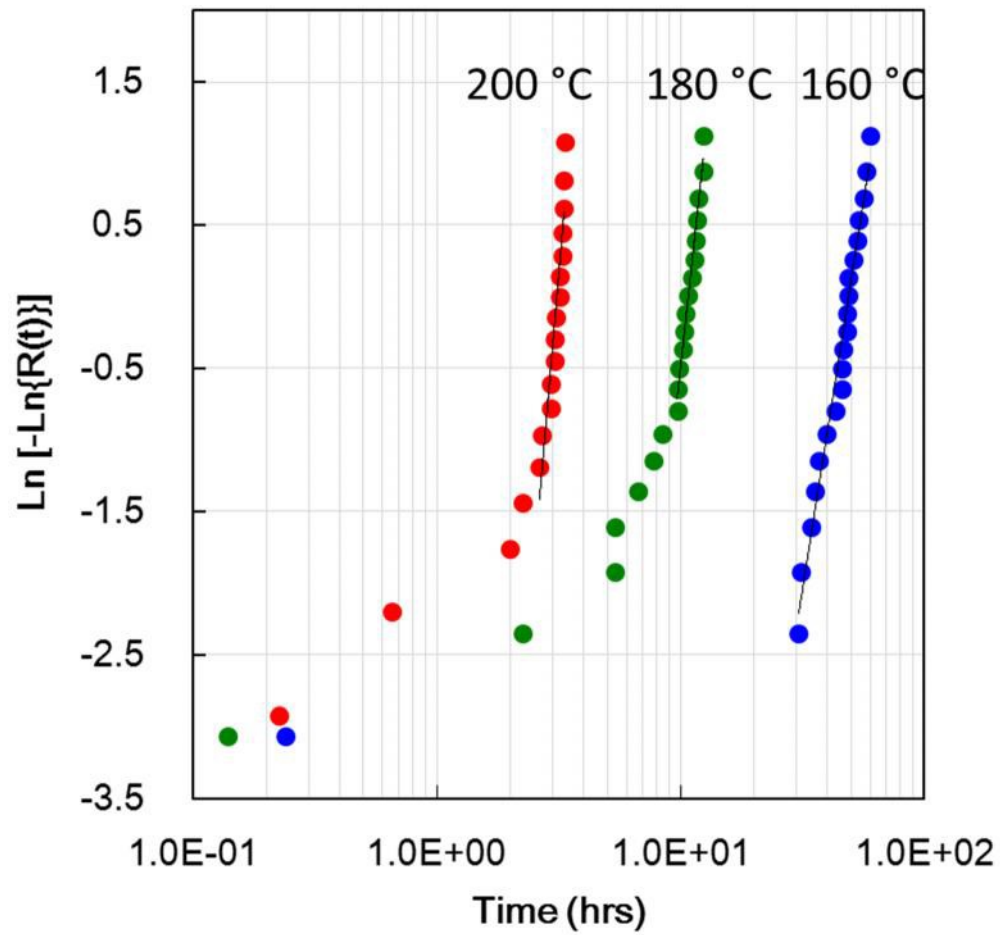


Figure 8.3. The time to failure for data sets at three temperatures from a CSD PZT thin film

Table 8.2. Median time to failure and Weibull fitting parameter for each temperature data set

Temp. (°C)	β	t_{50} (hours)
160	4.70 ± 0.18	45.2 ± 9.5
180	6.77 ± 0.29	10.2 ± 1.5
200	8.61 ± 0.87	2.98 ± 0.49

Figure 8.4 shows the natural log of the median time to failure plotted as a function of temperature. The slope of the fitting was used to determine the activation energy of the mechanism leading to degradation through the temperature dependence of the Eyring equation:

$$t = C_V \exp \frac{E_a}{k_B T}$$

where t is the median time to failure, C_V is a constant, k_B is Boltzmann's constant, and T is temperature.

Table 8.4 presents the calculated activation energy, and the voltage acceleration factor for the samples shown in Figure 8.4. Table 8.3 provides a compilation of activation energies and their associated mechanisms observed in previous studies on lead-based perovskites. An activation energy of 0.6 eV is consistent with the movement of oxygen vacancies,³ but the degradation mechanism associated with a 1.2 eV activation energy is uncertain.

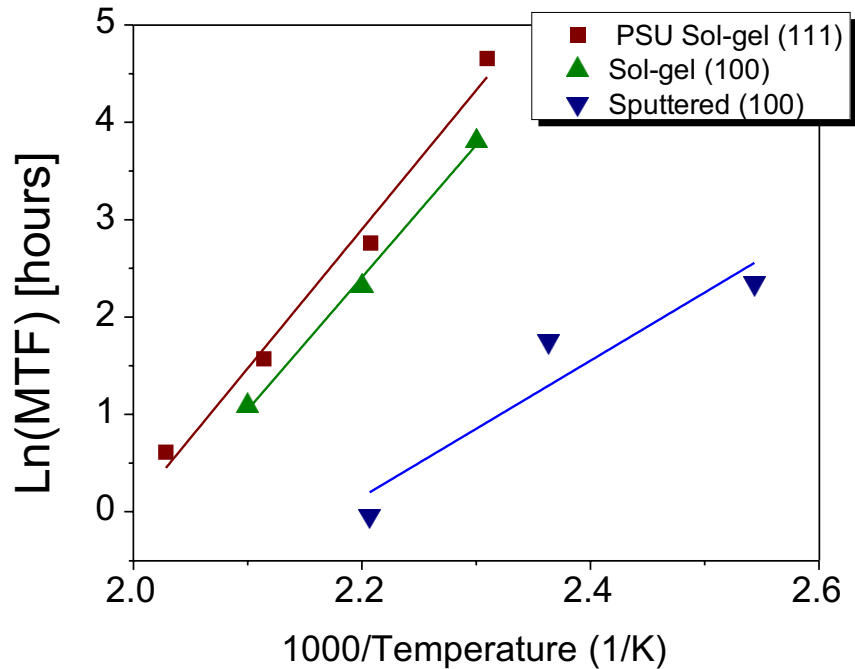


Figure 8.4. Median time to failure PZT thin films deposited by different methods, as a function of temperature at a constant voltage. While the chemical solution deposited films were tested at 150 kV/cm, the short lifetimes of the sputtered films required a reduction in the field to 100 kV/cm.

Table 8.3. Previous studies on mechanisms associated with a given activation energy in PZT.

From reference ¹⁵

Composition	Method	E_a (eV)	Mechanism	Reference
PZT thin film capacitor	I - V - T	1.3 0.6–1	V_{Pb}'' hole migration: $p \sim 2[V_{Pb}'']$ V_O'' bulk diffusion	Al-Shareef and Dimos (1997) (Ref. 9)
Pb(Zr _{1-x} Ti _x)O ₃ bulk	I - V - T	0.3 0.7	Hopping between Pb ³⁺ and Pb ²⁺ Acceptor ionization	Raymond and Smyth (1996) (Ref. 12)
Pb(Zr _{1-x} Ti _x)O ₃ bulk	I - V - T	1.4 1.1	V_{Pb}'' hole migration: $p \sim 2[V_{Pb}'']$ Sc-doped acceptor ionization	Dih and Fulrath (1978) (Ref. 13)
Pb(Zr _{1-x} Ti _x)O ₃ bulk	Young's modulus	0.82–1.05	Interaction between domain walls and oxygen vacancies	Zarycka <i>et al.</i> (2005) (Ref. 14)
Pb(Zr _{1-x} Ti _x)O ₃ film	Tracer O ¹⁸	2.7 0.6	V_O'' Surface diffusion V_O'' bulk diffusion	Wang and McIntyre (2005) (Ref. 15)
Pb(Zr _{1-x} Ti _x)O ₃ bulk	EPR	0.26 1	Hopping between Pb ³⁺ and Pb ²⁺ Ti ³⁺ excitation to conduction band	Robertson <i>et al.</i> (1993) (Ref. 16)
Pb(Zr _{1-x} Ti _x)O ₃ bulk	IS	0.6–0.8	V_O'' bulk diffusion	Boukamp <i>et al.</i> (2004) (Ref. 17)
PZN-4.5PT bulk	IS	0.59	V_O'' bulk diffusion	Kobor <i>et al.</i> (2007) (Ref. 18)
(Pb,La)TiO ₃ and (Pb,La)(Zr,Ti)O ₃ bulk	IS	0.36–0.67	V_O'' bulk diffusion	Kang <i>et al.</i> (2003) (Ref. 19)

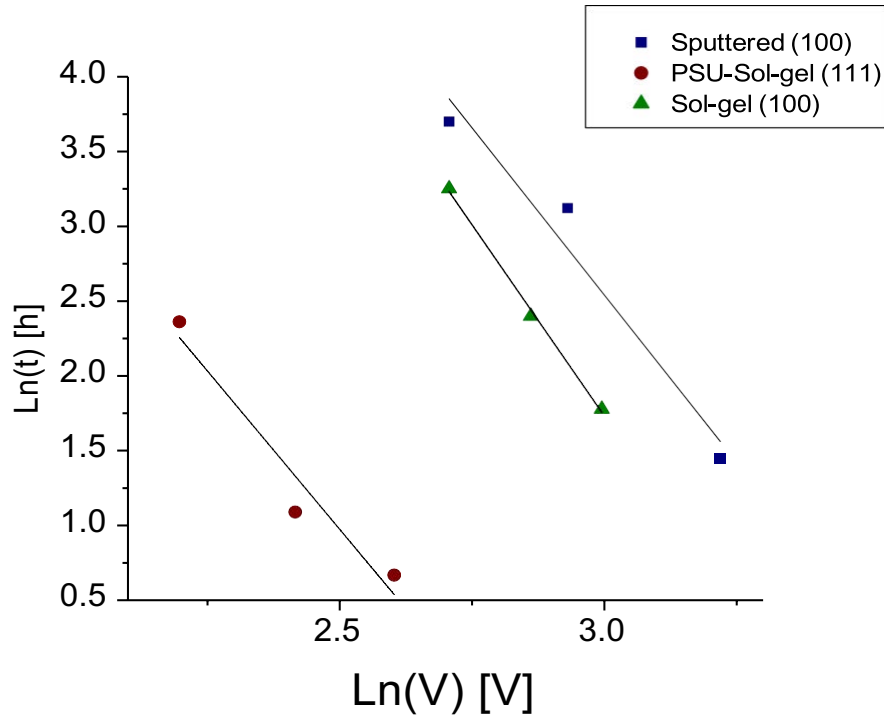


Figure 8.5. Median time to failure as a function of voltage at constant temperature of 150 °C for PZT thin films

Figure 8.5 shows the highly accelerated lifetime testing at constant temperature and varying applied voltage. The slope of the fitting was used to determine the activation energy of the mechanisms leading to degradation through the Eyring equation:

$$t = C_T V^{-N}$$

where t is the median time to failure, C_T is a constant, V is the voltage applied, and N is the voltage acceleration factor. Table 8.4 presents the calculated activation energy, and the voltage acceleration factor for the samples shown in Figure 8.5.

The voltage acceleration factors determined from the Eyring equation were incongruent with established models for possible conduction mechanisms (See Table 8.5). Amongst these possible conduction mechanisms, none have a fourth or fifth order polynomial relationship between the electric field and the leakage current in the material. This indicates that the voltage acceleration model derived from the Eyring equation is unphysical, which calls into question the assumption made about the mechanisms of failure within these films. In order to reliably predict lifetime for PZT thin films, a new model based on the physical mechanisms of failure for that material is necessary. This has been done for bulk BaTiO₃ ceramic dielectrics.¹⁸ Here, the applicability of the new model to thin films are necessary is explored.

Table 8.5. List of conduction mechanisms in dielectrics¹⁹**Table 10-2.** Conduction Mechanisms in Insulators

Mechanism	J- ϵ Characteristics	Experimentally Derivable Material Constants
1. Schottky Emission	$J_S = AT^2 \exp - \frac{q\Phi_B}{kT} \exp \left[\frac{1}{kT} \left(\frac{q^3 \epsilon}{4\pi \epsilon_i} \right)^{1/2} \right]$ (10-21)	Φ_B
2. Tunneling	$J_T = \frac{q^2 \epsilon^2}{8\pi h \Phi_B} \exp - \left[\frac{8\pi (2m)^{1/2}}{3hq\epsilon} (q\Phi_B)^{3/2} \right]$ (10-22)	Φ_B
3. Space Charge Limited	$J_{SCL} = \frac{9\mu\epsilon_i}{8} \frac{\epsilon^2}{d}$ (10-23)	—
4. Ionic Conduction	$J_I = \frac{a\epsilon}{kT} \exp - \frac{E_i}{kT}$ (10-24)	E_i
5. Intrinsic Conduction	$J_{In} = bT^{3/2} \exp - \frac{E_g}{2kT} \cdot \epsilon$ (10-25)	E_g
6. Poole-Frenkel Emission	$J_{PF} = c\epsilon \exp - \frac{E_i}{kT} \exp \left[\frac{1}{kT} \left(\frac{q^3 \epsilon}{\pi \epsilon_i} \right)^{1/2} \right]$ (10-26)	E_i

$a, b, c = \text{constant.}$

$\epsilon_i = \text{insulator dielectric constant.}$

In order to determine the dominant physical mechanism of conduction in these films, leakage current measurements as a function of applied voltage were employed. Figure 8.6 shows the results of this measurement for the CSD films developed at PSU. The results were fit to the equations for possible conduction through the film. The best fit was found for the Schottky conduction model described by:

$$\ln\left(\frac{J}{T^2}\right) = \ln A - \frac{\Phi_B}{k_B T} + \frac{q \sqrt{q E 4 \epsilon_0 \epsilon_\infty \pi}}{k_B T} E^{1/2}$$

were A is the Richardson constant, and ϵ_∞ is the high frequency permittivity. Furthermore, the permittivity derived from the equations for Schottky conduction was consistent with the theoretical values for high frequency permittivity. The calculated values ranged between 1.77 ± 0.03 and 2.13 ± 0.08 and the expected values are between 2.1 and 2.6. Schottky conduction was concluded to be the dominant conduction mechanism. It should be stressed that these results are exclusive to the films within this study and are not claimed as the only mechanisms of conduction possible within PZT films, which might vary greatly between processing methods or electrode material.

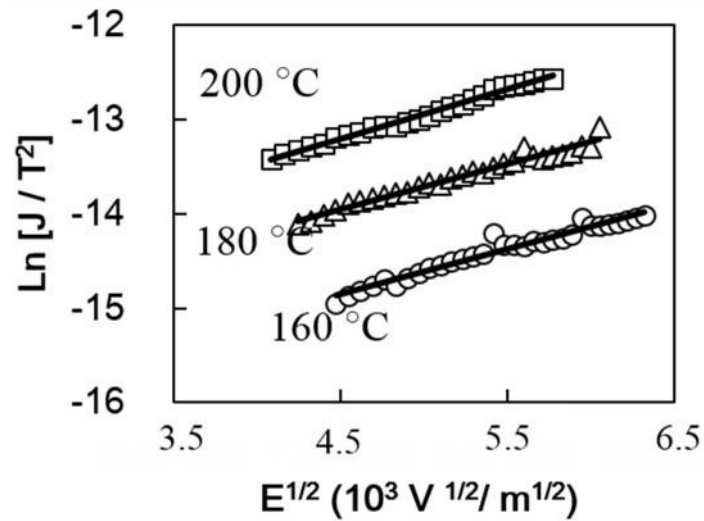


Figure 8.6. Fitting of the leakage current-voltage measurements over a range of temperature for CSD PZT thin films

Using the assumptions of constant critical charge to failure (borrowed from the semiconductor industry²⁰) and the equations for Schottky conduction new models for reliability were developed. The new fitting equations were derived through the following process:

$$Q_{critical} = constant = jt$$

$$j_1 t_1 = j_2 t_2$$

$$j_s = AT^2 e^{\left(\frac{-q\phi}{kT}\right)} e^{\left(\frac{1}{kT} \left(\frac{q^3 E}{4\pi\epsilon_i}\right)^{\frac{1}{2}}\right)}$$

$$\frac{t_1}{t_2} = \frac{T_2^2 e^{\left(\frac{-q\phi}{kT_2}\right)} e^{\frac{1}{kT_2} \left(\frac{q^3 E_2}{4\pi\epsilon_i}\right)^{\frac{1}{2}}}}{T_1^2 e^{\left(\frac{-q\phi}{kT_1}\right)} e^{\frac{1}{kT_1} \left(\frac{q^3 E_1}{4\pi\epsilon_i}\right)^{\frac{1}{2}}}}$$

Constant voltage

$$\frac{t_1}{t_2} = \left(\frac{T_2}{T_1}\right)^2 e^{\frac{\gamma k T_2 - \gamma k T_1}{k^2 T_2 T_1}}$$

$$\gamma = -q\phi + \alpha E^{\frac{1}{2}}$$

$$\alpha = \frac{q^3}{4\pi\epsilon_i}$$

Constant temperature

$$\frac{t_1}{t_2} = e^{\beta E_2^{\frac{1}{2}} - \beta E_1^{\frac{1}{2}}}$$

$$\beta = \frac{\alpha}{kT}$$

$$\frac{t_1}{t_2} = e^{\beta E_2^{\frac{1}{2}} - \beta E_1^{\frac{1}{2}}}$$

where t is the median time to failure, Q is the total charge and q is the charge of the carrier. Figure 8.7 shows the data from Figure 8.5 replotted according to these equation; the data are tabulated in Table 8.4.

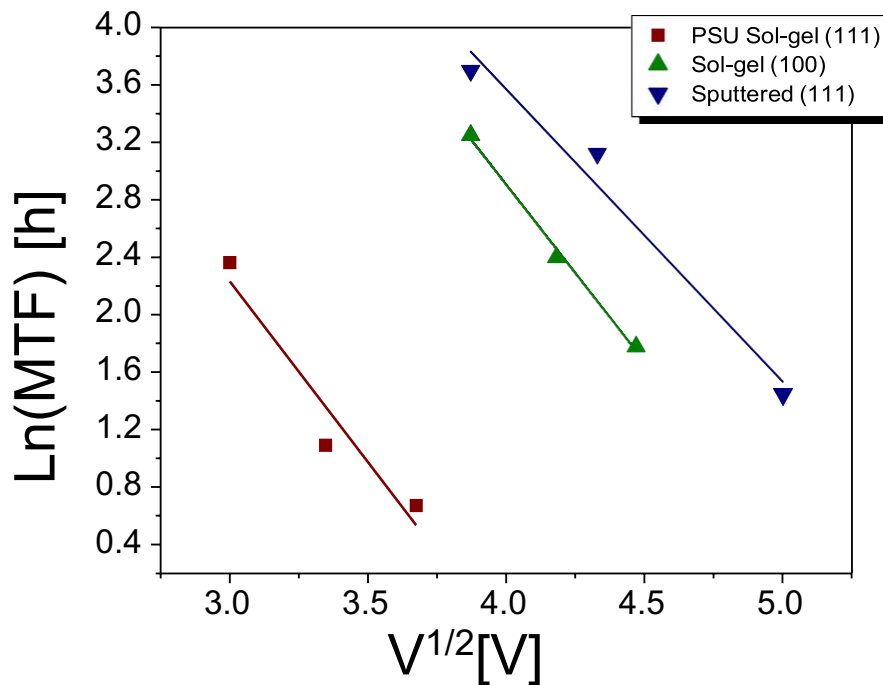


Figure 8.7. Refitting the highly accelerated lifetime testing for $\text{Pb}(\text{Zr},\text{Ti})\text{O}_3$ thin films deposited by different methods with different crystallographic orientations. The predicted voltage acceleration factor for the refit data is -2, which is in good agreement with the refit slopes

Table 8.4. Activation energy and voltage acceleration factor determined from the Eyring model and the voltage acceleration calculated from the new model

	PSU 111	CSD 100	Sputtered 100
Activation Energy	1.2 ± 0.1 eV	1.2 ± 0.04 eV	0.6 ± 0.2 eV (100 kV/cm)
Voltage Acceleration Factor	5.1 ± 0.3	4.5 ± 0.9	4.2 ± 1 (200 °C)
Voltage Acceleration Factor (New Model)	-2.5 ± 0.7	-2.46 ± 0.2	-2.0 ± 0.3 (200 °C)

The voltage acceleration was found to be between -2 and -2.5 for all data sets, which is consistent with the predicted slope, -2 of the new model. These results highlight the importance of establishing lifetime models based off of the physical mechanisms of degradation. This model should facilitate reliable lifetime predictions in PZT thin films.

Additionally, the activation energies for failure of the sol-gel PZT samples considerably exceeds the reported values for motion of oxygen vacancies in the material. Nonetheless, the very slow failures (e.g. long lifetimes) of the film, suggest that either the buildup of the injected charge is quite slow, or that the key barrier in the system is affected by some slow-moving species (such as ionic defects). That is, the failure may involve a coupled mechanism in which the energy barrier for the failure process is changed by a second process.

8.4 Supplementary Measurements: Voltage Contrast Microscopy and Optical Microscopy

Voltage contrast microscopy is another method which can be used to characterize the reliability and degradation of a thin film device. Voltage contrast microscopy investigates the real time degradation of a material through the application of voltage during scanning electron microscopy. Shown in Figure 8.8 are two areas of a PZT thin film device under 30 Volts. No post processing changes were made to the contrast of these images. These films were under voltage for 4.5 hours prior to the taking of these images. Over this time the electric field was observed to bleed into the dielectric within certain regions as indicated by the increased contrast in degraded areas. Over time the intensity of the contrast would increase, suggesting injected charge, until failure occurred with the complete destruction of the electrode area. Due to the fact that information provided by voltage contrast microscopy is limited to the surface of the sample, this method would be most beneficially employed for interdigitated electrodes or features with tight line spacing.

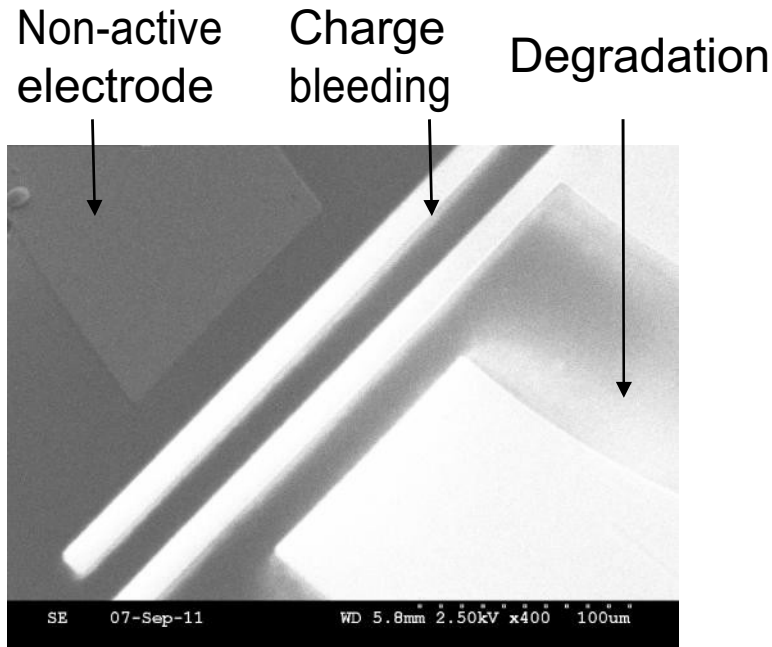


Figure 8.8. Voltage contrast microscopy of PZT thin film devices under 30 V for 4.5 hours showing regions of resistance degradation

Additionally scanning electron microscopy and optical microscopy can also be used to investigate failure in thin film dielectrics. Figure 8.9 shows an image of a scanning electron micrograph of an electrode following a failure event. Regions within the damaged electrode are highlighted in Figure 8.9. The observed failure in this instance likely occurred due to local Joule heating due to electric field concentration at a defect. After a period of time under electric fields these regions partially vaporize. Often electrodes will show many darkened areas associated with the removal of material through Joule heating at a flaw. These events may or may not lead to failure if the cause of the short is removed completely.

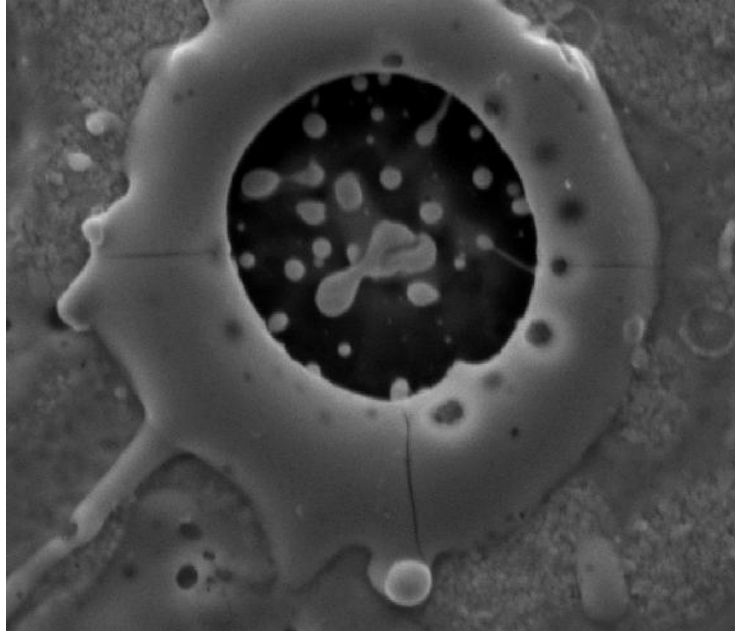


Figure 8.9. Scanning electron micrograph of an area of ejected material after electrical testing in a PZT thin film

8.5. References

1. Berge, J., Norling, M., Vorobiev, A. & Gevorgian, S. Field and temperature dependent parameters of the dc field induced resonances in $\text{Ba}_x\text{Sr}_{1-x}\text{TiO}_3$ -based tunable thin film bulk acoustic resonators. *J. Appl. Phys.* **103**, 064508 (2008).
2. Murali, P., Polcawich, R. G. & Trolor-McKinstry, S. Piezoelectric thin films for sensors, actuators, and energy harvesting. *MRS Bull.* **34**, 658–664 (2009).
3. Waser, R., Baiatu, T. & Härdtl, K. dc Electrical degradation of perovskite-type titanates: I, Ceramics. *J. Am. Ceram. Soc.* **73**, 1645–1653 (1990).

4. Al-Shareef, H. N. & Dimos, D. Leakage and reliability characteristics of lead zirconate titanate thin-film capacitors. *J. Am. Ceram. Soc.* **80**, 3127–3132 (1997).
5. Bouyssou, E., R. Jérision, N. Cézac, P. Leduc, G. Guégan, and C. Anceau, Wafer level reliability and leakage current modeling of PZT capacitors. *Mater. Sci. Eng. B* **118**, 28–33 (2005).
6. Yang, Y. S., Lee, S. J., Kim, S. H., Chae, B. G. & Jang, M. S. Schottky barrier effects in the electronic conduction of sol–gel derived lead zirconate titanate thin film capacitors. *J. Appl. Phys.* **84**, 5005–5011 (1998).
7. Juan, T. P.-C., Chen, S. & Lee, J. Y. Temperature dependence of the current conduction mechanisms in ferroelectric $\text{Pb}(\text{Zr}_{0.53}\text{Ti}_{0.47})\text{O}_3$ thin films. *J. Appl. Phys.* **95**, 3120–3125 (2004).
8. Polcawich, R. G., C. Feng, P. Vanatta, R. Piekarcz, S. Trolier-McKinstry, M. Dubey, and M. Ervin, Highly accelerated lifetime testing (HALT) of lead zirconate titanate (PZT) thin films. *Proceedings of the 2000 12th IEEE International Symposium on Applications of Ferroelectrics, 2000. ISAF 2000* **1**, 357–360 vol. 1 (IEEE, 2000).
9. Polcawich, R. G., Moses, P. J. & Trolier-McKinstry, S. AC and DC electrical stress reliability of piezoelectric lead zirconate titanate (PZT) thin films. Presented at Microelectronics 1999. **3906**, 227 (1999).
10. Nagaraj, B., Aggarwal, S., Song, T. K., Sawhney, T. & Ramesh, R. Leakage current mechanisms in lead-based thin-film ferroelectric capacitors. *Phys. Rev. B* **59**, 16022–16027 (1999).

11. Chen, J., Chen, H. & Lee, J. Y. An investigation on the leakage current and time dependent dielectric breakdown of ferroelectric lead–zirconate–titanate thin film capacitors for memory device applications. *Appl. Phys. Lett.* **69**, 4011–4013 (1996).
12. Sudhama, C., A. Campbell, P. D. Maniar, R. E. Jones, R. Moazzami, C. J. Mogab, and J. C. Lee, A model for electrical conduction in metal-ferroelectric-metal thin film capacitors. *J. Appl. Phys.* **75**, 1014–1022 (1994).
13. Mihara, T. & Watanabe, H. Electronic Conduction Characteristics of Sol-Gel Ferroelectric $\text{Pb}(\text{Zr}_{0.4}\text{Ti}_{0.6})\text{O}_3$ Thin-Film Capacitors: Part I. *Jpn. J. Appl. Phys.* **34**, 5664 (1995).
14. Dimos, D., Schwartz, R. W. & Lockwood, S. J. Control of leakage resistance in $\text{Pb}(\text{Zr,Ti})\text{O}_3$ thin films by donor doping. *J. Am. Ceram. Soc.* **77**, 3000–3005 (1994).
15. Zhao, S., Zhang, S. J., Liu, W., Donnelly, N. J., Xu, Z., Randall, C. A., Time dependent dc resistance degradation in lead-based perovskites: $0.7 \text{Pb}(\text{Mg}_{1/3}\text{Nb}_{2/3})\text{O}_3$ – 0.3PbTiO_3 . *J. Appl. Phys.* **105**, 053705 (2009).
16. Masuda, Y. & Nozaka, T. Investigation into electrical conduction mechanisms of $\text{Pb}(\text{Zr,Ti})\text{O}_3$ thin-film capacitors with Pt, IrO_2 and SrRuO_3 top electrodes. *Jpn. J. Appl. Phys.* **43**, 6576 (2004).
17. Stolichnov, I., A. Tagantsev, N. Setter, S. Okhonin, P. Fazan, J. S. Cross, M. Tsukada, A. Bartic & D. Wouters, Constant-current study of dielectric breakdown of $\text{Pb}(\text{Zr,Ti})\text{O}_3$ ferroelectric film capacitors. *Integr. Ferroelectr.* **32**, 737–746 (2001).
18. Randall, C. A., R. Maier, W. Qu, K. Kobayashi, K. Morita, Y. Mizuno, N. Inoue and T. Oguni, Improved reliability predictions in high permittivity dielectric oxide capacitors under high dc electric fields with oxygen vacancy induced electromigration. *J. Appl. Phys.* **113**, 014101 (2013).

19. Ohring M., *The Materials Science of Thin Films*. Academic Press, London, 1992.
20. Lampert, M.. *Current Injection in Solids*. Academic Press, London, 1970.

Chapter 9

Conclusions and Future Work

9.1 Conclusions

This chapter reviews the major conclusions from the work described in this thesis. Recommendations for future work are provided in light of these results.

9.1.1 Residual Ferroelectricity in BST Tunable Dielectrics

Rayleigh behavior as a function of temperature was used to track the ferroelectric behavior of BST materials through the ferroelectric to paraelectric transition temperature. The irreversible Rayleigh parameter serve as a metric for the presence of ferroelectricity because this response is dependent on the presence of domain walls, cluster boundaries or phase boundaries. The Rayleigh results were found to be in good agreement with the measured minor polarization-electric field hysteresis loops. The logarithmic decay of the frequency dependence of the Rayleigh behavior was consistent with other ferroelectric systems¹ and the Rayleigh behavior was further corroborated through optical second harmonic generation. In the future it would be important to address the impacts of inhomogeneous electric fields in the materials with interdigitated top electrodes on the Rayleigh response and tunability in these materials.

From the Rayleigh analysis, residual ferroelectricity –a persistent ferroelectric response above the global phase transition temperature– was observed in BST ceramics and thin films processed by different methods. While all of the measured materials exhibited residual

ferroelectricity, the temperature extent varied greatly between materials processed by different methods. A-site chemical inhomogeneity was found to promote residual ferroelectricity.

This study has shown ferroelectric based loss persists well beyond the expected transition temperature in many BST materials. In order to avoid ferroelectric based loss the transition temperature should be suppressed, by varying the barium to strontium ratio, in equal measure to the temperature extent of the residual ferroelectricity. It is also suggested that ferroelectric measurements of tunable dielectric material be routinely made using Rayleigh analysis. Rayleigh analysis provides an indication of ferroelectricity which is not possible through polarization-electric field hysteresis loops which is what is currently most often reported.

9.1.2. Residual Ferroelectricity and Flexoelectricity

Residual ferroelectricity is observed in barium strontium titanate ceramics 30°C above the global phase transition temperature, in the same temperature range in which anomalously large flexoelectric coefficients are reported. The application of a strain gradient in this temperature range leads to strain gradient-induced poling, or flexoelectric poling, enhancing the flexoelectric response. Flexoelectric poling was observed by the development of a remanent polarization in flexoelectric measurements upon the removal of the applied strain gradient. Additionally, an induced d_{33} piezoelectric response was observed in samples after the removal of the applied strain gradient, indicating that the polarization was realigned during flexoelectric measurements. Flexoelectric poling lead to the production of an internal bias of 9 kV/m . It is concluded that residual ferroelectric response considerably enhances the observed flexoelectric response.

9.1.3. Electric Field Induced Piezoelectricity in BST thin films

Metrology was designed, developed and calibrated for the measurement of the $e_{31,f}$ piezoelectric coefficient as a function of applied electric field and strain. This allowed for direct measurements of the field-induced piezoelectric response for $Ba_{0.7}Sr_{0.3}TiO_3$ (70:30) and $Ba_{0.6}Sr_{0.4}TiO_3$ (60:40) thin films on MgO and silicon. The DC electric field dependence of the permittivity (tunability), and the dielectric non-linearity were also characterized. The relative dielectric tunabilities for the 70:30 and 60:40 composition on MgO were 83% and 70% respectively, with a dielectric loss of less than 0.011 and 0.004 at 100 kHz. A linear increase in induced piezoelectricity with field to -3.0 C/m^2 and -1.5 C/m^2 at 110 kV/cm was observed in 60:40 BST on MgO and 70:30 BST on Si. Large and hysteretic piezoelectric and tuning responses were observed in the 70:30 BST thin films on MgO. This was consistent with the irreversible Rayleigh behavior, indicating a ferroelectric contribution to the piezoelectric and dielectric response 40°C above the global paraelectric transition temperature. Field-induced piezoelectricity was observed both in films on substrates which should impart tensile or compressive stress. This information should enable advancements in tunable dielectric components through the removal of piezoelectric resonance-based loss mechanisms. Further work in investigating the piezoelectric and electrostrictive response could be done through an investigation of the electromechanical response at odd or even higher order harmonics.

9.2 Future Work

9.2.1. Characterization of Residual Ferroelectricity in Materials for Flexoelectric Applications

Chapter 7 discusses the relationship between residual ferroelectricity and flexoelectricity (specifically the flexocoupling factor) in BST. Flexocoupling factors which are orders of magnitude higher than what was theoretically predicted (1-10V) have been observed in BST.² Residual ferroelectricity, as measured through Rayleigh analysis, is examined as a mechanism behind the enhanced flexocoupling in BST.

Enhanced flexocoupling is not exclusive to BST, in fact many ferroelectric perovskite materials exhibit anomalously large flexocoupling coefficients. The last column of Table 9.1 shows the flexocoupling factor, f , for a series of ferroelectric perovskites.² The available data suggest that flexocoupling coefficients beyond what is theoretically predicted are observed in all perovskites which can become ferroelectric. In contrast to this, in perovskite materials with similar structures but lacking ferroelectricity, such as strontium titanate, the flexocoupling response is within the predicted range of 1-10 V.³

There have been as of yet few attempts to study the mechanisms of enhanced flexocoupling in ferroelectric perovskites. Narvaez and Catalan have shown a correlation between the onset of nano-polar regions and enhanced flexoelectric response in a relaxor ferroelectric.⁴ This supports the idea that ferroelectricity impacts the flexoelectric response, but does not account for the nominally normal ferroelectric perovskites with enhanced flexocoupling.

The work described within this thesis shows a correlation between the onset of residual ferroelectricity and enhanced flexocoupling in BST. Extending the study of residual ferroelectricity to other materials for flexoelectric applications, such as barium titanate, lead

zirconate titanate and lead magnesium niobate, would further substantiate the correlations observed in this work. Understanding the temperature extent of any ferroelectric response or mobile polar distortion, is particularly important as many of these materials are characterized and used within a few degrees of the ferroelectric phase transition, as shown for barium titanate in the first row of Table 9.1. Additionally, if any residual ferroelectric response were observed in these flexoelectric materials it would facilitate the development of new models of flexocoupling. This would in turn provide a better metrics for the design of flexoelectric devices.

Table 9.1. Flexoelectric and flexocoupling response in a series of perovskite materials. All measurements are taken on nominally paraelectric materials. The method column indicates the method of flexoelectric characterization where: CB stands for cantilever beam, 4PB is by four point beam testing, CFE is converse flexoelectric effect, and PC is pyramidal compression. From reference ²

Compound	Coefficient	Method	Value ($\mu\text{C m}^{-1}$)	χ/ϵ_0	$f = \mu/\chi$ (V)
BaTiO ₃	$\bar{\mu}_{12}$ ($T_c + 3.4$ K)	CB	~50 (62)	~10,000	~560 (62)
Ba _{0.67} Sr _{0.33} TiO ₃	$\bar{\mu}_{11}$	PC (0.5 Hz)	150 (12)	~20,000	~850
	$\bar{\mu}_{11}$	CFE (400 Hz)	120 (67)		
	$\bar{\mu}_{12}$	CB (1 Hz)	100 (60)	~16,000	~700
Ba _{0.65} Sr _{0.35} TiO ₃	$\bar{\mu}_{12}$	CB	~8.5 (144)	4,100	234
PbMg _{0.33} Nb _{0.67} O ₃	$\bar{\mu}_{12}$	CB	3–4 (58)	~13,000	~26–45
PMN-PT	$\bar{\mu}_{11}$	PC (4–10 Hz)	6–12 (69)	21,000	~32–65
		PC (0 Hz)	20–50 (69)		~110–270
Pb _{0.3} Sr _{0.7} TiO ₃	$\bar{\mu}_{11}$	PC (0.5 Hz)	20 (12)	13,500	170
Pb(Zr,Ti)O ₃	$\bar{\mu}_{12}$	4PB	0.5 (63)	~2,200	25
		CB (1 Hz)	1.4 (61)		72

9.2.2. Characterization of A-Site Chemical Inhomogeneity in BST

In chapter 6, residual ferroelectricity in BST was investigated with respect to A-site chemical inhomogeneity. As measured by electron energy loss spectroscopy, EELS, there is a significant difference between samples with narrow and broad temperature dependent Rayleigh behavior, with inhomogeneous samples exhibiting broader temperature dependences. Now that this chemical inhomogeneity has been observed, the next step to mitigating residual ferroelectric based loss requires an understanding of the driving forces for disordering in the BST system. Understanding the mechanisms which control the length scales of ordering in this material could provide insight into methods to regulate chemical homogeneity and reduce ferroelectric loss. Further information could be inferred through an investigation of variations in the full width half maximum of the x-ray diffraction patterns taken on the samples used in this study. Additionally, further investigations into the time and temperature dependence of the Rayleigh response would provide information about aging and degradation from which inference could be made into the structure and movement of the domains, cluster or phase boundaries. A direct measurement of the order could also be possible through the application of transmission electron microscopy, as has previously been used in the work of Bursill to identify ordered clusters in barium titanate.⁵

Further establishing a causal relationship between A-site chemical inhomogeneity and residual ferroelectricity requires a thorough measure of the local chemical distribution. The EELS method relies on variations in the barium to titanium ratio to infer differences between the barium to strontium ratios. This assumes that barium titanate is a line compound. However, it is known that a finite solid solution window exists with variable A:B ratios.⁶ Furthermore, thin films are not necessarily in thermodynamic equilibrium,^{7,8} which could further change the A:B ratio in the single phase material. Energy dispersive spectroscopy, EDS, would allow for a more direct characterization of the local scale barium to strontium ratio.⁹ EDS measurements on barium

titanate based materials are complicated by an overlap of the energies of barium and titanium, as shown in Figure 9.1.¹⁰ However recent advances in analysis software now provide corrective peak fitting measures specifically for barium titanate.¹⁰

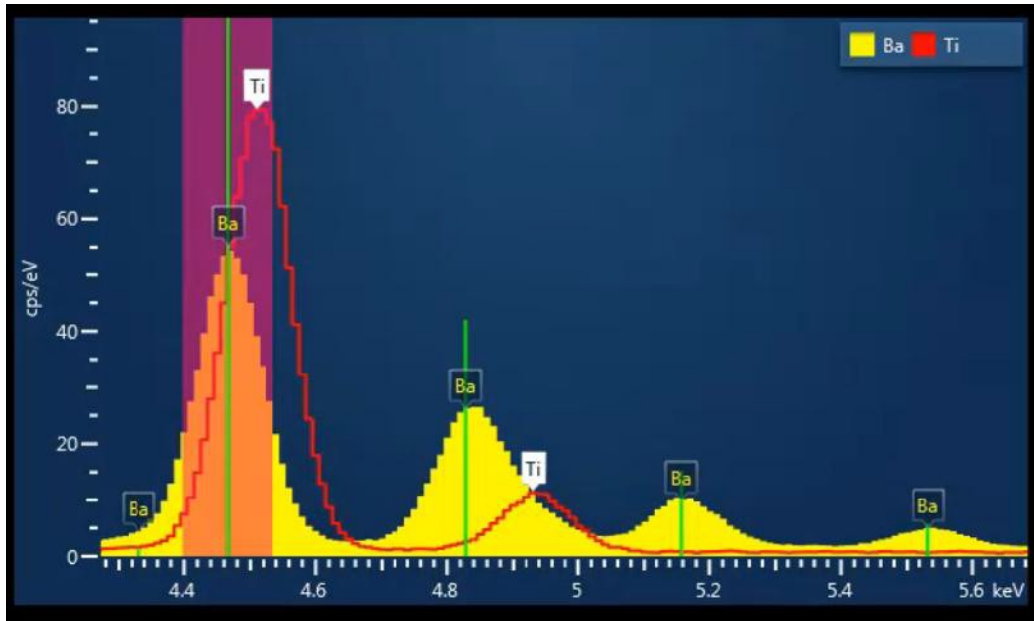


Figure 9.1. Characteristic EDS response from barium titanate. From reference⁹

An x-ray photoelectron spectroscopy of secondary ion mass depth profile depth profile could, in principle allow extraction of quantitative compositional data, although typically the lateral resolution is not adequate.¹¹ Quantifying the relationship between chemical composition and residual ferroelectricity is a necessary next step towards developing routes to mitigate loss in tunable dielectrics.

9.3 References

1. Taylor, D. V. & Damjanovic, D. Evidence of domain wall contribution to the dielectric permittivity in PZT thin films at sub-switching fields. *J. Appl. Phys.* **82**, 1973–1975 (1997).
2. Zubko, P., Catalan, G. & Tagantsev, A. K. Flexoelectric effect in solids. *Annu. Rev. Mater. Res.* **43**, 387–421 (2013).
3. Zubko, P., Catalan, G., Buckley, A., Welche, P. R. L. & Scott, J. F. Strain-Gradient-Induced polarization in SrTiO₃ single crystals. *Phys. Rev. Lett.* **99**, 167601 (2007).
4. Narvaez, J. & Catalan, G. Origin of the enhanced flexoelectricity of relaxor ferroelectrics. *Appl. Phys. Lett.* **104**, 162903 (2014).
5. Bursill, L. A. & Lin, P. J. Microdomains observed at the ferroelectric/paraelectric phase transition of barium titanate. *Nature* **311**, 550–552 (1984).
6. Lee, S., Randall, C. A. & Liu, Z.-K. Modified phase diagram for the barium oxide–titanium dioxide system for the ferroelectric barium titanate. *J. Am. Ceram. Soc.* **90**, 2589–2594 (2007).
7. Schwartz, R. W. Chemical solution deposition of perovskite thin films. *Chem. Mater.* **9**, 2325–2340 (1997).
8. Lange, F. F. Chemical solution routes to single-crystal thin films. *Science* **273**, 903–909 (1996).
9. Joshi, U. A. & Lee, J. S. Template-Free hydrothermal synthesis of single-crystalline barium titanate and strontium titanate nanowires. *Small* **1**, 1172–1176 (2005).
10. AZtec TruMap. EDS Software. (Oxford Instruments, 2013).
11. Stickle, William F., Peter E. Sobol, and Kenneth D. Bomben. *Handbook of X-ray photoelectron spectroscopy*. Vol. 40. Eden Prairie, MN: Perkin Elmer, 1992.

VITA

Lauren Garten

Lauren Garten was born in Utica, MI on June 23, 1986. In 2004 she began studying music performance/education at the Missouri State University. For two years she played in a number of music ensembles and toured the country with a drum and bugle corps. Then after a long battle with severe stage fright, she decided to give up her career in music and follow her passion for science (and hoped to never have to perform in front of a crowd again). She transferred to the University of Missouri-Rolla, and graduated with a bachelors degree in ceramic engineering in December 2008. Then in January 2009 she started her graduate career at the Pennsylvania State University. In 2011 she transferred out of the program to work as a technician for Dr. Meyer at the Applied Research Laboratory and for Dr. Trolier-McKinstry at the Materials Research Laboratory. She then restarted her graduate career with Dr. Trolier-McKinstry and under her guidance went on to complete her graduate work.